

NAVAL POSTGRADUATE SCHOOL

Monterey, California



THESIS

**RECURSIVE BLOCK-BY-BLOCK INTEGRAL
EQUATION SOLUTION FOR TRANSIENT
DYNAMIC ANALYSIS WITH MEMORY-TYPE
ELEMENTS**

by

Al V. Jarque

March 2001

Thesis Advisor:

Joshua Gordis

Approved for public release; distribution is unlimited.

20010612 016

REPORT DOCUMENTATION PAGE			Form Approved OMB No. 0704-0188	
Public reporting burden for this collection of information is estimated to average 1 hour per response, including the time for reviewing instruction, searching existing data sources, gathering and maintaining the data needed, and completing and reviewing the collection of information. Send comments regarding this burden estimate or any other aspect of this collection of information, including suggestions for reducing this burden, to Washington Headquarters Services, Directorate for Information Operations and Reports, 1215 Jefferson Davis Highway, Suite 1204, Arlington, VA 22202-4302, and to the Office of Management and Budget, Paperwork Reduction Project (0704-0188) Washington DC 20503.				
1. AGENCY USE ONLY (Leave blank)		2. REPORT DATE March 2001		3. REPORT TYPE AND DATES COVERED Master's Thesis
4. TITLE AND SUBTITLE Recursive Block-by-Block Integral Equation Solution For Transient Dynamic Analysis With Memory-Type Elements			5. FUNDING NUMBERS	
6. AUTHOR(S) Jarque, Al V.				
7. PERFORMING ORGANIZATION NAME(S) AND ADDRESS(ES) Naval Postgraduate School Monterey CA 93943-5000			8. PERFORMING ORGANIZATION REPORT NUMBER	
9. SPONSORING/MONITORING AGENCY NAME(S) AND ADDRESS(ES)			10. SPONSORING/MONITORING AGENCY REPORT NUMBER	
11. SUPPLEMENTARY NOTES The views expressed in this thesis are those of the author and do not reflect the official policy or position of the Department of Defense or the U.S. Government.				
12a. DISTRIBUTION/AVAILABILITY STATEMENT Approved for public release; distribution is unlimited			12b. DISTRIBUTION CODE	
13. ABSTRACT (maximum 200 words) An efficient method of computing structural response of multi-story nonlinear base isolated buildings for a given seismic event is presented. Using a recursive block-by-block convolution (RBBIEF) solution to the governing nonlinear Volterra integral equation, structural base motion acting through an arbitrary number of nonlinear base isolators can be computed quickly and accurately. The general solution to the governing nonlinear Volterra integral is formulated and subsequently converted into code using MATLAB. The procedure incorporates modal properties, computed from conventional finite element (FE) techniques, and the generated MATLAB programs to solve a varying set of multi-degree of freedom structures coupled to both linear and nonlinear isolators. Ultimately, an analysis is conducted on a 30-story building that was overly designed using the 1994 Load Resistance Factor Design [Ref. 1] and the 1994 Uniform Building Codes [Ref. 2] for earthquake loading. The method demonstrates that the Volterra integration scheme in the time domain is very effective and efficient.				
14. SUBJECT TERMS: Finite Element, Nonlinear Dynamic Transient Response, Seismic Response, Volterra integral, Nonlinear Structural Base Isolation, Hysteretic isolators			15. NUMBER OF PAGES 112	
			16. PRICE CODE	
17. SECURITY CLASSIFICATION OF REPORT Unclassified	18. SECURITY CLASSIFICATION OF THIS PAGE Unclassified	19. SECURITY CLASSIFICATION OF ABSTRACT Unclassified	20. LIMITATION OF ABSTRACT UL	

THIS PAGE INTENTIONALLY LEFT BLANK

Approved for public release; distribution is unlimited

**RECURSIVE BLOCK-BY-BLOCK INTEGRAL EQUATION SOLUTION
FOR TRANSIENT DYNAMIC ANALYSIS WITH MEMORY-TYPE
ELEMENTS**

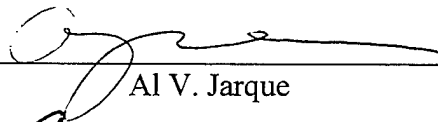
Al V. Jarque
Lieutenant, United States Navy
B.S., University of California at San Diego, 1994

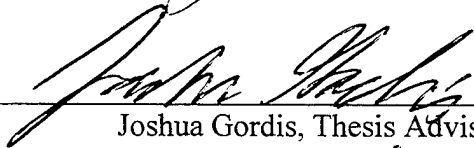
Submitted in partial fulfillment of the
requirements for the degree of

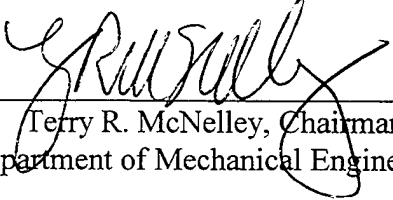
MASTER OF SCIENCE IN MECHANICAL ENGINEERING

from the

**NAVAL POSTGRADUATE SCHOOL
March 2001**

Author: 
Al V. Jarque

Approved by: 
Joshua Gordis, Thesis Advisor


Terry R. McNelley, Chairman
Department of Mechanical Engineering

THIS PAGE INTENTIONALLY LEFT BLANK

ABSTRACT

An efficient method of computing structural response of multi-story nonlinear base isolated buildings for a given seismic event is presented. Using a recursive block-by-block integral equation formulation (RBBIEF) solution to the governing nonlinear Volterra integral equation, structural base motion acting through an arbitrary number of nonlinear base isolators can be computed quickly and accurately. The general solution to the governing nonlinear Volterra integral is formulated and subsequently converted into code using MATLAB. The procedure incorporates modal properties, computed from conventional finite element (FE) techniques, and the generated MATLAB programs to solve a varying set of multi-degree of freedom structures coupled to both linear and nonlinear isolators. Ultimately, an analysis is conducted on a 30-story building that was overly designed using the 1994 Load Resistance Factor Design [Ref. 1] and the 1994 Uniform Building Codes [Ref. 2] for earthquake loading. The method demonstrates that the Volterra integration scheme in the time domain is very effective and efficient.

THIS PAGE INTENTIONALLY LEFT BLANK

TABLE OF CONTENTS

I.	INTRODUCTION	1
II.	EARTHQUAKE DESIGN AND NONLINEAR ISOLATORS	5
A.	STRUCTURAL DESIGN.....	5
B.	EARTHQUAKE SAMPLING.....	7
C.	NONLINEAR BASE ISOLATION	10
1.	Rubber Isolators	12
2.	Elastomeric Isolators.....	13
3.	Hysteretic Isolators	14
D.	MATHEMATICAL MODELS.....	14
1.	Bilinear Element	14
2.	Wen Element	18
3.	Maxwell Element.....	22
E.	LOAD DEPENDANT ISOLATORS	22
III.	EQUATIONS OF MOTION AND NONLINEAR ISOLATORS.....	25
A.	GOVERNING EQUATIONS	25
B.	VOLTERRA INTEGRAL FORMULATION	28
C.	RECURSIVE ITERATION FORMULATION	32
D.	LINEAR AND NONLINEAR RECURSIVE BLOCK-BY-BLOCK FORMULATION	34
E.	UPLIFT IN RECURSIVE BLOCK-BY-BLOCK SYNTHESIS	39
F.	SINGLE ISOLATION TRAPEZOIDAL EXTRACTION	40
V.	RESULTS	43
A.	PROGRAM VALIDATION	44
1.	De-coupled Versus Coupled System	44
2.	Block-by-Block Synthesis Versus MATLAB's <i>ODE45</i>	47
3.	Model Isolator Plots.....	50
B.	SINGLE BAY 4-STORY BUILDING	53
C.	9-BAY 4-STORY BUILDING	62
D.	30 STORY BUILDING	71

VI. CONCLUSIONS	81
VII. RECOMMENDATIONS FOR FUTURE WORK	83
APPENDIX. TRAPEZOIDAL FORCE EXTRACTION VERSUS NASTRAN AND ODE45	85
LIST OF REFERENCES	89
INITIAL DISTRIBUTION LIST	91

LIST OF FIGURES

Figure 1. UBC Seismic Acceleration Graph From Ref. [3].....	5
Figure 2. Imperial Valley Accelerometer Plot From Ref. [8].....	8
Figure 3. El Centro 1940 North South Power Spectral Density Function of the Displacement Time History Data	10
Figure 4. Hysteretic Loop of an Elastic-Pure Plastic Isolator	11
Figure 5. Bilinear Hysteretic Loop	13
Figure 6. Bilinear Algorithm	17
Figure 7. Parameters of the Wen's Model From Ref. [14:p. 355].....	18
Figure 8. Wen Element Hysteresis Loop for $F_y=1$, $A=2$, $\eta=2$, $\beta=1$, $\gamma=1$, $\delta_y=1$, $\alpha=.01$ due to Unit Sinusoidal Excitation at .5 Hz.....	20
Figure 9. Parameter Change Effects on Wen Hysteresis, a) Increase F_y b) Increase A , c) Increase β , d) Increase η , e) Increase δ_y , f) Increase α , g) Increase γ	21
Figure 10. Isolator's Properties Versus Vertical Displacements	23
Figure 11. Shear Stresses on a Load Isolator From [Ref. 9:p.142].....	24
Figure 12. N-Story Base isolated Structure	26
Figure 13. Basic Recursive Iteration Algorithm	34
Figure 14. Recursive Block-by-Block Algorithm.....	37
Figure 15. Recursive Interpolation	39
Figure 16. 9-DOF Spring Mass System.....	45
Figure 17. Uncoupled Large Mass 9-DOF Spring Mass System.....	45

Figure 18. Base Displacement Time History of 9-DOF System Using Recursive Block-by-Block Synthesis	46
Figure 19. 9-DOF Spring Mass System, Absolute Base Displacement Differences Between a Three Block Recursive Block-by-Block Synthesis and ODE45	48
Figure 20. Three Block Synthesis Versus <i>ODE45</i> Base Displacements Comparisons of a Linear Spring Isolated 9-DOF Spring Mass System, from a Unit Sinusoidal Ground Excitation at .5 Hz	49
Figure 21. Three Block Synthesis Versus <i>ODE45</i> Hysteresis Comparisons of a Linear Spring Isolated 9-DOF Spring Mass System, from a Unit Sinusoidal Ground Excitation at .5 Hz	49
Figure 22. Unit Sinusoidal Ground Excitation at .5 Hz on a Real Bilinear Isolator.....	51
Figure 23. Unit Sinusoidal Ground Excitation at .5 Hz on an ideal Bilinear Isolator	51
Figure 24. Unit Sinusoidal Ground Excitation at .5 Hz on a Wen Isolator	52
Figure 25. Unit Sinusoidal Ground Excitation at .5 Hz on a Maxwell Isolator.....	52
Figure 26. 1940 El Centro North South Ground Motion Time History	53
Figure 27. Single Bay, 4-Story Building Frame	54
Figure 28. Single Bay, 4-Story, Real Bilinear Isolator, Corner Node Hysteresis	55
Figure 29. Single Bay, 4-Story, Real Bilinear Isolator, Corner Node Lateral Displacement History	55
Figure 30. Single Bay, 4-Story, Real Bilinear Isolator, Corner Node Uplift Displacement History	56
Figure 31. Single Bay, 4-Story, ideal Bilinear Isolator, Corner Node Hysteresis for the	

1940 El Centro North South Earthquake Ground Motion	56
Figure 32. Single Bay, 4-Story, ideal Bilinear Isolator, Corner Node Lateral Displacement History for the 1940 El Centro North South Earthquake Ground Motion	57
Figure 33. Single Bay, 4-Story, ideal Bilinear Isolator, Corner Node Uplift Displacement History for the 1940 El Centro North South Earthquake Ground Motion	57
Figure 34. Single Bay, 4-Story, Wen Isolator, Corner Node Hysteresis for the 1940 El Centro North South Earthquake Ground Motion.....	58
Figure 35. Single Bay, 4-Story, Wen Isolator, Corner Node Lateral Displacement History for the 1940 El Centro North South Earthquake Ground Motion.....	58
Figure 36. Single Bay, 4-Story, Wen Isolator, Corner Node Uplift Displacement History for the 1940 El Centro North South Earthquake Ground Motion.....	59
Figure 37. Single Bay, 4-Story, Maxwell Isolator, Corner Node Hysteresis for the 1940 El Centro North South Earthquake Ground Motion	59
Figure 38. Single Bay, 4-Story, Maxwell Isolator, Corner Node Lateral Displacement History for the 1940 El Centro North South Earthquake Ground Motion.....	60
Figure 39. Single Bay, 4-Story, Maxwell Isolator, Corner Node Uplift Displacement History for the 1940 El Centro North South Earthquake Ground Motion.....	60
Figure 40. 9-Bay, 4-Story Building Frame	62
Figure 41. 9-Bay, 4-Story, Real Bilinear Isolator, Corner Node Hysteresis for the 1940 El Centro North South Earthquake Ground Motion	64

Figure 42. 9-Bay, 4-Story, Real Bilinear Isolator, Corner Node Lateral Displacement History for the 1940 El Centro North South Earthquake Ground Motion.....	64
Figure 43. 9-Bay, 4-Story, Real Bilinear Isolator, Corner Node Uplift Displacement History for the 1940 El Centro North South Earthquake Ground Motion.....	65
Figure 44. 9-Bay, 4-Story, ideal Bilinear Isolator, Corner Node Hysteresis for the 1940 El Centro North South Earthquake Ground Motion	65
Figure 45. 9-Bay, 4-Story, ideal Bilinear Isolator, Corner Node Lateral Displacement History for the 1940 El Centro North South Earthquake Ground Motion.....	66
Figure 46. 9-Bay, 4-Story, ideal Bilinear Isolator, Corner Node Uplift Displacement History for the 1940 El Centro North South Earthquake Ground Motion.....	66
Figure 47. 9-Bay, 4-Story, Wen Isolator, Corner Node Hysteresis for the 1940 El Centro North South Earthquake Ground Motion	67
Figure 48. 9-Bay, 4-Story, Wen Isolator, Corner Node Lateral Displacement History for the 1940 El Centro North South Earthquake Ground Motion	67
Figure 49. 9-Bay, 4-Story, Wen Isolator, Corner Node Uplift Displacement History for the 1940 El Centro North South Earthquake Ground Motion	68
Figure 50. 9-Bay, 4-Story, Maxwell Isolator, Corner Node Hysteresis for the 1940 El Centro North South Earthquake Ground Motion.....	68
Figure 51. 9-Bay, 4-Story, Maxwell Isolator, Corner Node Lateral Displacement History for the 1940 El Centro North South Earthquake Ground Motion.....	69
Figure 52. 9-Bay, 4-Story, Maxwell Isolator, Corner Node Uplift Displacement History for the 1940 El Centro North South Earthquake Ground Motion.....	69

Figure 53. 30-Story Building, Wire Frame	72
Figure 54. 30-Story, Real Bilinear Isolator, Corner Node Hysteresis for the 1940 El Centro North South Earthquake Ground Motion.....	73
Figure 55. 30-Story, Real Bilinear Isolator, Corner Node Lateral Displacement History for the 1940 El Centro North South Earthquake Ground Motion.....	73
Figure 56. 30-Story, Real Bilinear Isolator, Corner Node Uplift Displacement History for the 1940 El Centro North South Earthquake Ground Motion.....	74
Figure 57. 30-Story, ideal Bilinear Isolator, Corner Node Hysteresis for the 1940 El Centro North South Earthquake Ground Motion.....	74
Figure 58. 30-Story, ideal Bilinear Isolator, Corner Node Lateral Displacement History for the 1940 El Centro North South Earthquake Ground Motion.....	75
Figure 59. 30-Story, ideal Bilinear Isolator, Corner Node Uplift Displacement History for the 1940 El Centro North South Earthquake Ground Motion.....	75
Figure 60. 30-Story, Wen Isolator, Corner Node Hysteresis for the 1940 El Centro North South Earthquake Ground Motion.....	76
Figure 61. 30-Story, Wen Isolator, Corner Node Lateral Displacement History for the 1940 El Centro North South Earthquake Ground Motion	76
Figure 62. 30-Story, Wen Isolator, Corner Node Uplift Displacement History for the 1940 El Centro North South Earthquake Ground Motion	77
Figure 63. 30-Story, Maxwell Isolator, Corner Node Hysteresis for the 1940 El Centro North South Earthquake Ground Motion	77
Figure 64. 30-Story, Maxwell Isolator, Corner Node Lateral Displacement History for	

the 1940 El Centro North South Earthquake Ground Motion	78
Figure 65. 30-Story, Maxwell Isolator, Corner Node Uplift Displacement History for the 1940 El Centro North South Earthquake Ground Motion	78
Figure 66. NASTRAN Sinusoidal Base Excitation Tip Displacement Results of a 375 Feet Steel W36x487 Column.....	86
Figure 67. 375 Feet Steel W36x487 Column , NASTRAN Versus Trapezoidal Time History Difference Plot of Tip DOF	86
Figure 68. Trapezoidal Extraction Base Node Displacement Time History of a 9-DOF System.....	88
Figure 69. 9-DOF Spring Mass System, ODE Versus Trapezoidal Extraction Absolute Difference Plot of Base DOF	88

LIST OF TABLES

Table 1. Parameters of Modeled Buildings	44
Table 2. Model Isolator Parameters of Sinusoidal Input	50
Table 3. Single Bay, 4-Story Isolator Properties.....	54
Table 4. Single Bay, 4-Story, 1940 El Centro Earthquake Recursive Block-by-Block Synthesis Time Results in Seconds	61
Table 5. Single Bay, 4-Story, 1940 El Centro Earthquake Recursive Block-by-Block Synthesis FLOP Count Results.....	61
Table 6. 9-Bay, 4-Story Isolator Properties	63
Table 7. 9-Bay, 4-Story, 1940 El Centro Earthquake Recursive Block-by-Block Synthesis Time Results in Seconds	70
Table 8. 9-Bay, 4-Story, 1940 El Centro Earthquake Recursive Block-by-Block Synthesis FLOP Count Results.....	70
Table 9. 30-Story Isolator Properties	71
Table 10. 30-Story, 1940 El Centro Earthquake Recursive Block-by-Block Synthesis Time Results in Seconds.....	79
Table 11. 30-Story, 1940 El Centro Earthquake Recursive Block-by-Block Synthesis FLOP Count Results	79
Table 12. Optimum Times for Nonlinear Wen Element Synthesis	80

THIS PAGE INTENTIONALLY LEFT BLANK

I. INTRODUCTION

Seismic base motion is an important design factor in constructing and retrofitting structures. The extensive base displacements and resultant shear forces caused by large magnitude earthquakes are major contributors to the eventual failure of the structure. Isolating structures from seismic events is currently accomplished through the use of passive isolators.

Originally, it was the engineer's goal to reduce the structural displacements through isolation. However, current techniques place equal importance on increasing the energy dissipation in an isolation device. An increase in the area contained within the device's hysteresis loop is directly related to the energy dissipation provided by the device. The plastic properties of passive hysteretic type isolators are mathematically modeled as a complex nonlinear equation [Ref. 3]. Modeling and analysis using finite element (FE) techniques for nonlinear isolators then becomes equally complex and computationally demanding.

Several Commercial-Off-the-Shelf (COTS) programs such as, IDRAC-3D, 3D-BASIS, DRAIN-2DX, SAP, ANSR, N-PAD, LPM, and others have their respective limitations and advantages as outlined in [Ref. 3]. The primary solution methods for nonlinear base isolation of structures are the pseudo-force iterative method or the nonlinear tangent stiffness method [Ref. 3]. However, the incorporation of 3-D motion and discrete time histories in conjunction with n-nonlinear isolators to the above-mentioned FE programs can be computationally exhaustive and or not practically possible.

Current FE programs can, in seconds, compute normalized mode shapes and natural frequencies of several thousand degree of freedom systems. The structure's modal properties are used by many of the above programs in order to compute transient response or frequency response. Unlike the methods of solving the differential equations of motion above, we describe herein a method that solves the transient response directly using the Volterra integral form. This method, referred to as time domain synthesis, is presented in [Ref. 4] and [Ref. 5], and is a numerically accurate and fast solution for structural response due to base motion excitation through nonlinear isolation.

The addition of nonlinear memory-type isolators to the time domain synthesis is presented herein. Currently, the synthesis is solved using the (RBBIEF) method. The RBBIEF method obtains its significant efficiency from two characteristics of the formulation. First, a structure is described by impulse response functions calculated only for those physical DOF of interest. Those DOF for which response is not required can be omitted with no loss of accuracy. Second, the block-by-block convolution divides a large time history into several "blocks," and the governing Volterra integral equation is solved in a block-by-block manner wherein only one block undergoes iterative convolution at a time. The converged forces of synthesis from previously iterated blocks are used in conjunction with the results of the current iteration to calculate the response for the current block. To incorporate memory-type isolators in the synthesis, the isolator equations are solved using standard numerical solution techniques for ordinary differential equations. This solution of the isolator's governing differential equation is incorporated into the RBBIEF method. This revised synthesis method provides fast and

accurate solutions. Ultimately, the combination of quick eigenvalue solutions of large degree of freedom structures, modal reduction, and a block-by-block recursive solution of the governing integral equation of the retained nodes that are seismically excited, can lead to significant timesavings and accuracy.

THIS PAGE INTENTIONALLY LEFT BLANK

II. EARTHQUAKE DESIGN AND NONLINEAR ISOLATORS

A. STRUCTURAL DESIGN

Current design techniques and survivability rely upon the structure's total strain energy capacity as it plastically deforms during a seismic event. This "hard working" process is accounted for by the Uniform Building Code, UBC. In Figure 1 below, the UBC's required seismic coefficient is significantly underestimating the various earthquakes presented.

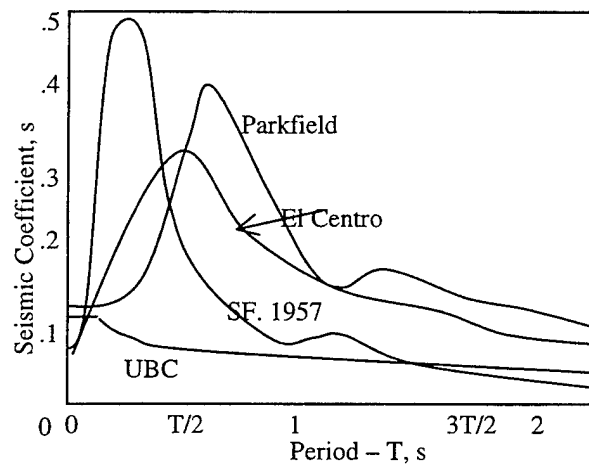


Figure 1. UBC Seismic Acceleration Graph From Ref. [3]

Additional varying normalized response spectra plots similar to Figure 1 are produced in [Ref. 3]. The vertical axis outlines the seismic coefficient and is used in various UBC equations, the horizontal axis represents structural periods. The apparent differences between the UBC's required protection as seen in Figure 1 and an arbitrary seismic excitation is where passive base isolation plays its important role. In order to ensure the reduction of the earthquake's overall input forces using passive isolators, an assumed normalized response spectrum is chosen.

Existing codes outlined in Chapter 23 of [Ref. 3] require that the existing structure have several design capacities such as seismic base shear, lateral seismic force, lateral deflection, overturning moment, and torsional moment. As part of the seismic design procedure, the structure is converted into modal space and a conservative participation factor is chosen. The general design equation is presented as:

$$\Psi_x = \sqrt{\sum_{m=1}^N \Psi_{xm}^2} \quad (1)$$

Replacing ψ with V for shear, Δ for drift, δ for deflection, M for moment, and T for torsion into Equation (1) above to arrive at the respective design limits. The subscript (m) represents the modal values and (x) the story level. Details of modal decomposition and participation can be found in numerous vibration textbooks such as [Ref. 6] and will be summarized in subsequent chapters herein.

A 30 story moment resisting frame (MRF) building was conservatively designed using the Manual of Steel Construction, Load Resistance Factor Design (LRFD) [Ref.1], the Uniform Building Code (UBC). [Ref.2], and a steel structure design textbook [Ref. 7]. The structure has an inter-story height of 17 feet and a total building height of 510 ft. The columns were spaced 25-ft center to center leading to an overall length of 400 ft at the base. A total of 256 columns are present corresponding to 256 base isolators at the base. Each floor was designed to support a dead load of 150 psf and the roof, 50 psf. The beams were divided as follows: the roof consisted of W36x135 beams; Floors 30-21 W36x150; Floors 20-11 W36x160; Floors 10-2 W36x170. The first floor was designed

as the foundation however, when the structure was redesigned for isolation, W36x170 beams were used to connect the columns at the base of the structure.

Because the isolated and non-isolated structures are two distinct eigenvalue problems, due to the free-free nature of the isolated structure, vertical motion, not previously seen in a clamped structure, is no longer constrained. The addition of vertical displacements at the base is known as uplift. This uplift motion can increase local stresses as well as decrease the designed overturning moment. The effects of uplift can be seen at some or all frequencies and can have an adverse effect on many types of passive isolators.

B. EARTHQUAKE SAMPLING

Seismic events occur worldwide and on a frequent basis. Generally, earthquakes who's magnitudes are greater than five can cause significant damage. The following uncorrected ground acceleration plotted in Figure 2 is indicative of earthquake magnitudes of 6 and above. Various time history data can be obtained through several resources such as [Ref. 8].

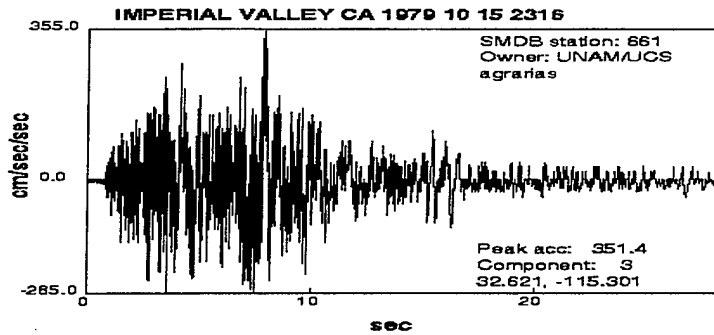


Figure 2. Imperial Valley Accelerometer Graph From Ref. [8]

Without formally verifying the enormous earthquake time history data for ergodicity, many of the earthquakes observed lasted for less than 30 seconds with the majority of the energy focused within the first 10-20 seconds. Time sampling from various monitoring stations is generally on the order of 10^{-2} seconds. Therefore time data histories can total to about 6000 data points. To reduce the amount of data and speed up the subsequent numerical solutions, correlations can be calculated similar to data signal processing.

The equations presented in this section are outlined in Reference [9] and are presented here in summary. This direct characterization is best seen in the spectral density function plot. Beginning with the auto-correlation function, Equation (2), of the acceleration time history a set of characteristics can be determined from the earthquake time history.

$$R_{xx}(\tau) = \lim_{T \rightarrow \infty} \frac{1}{T} \int_0^T x(t)x(t+\tau)dt \quad (2)$$

$$R_{xx}(0) = \text{mean square value} \quad (3)$$

$$R_{xx}(\infty) = \text{mean value squared} \quad (4)$$

Although Equations (3) and (4) are useful, Equation (2) is necessary in the computation of the power spectral density function. Taking the Fourier transform of Equation (2) a one-sided spectral density function is developed, Equation (5). This function is better known as the power spectral density function (PDF).

$$G_{xx}(f) = 2 \int_0^{\infty} R_{xx}(\tau) e^{-2\pi f \tau} d\tau \quad (5)$$

Plotting Equation (5) versus frequency will yield a graphical representation of the energy distribution of the system. There are many algorithms that take advantage of time averaging of the sample data to primarily suppress bias errors in the estimate. From the PDF an appropriate sampling frequency can be determined.

To avoid statistical sampling errors the minimum sampling frequency should be equivalent to the Nyquist frequency.

$$f_{nyq} = 2 * f_{resolution} \quad (6)$$

To increase the resolution and to avoid aliasing the general rule of thumb for the sampling frequency is:

$$f_s = 10 * f_{nyq} \quad (7)$$

Given the value of Equation (7) and the data obtained from plotting Equation (5) versus frequency, the previously mentioned 6000 data points can be dramatically reduced. Using MATLAB's power spectral density function on the El Centro earthquake, of 1940 time history data reveals it's distribution plot in Figure 3. From Figure 3 it is apparent that the majority of the energy is well below 1 Hz. Therefore, using a sampling

frequency of 10 Hz, the time step equivalent of .1 seconds, reduces the proposed 6000 data points by a factor of 10 to 600.

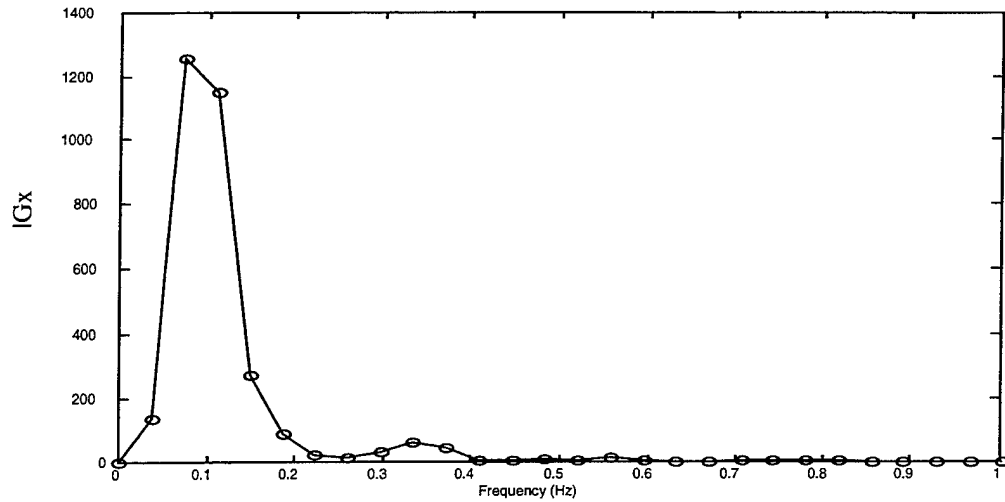


Figure 3. El Centro 1940 North South Power Spectral Density Function of the Displacement Time History Data

C. NONLINEAR BASE ISOLATION

Since many spectral density plots of seismic events indicate a dispersed frequency range, viscous dampers aren't as efficient in energy dissipation than isolators that are frequency independent. Frequency independent isolators maintain their unique hysteretic loop across a wide range of frequencies. The general topic of base isolation is well researched and discussed in [Ref. 10] and is broadly presented in this sub-section.

The general nonlinear equation that describes general frequency independent isolators is:

$$F = -K_o(1 + i\delta)(x - u_g) \quad (8)$$

Where K_o is the dynamic stiffness, δ is described as the loss factor, x the base motion, and u_g is the ground base motion. Graphically, Equation (8) spans the hysteretic loop as shown in Figure 4.

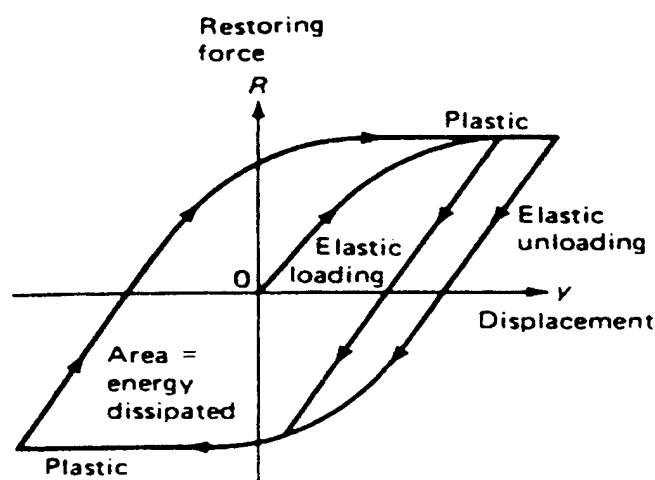


Figure 4. Hysteretic Loop of an Elastic-Pure Plastic Isolator

The process by which the hysteretic loop is formed is through cyclical deformation along a material's stress strain curve. Deformation below the tensile and compressive yield stresses describes typical linear elastic springs. Deformation beyond the initial yield stresses results in plastic deformation. In this region the material resists additional stress, due to strain hardening, leading to a secondary stiffness rate. In order to generate the hysteresis loop the subsequent unloading from the plastic region occurs elastically until it plastically deforms again.

The basic groups of base isolation in use today are linear base isolators and nonlinear energy dissipation isolators. Generally, the isolators are not designed to plastically deform but to achieve the similar hysteresis loop through hybrid systems.

Typical linear base isolators are elastic springs such as rubber or high damping rubber (HDR). Typical nonlinear isolators are hysteretic, visco-elastic, friction, or material devices. The preferred isolators in use today are the hysteretic nonlinear devices and the friction devices.

1. Rubber Isolators

Rubber used by it self is categorized as a linear base isolator. Its main advantage as an isolator is it's dynamic shear modulus, G , remains relatively constant over a wide range of frequencies and temperatures [Ref. 11]. Additionally, it's dynamic damping coefficient, δ , in Equation (8), is relatively constant at frequencies lower than 50 Hz [Ref. 11]. Given that the majority of the seismic energy was concentrated well below 50 Hz, the use of rubber isolators is desirable.

A nonlinear isolator is produced when different types of rubbers are used. The resulting combined stress strain curve for the composite rubber isolator is tri-linear [Ref.11:p. 199]. At moderate shear strains, such as wind loading and service loading, the effective spring stiffness is very low. At larger shear strains, seismic loads, the stiffness can increase dramatically until it decreases to the third stiffness rate. However, since the deformation is contained within the elastic regions of the isolator there is no hysteretic loop generated.

Additional materials or devices built into a rubber isolator can produce a hysteretic effect. The plastic deformation rate would dominate the isolator's property at larger deformations while the elastic stiffness of the rubber would control the subsequent

moderate cyclical loading and unloading on the isolator. The effect, during seismic loading, is generally modeled as a bilinear model as shown in Figure 5.

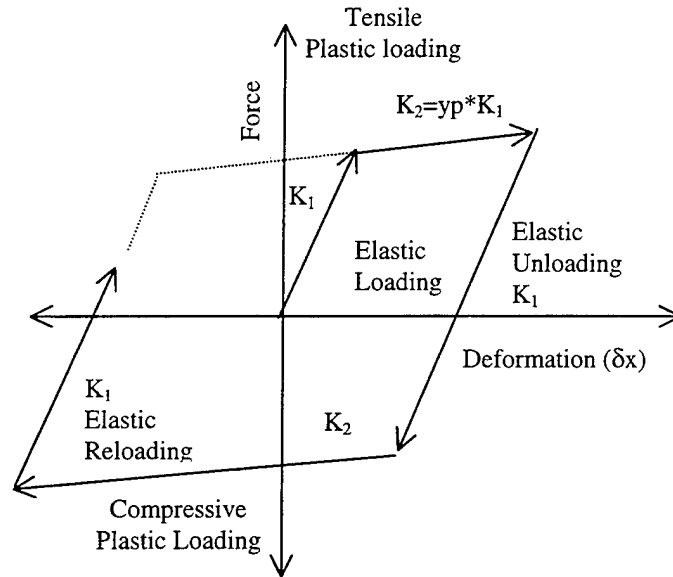


Figure 5. Bilinear Hysteretic Loop

Where K_1 and K_2 are the two distinct stiffness constants and the variable, y_p , is the yield to post ratio parameter.

2. Elastomeric Isolators

Elastomeric bearings are engineered from synthetic rubbers. The properties of the bilinear hysteresis loop can be readily designed and manufactured with the use of synthetic rubbers. These devices, known as High Damping Elastomeric Bearings (HDEB), are frequently used in both structural and industrial use. A comprehensive study conducted in [Ref. 12] validates work on performance and efficiency issues between polymer type bearings and High Damping Rubber Bearings (HDRB). The only

disadvantage of polymer synthetic rubber isolators is that over time the tensile and tear strengths become degraded.

3. Hysteretic Isolators

Not including the HDEB or HDRB devices, hysteretic bearings are developed using metals or composites such as the lead core rubber isolator. By varying materials and manufacturing processes a wide variety of hysteretic curves can be engineered. Modeling hysteretic systems is mathematically challenging due to the nonlinear governing equations. An accepted mathematical model to Figure 3 above, is the Wen nonlinear Equation [Ref.13]. The equation is very adaptive to various hysteretic type bearings. Another model, not used in this paper, is known as the Ozdemir element [Ref.14]. This mathematical model is based on similar principles as the Wen element however; it incorporates modifications to allow for Shape Memory Alloy (SMA) device modeling.

D. MATHEMATICAL MODELS

The general formulations of the mathematical models below are developed in previous works outlined in the respective subsection's reference remarks. The presentation of the equations represents general summaries of their work.

1. Bilinear Element

The bilinear element's hysteretic loop is shown above, in Figure 5, and is an approximation to the dynamic hysteretic loop as shown in Figure 4 above. The hysteretic loop is a function of displacement and velocity across the isolator, primary spring stiffness, and the secondary spring stiffness. Program code for the hysteretic loop is

formulated using basic logical algorithms, and is executed at the given time step interval over the time span.

In developing the algorithm for the hysteresis loop it is evident that the loop is a combination of 4 intersecting linear lines. Additionally, the restorative force is a function of the spring constant, displacement, velocity, previous deformation state position, and the intercept. Ultimately, to identify which part of the hysteresis loop that the current deformation data is on, a set of memorized variables is required. The memorized set of variables stores which leg the last deformation state was at and the force intercepts of the 4 lines.

As an example, an isolator in equilibrium is subjected to a sinusoidal base excitation. Assuming that the excitation begins in the positive direction the initial velocity and displacement are positive. Given the primary stiffness as K_1 , the force is calculated from Equation (9).

$$F = K_1 \Delta x + B_1$$

(9)

Since the equilibrium position was at zero velocity and zero displacement the value of B_1 is zero. If the calculated force from Equation (9) is less than a specified positive transition force, F_{\max} , the intercept, B_2 , for the subsequent leg is simultaneously calculated. This is conducted by numerically solving for the linear equation with a slope of K_2 that intersects the calculated F and Δx position. When the force, calculated in Equation (9), is greater than the transition force, F_{\max} , Equation (10) is used.

$$F = K_2 \Delta x + B_2 \tag{10}$$

Continuing along this leg the slope of the next leg, B_3 , is simultaneously calculated until the velocity becomes negative and the isolator begins to unload. At which point Equation (11) is used.

$$F = -K_1 \Delta x + B_3 \quad (11)$$

As the deformation progresses along this leg the next leg's intercept, B_4 is calculated as before. Upon surpassing the negative transition force, $-F_{\max}$, Equation (12) is used.

$$F = -K_2 \Delta x + B_4 \quad (12)$$

The loop continues until the end of the time history is reached. Additionally, at each time step, the intercepts and a location variable are updated and stored. Furthermore, reloading and unloading along the same leg is also possible given the data stored at each step.

The two distinct types of bilinear elements used in this paper are referred to as "ideal" and "real." The real isolator models the basic stress-strain curve, where the isolator is allowed to strain harden. Therefore, upon successive reload in either the tensile or compressive direction the yield force is increased. The ideal isolator is not allowed to strain harden and hence has constant positive and negative transition forces.

The algorithm of the example above is presented in Figure 6. Incorporating this algorithm into the recursive block-by-block formulation is easily conducted because the stored data is passed from block to block. However, since the process within a specific block is iterative the final block's data is not updated until the respective block has converged.

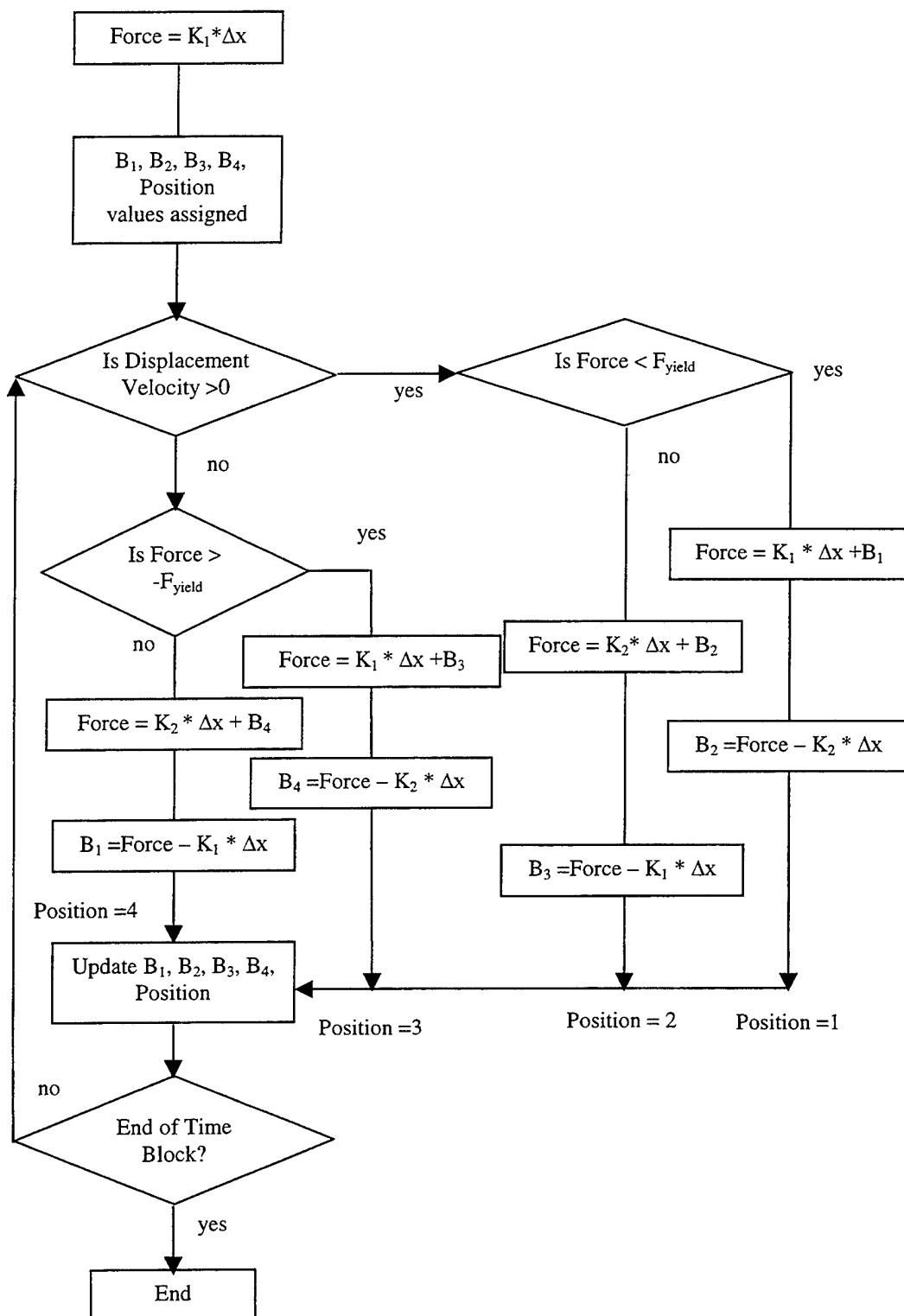


Figure 6. Bilinear Algorithm

2. Wen Element

As stated earlier, the Wen element is a mathematical equation that accurately models the hysteretic behavior of nonlinear isolators. The Wen nonlinear equation takes the bilinear hysteretic loop from Figure 4 and generates a more realistic hysteresis. The Wen element refines the bilinear element's hysteretic loop through variation of the input parameters, as seen in Figure 7.

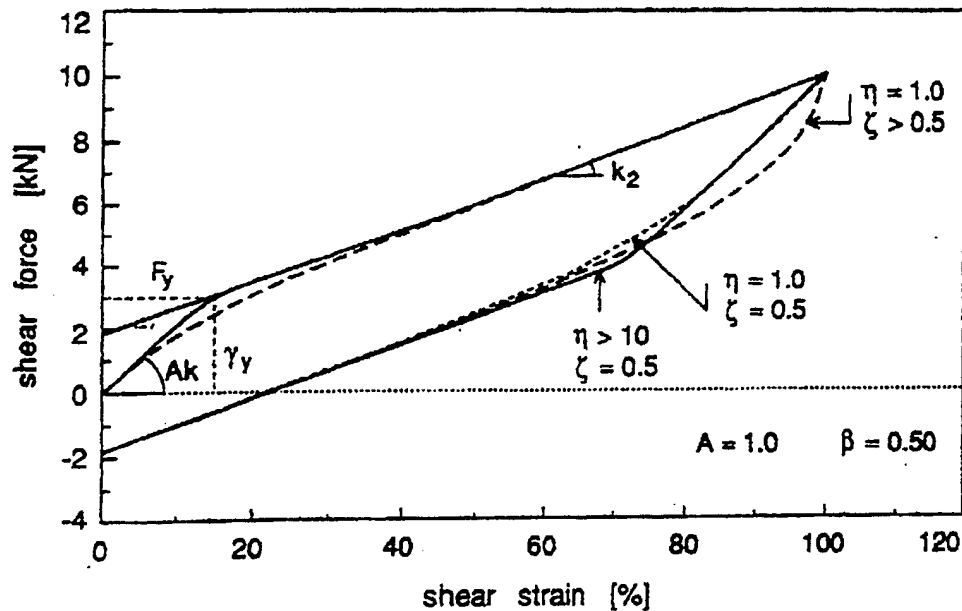


Figure 7. Parameters of the Wen's Model From Ref. [14:p. 355]

The non-dimensional coefficients A , β , ζ , and η control the shape of the hysteresis loop. Parameter A influences the initial loading slope and subsequent unloading and reloading slopes. The ratio of ζ/β controls the unloading and reloading curvatures. The effect of $\zeta/\beta > 1$ is equivalent to increasing the (A) parameter and causing the loop to curve outward as seen in Figure 7 where $\zeta > 1$. The parameter η controls the

curves that join the load and unload curves and is best described as the elastic-plastic behavior of the material.

The general formula for calculating the restoring force is:

$$F(t) = \alpha \frac{F_y}{\delta_y} x(t) + (1 + \alpha) F_y z(t) \quad (13)$$

Where $\alpha \frac{F_y}{\delta_y} \delta(t)$ is the equivalent linear portion and $(1 + \alpha) F_y z(t)$ is the nonlinear portion. The symbol α , is the respective yield to post ratio parameter, and $z(t)$ is the dimensionless hysteretic displacement that is defined by the nonlinear equation:

$$\frac{dz(t)}{dx} \delta_y = \left\{ A - |z(t)|^\eta \left[\beta + \text{sign} \left(z(t) \frac{dx(t)}{dt} \right) \zeta \right] \right\} \quad (14)$$

Where, $x(t)$ represents the strain. Rearranging Equation (14) and substituting the variable notation of ζ with γ in Equation (14) the equivalent Equations (15) and (16) are adopted from [Ref. 13:p. 250].

$$\dot{z}(t) = -\gamma \left| \dot{x}(t) \right| z(t)^{n-1} |z(t)| - \beta \dot{x}(t) |z(t)|^n + A \dot{\delta}(t) \text{ for } n = \text{even} \quad (15)$$

$$\dot{z}(t) = -\gamma \left| \dot{x}(t) \right| z(t)^n - \beta \dot{x}(t) |z(t)|^n + A \dot{x}(t) \text{ for } n = \text{odd} \quad (16)$$

A more refined formula for the dimensionless hysteretic displacement $z(t)$, from [Ref. 15:p. 79], is used in this study.

$$\dot{z} = -\gamma \left| \dot{x} \right| z |z|^{n-1} - \beta \dot{x} |z|^n + A \dot{x} \quad (17)$$

The combination of the nonlinear parameters from Equation (17) yields the maximum value of the restoring force.

$$F_{\max} = \left[\frac{A}{\gamma + \beta} \right]^{\frac{1}{\eta}} \quad (18)$$

To reinforce the effects of each of the respective Wen nonlinear equation parameters graphical representations are presented. An arbitrary hysteretic isolator was chosen and a sinusoidal displacement was imposed. Figure 8 illustrates the hysteresis loop for the isolator and sinusoidal excitation.

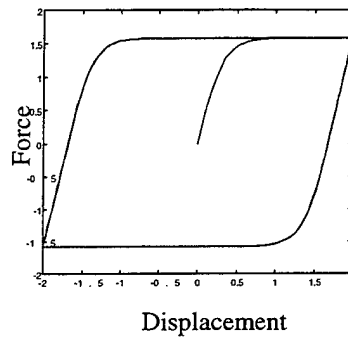


Figure 8. Wen Element Hysteresis Loop for $F_y=1$, $A=2$, $\eta=2$, $\beta=1$, $\gamma=1$, $\delta_y=1$, $\alpha=.01$ due to Unit Sinusoidal Excitation at .5 Hz

By varying the constant parameters in Equations (14) and (17), the effects, delineated by the dashed lines, are presented in Figure 9.

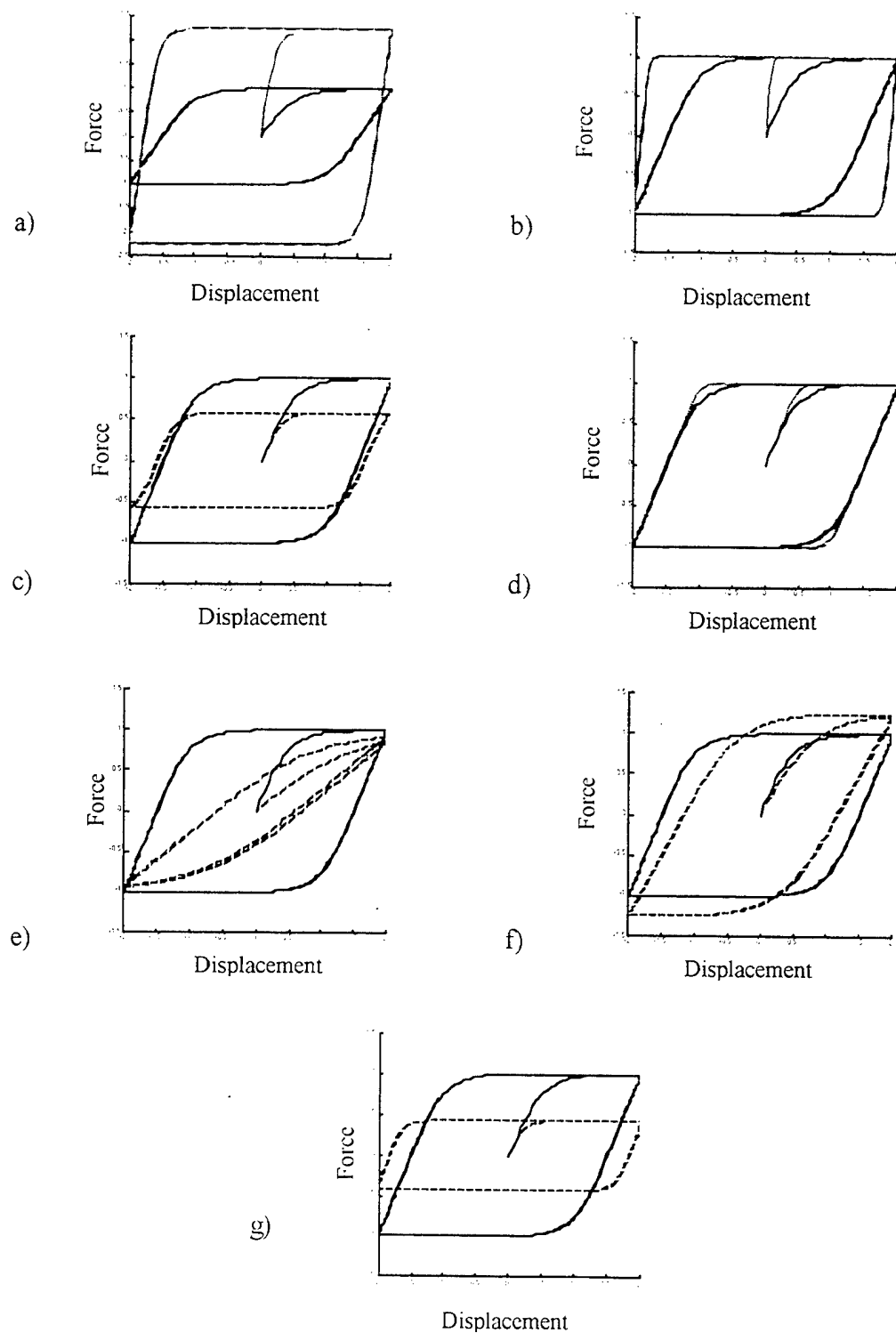


Figure 9. Parameter Change Effects On Wen Hysteresis, a) Increase F_y b) Increase A , c) Increase β , d) Increase η , e) Increase δ_y , f) Increase α , g) Increase γ

3. Maxwell Element

The Maxwell element is another type of nonlinear isolator that is constructed from a linear spring and viscous damper in series vice in parallel as in a common shock absorber. The formulation was developed in [Ref.14] and is included in the code to provide an additional nonlinear element. Although viscous dampers and shock absorbers are frequency dependant, the overall nonlinearity makes them sufficiently more efficient in energy dissipation then a linear spring. By placing the spring and viscous damper in series the isolator becomes frequency independent.

The nonlinear restorative force equation is:

$$\dot{F}(t) = -\frac{k}{c} F(t) + k \dot{\delta}(t) \quad (19)$$

E. LOAD DEPENDANT ISOLATORS

Devices that are used in structural applications not only require horizontal stiffness but also vertical stiffness as well. The initial loading as well as uplift loads on the isolator plays an important role in establishing the horizontal or shear stiffness of the bearing. The broad effects of vertical displacements on rubber and elastomeric isolators are well documented in [Ref. 9:p. 170], [Ref. 16], and [Ref. 17] and are broadly summarized in this section.

For an isotropic material the loading versus the stiffness function is similar to the curve outlined in Figure 11.

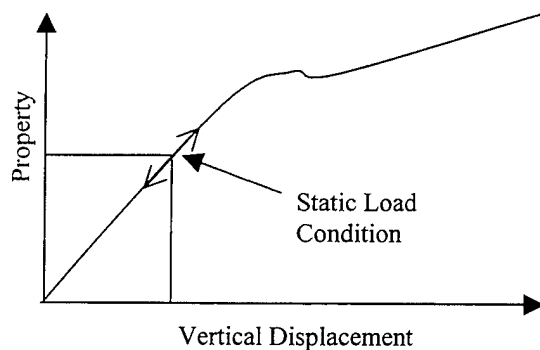


Figure 11. Isolator's Properties Versus Vertical Displacements

For small vertical displacements the change in the isolator loads will be small enough that the parameters will be dictated by it's elastic range. Since the vertical spring component of the isolator will generally obeys Hooks law.

$$\sigma = E \varepsilon \quad (20)$$

Where σ represents the stress, ε the strain, and E the elastic modulus. The properties of the isolator are then determined by the vertical displacements.

Generally, when the isolator has been loaded it has stored elastic energy. Rubber is particularly strain sensitive which causes the shear modulus, G , to change according to the strains imparted due to the connections to the building and ground bearing, represented by Figure 12.

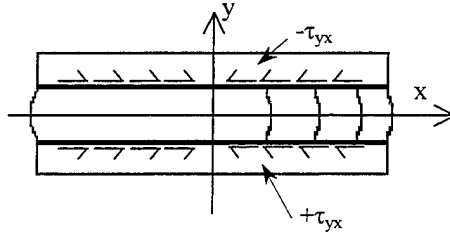


Figure 12. Shear Stresses on a Load Isolator From [Ref. 9:p.142]

The comparison of the total elastic stored energy caused by the shear forces on the top and bottom surfaces to the energy obtained from the average shear strain within the isolator will influence the overall effective shear modulus.

$$\gamma_{ave}^2 = \frac{1}{G^2 A t} \int \int (\tau_{xz}^2 + \tau_{yx}^2) dy dA \quad (21)$$

Where, A is the cross sectional area of the isolator, and t the thickness. Depending on the type of isolator, the values of the average shear strain can be calculated and the resultant G could then be iterated since G is also a function of ϵ_c (compression strain).

Expanding the system to more complex systems such as anisotropic materials like composites requires a more detailed knowledge of the property versus loading curves. Even a simple model can lead to complex numerical formulations if the transition was made into the plastic region. This could easily lead to a hysteretic behavior in the vertical component due to the continuous loading and reloading in the plastic range.

III. EQUATIONS OF MOTION AND NONLINEAR ISOLATORS

Generating the equations of motion of an arbitrary n -degree of freedom structure allows the structure to be described both statically and dynamically in a finite mathematical manner. By modeling the structure and directly controlling the number of degrees of freedom (DOF), the number of differential equations becomes finite and manageable. The left hand side of the equations of motion becomes the representation of the elastic-linear structure while the right hand side captures all the forces generated from the linear and nonlinear attributes of the isolators.

A. GOVERNING EQUATIONS

Developing a FE model of a structure is covered in various texts [Ref. 18] and the basic structural dynamic formulation is covered in [Ref. 19]. The work in this section is a basic summary of work developed in these references.

Taking a continuous model, which has an infinite number of DOF, and converting it to a workable yet realistic mathematical model is the goal of FE techniques. In order to determine the discretization of the structure a logical determination has to be made in respect to retaining a sufficient number of degree of freedoms. The structure can then be describe by a continuous mathematical model and is formulated as a partial differential equation (PDE). Avoiding the computational effort associated with a PDE, the system is transformed into a set of 2^{nd} order ordinary differential equations (ODE). The transformation is conducted by using elements of lumped-parameter models. The formulation is covered in many vibration and dynamic analysis textbooks as in [Ref. 6] and [Ref. 19] and is summarized below. Additionally, it is computationally useful to

transform the coupled ODE into modal space to achieve uncoupled ODEs. Again, these methods are well documented and are used in summary in this formulation.

For an arbitrary base isolated structure the free-free structure is connected to the base isolators as shown in Figure 12.

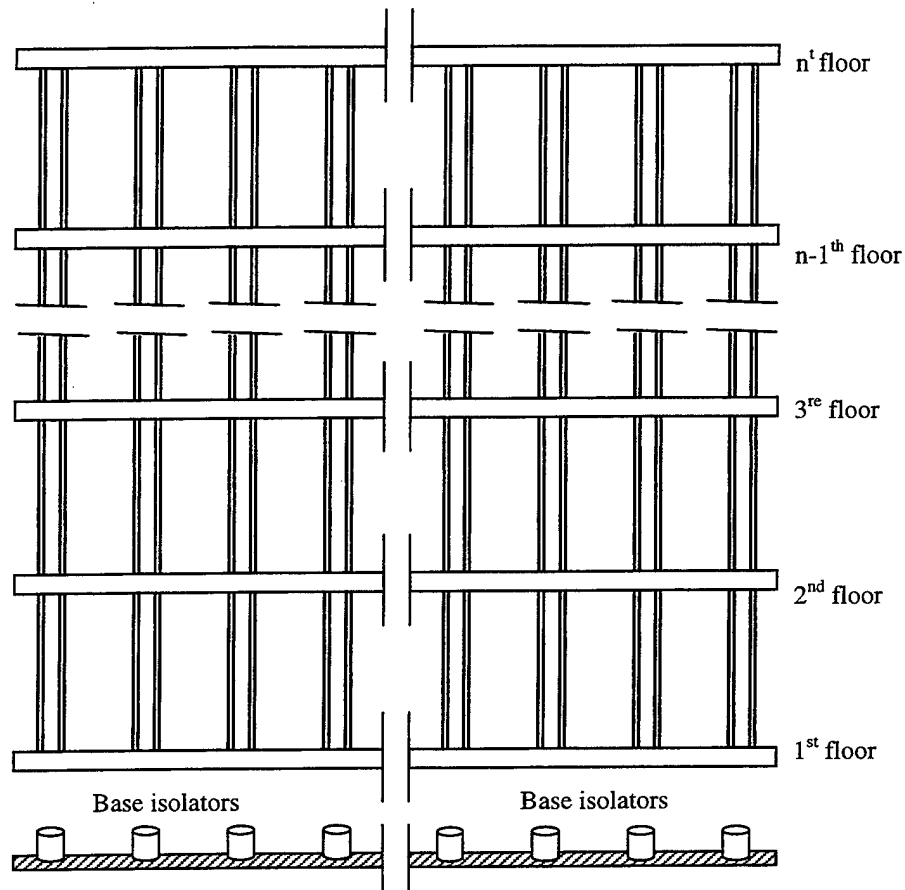


Figure 12. N-Story Base Isolated Structure

The structure's nodal degrees of freedom that connect to the isolator are contained in the vector (Cset). (Cset) can contain all six degrees of freedom per node but generally the lateral and vertical degree of freedoms are chosen for base isolation.

The governing equations of motion, assuming proportional structural damping, [Ref.4:p. 176], for the coupled free-free structure and the isolators, is presented in Equation (22):

$$[M]_{n \times n} \begin{Bmatrix} \ddot{x} \\ \ddot{x} \end{Bmatrix}_{n \times 1} + [C]_{n \times n} \begin{Bmatrix} \dot{x} \\ \dot{x} \end{Bmatrix}_{n \times 1} + [K]_{n \times n} \{x\}_{n \times 1} = \{F_{Cset}^{iso}\}_{n \times 1} \quad (22)$$

Where, (n) represents the total number of degrees of freedom in the system and the forcing function, $F_{Cset}^{iso}(t)$, contains the external isolator forces of length (Cset) and zeros for non-coupled degrees of freedom. The general solution to the second order differential equation is of the form:

$$x(t) = x(t)_h + x(t)_p \quad (23)$$

The homogenous solution for particular degree of freedom becomes:

$$x = e^{-\zeta \omega_n t} (A \sin \sqrt{1 - \zeta^2} \omega_n t + B \cos \sqrt{1 - \zeta^2} \omega_n t) \quad (24)$$

The derivation of the particular solution depends upon the arbitrary forcing function. For simple forces such as linear springs the solution becomes trivial through the manipulation of Equation (22). However, for nonlinear elements the particular solution can be significantly complex.

A method to directly solve Equation (22) is to transform the second order differential equation into two coupled single ODEs. Pre-multiplying Equation (22) by $[M]^{-1}$ and moving the stiffness and damping components to the right yields:

$$\begin{Bmatrix} \dot{x} \\ \dot{x} \end{Bmatrix} = -[M]^{-1} [C] \begin{Bmatrix} \dot{x} \\ \dot{x} \end{Bmatrix} - [M]^{-1} [K] \{x\} + [M]^{-1} \{F_{Cset}^{iso}\} \quad (25)$$

The two-coupled single ODEs that represent Equation (25) are:

$$\begin{aligned}\begin{Bmatrix} \dot{x} \\ \dot{s} \end{Bmatrix} &= \begin{Bmatrix} s \end{Bmatrix} \\ \begin{Bmatrix} \dot{s} \end{Bmatrix} &= -[M]^{-1}[C]\begin{Bmatrix} \dot{x} \end{Bmatrix} - [M]^{-1}[K]\begin{Bmatrix} x \end{Bmatrix} + [M]^{-1}[F_{Cset}^{iso}]\end{aligned}\quad (26)$$

The solution to Equation (26) can be easily completed using any validated ODE solver, however, it can become significantly problematic if the forcing matrix $[M]^{-1}\{F_{Cset}^{iso}\}$ is nonlinear.

B. VOLTERRA INTEGRAL FORMULATION

The solution of Equation (22) can also be obtained using the Volterra integral method. The method of solving for the particular solution of Equation (22) is conducted using the convolution integral. The derivation of the convolution integral is developed in various vibration textbooks such as [Ref. 6], and is formulated as:

$$x(t) = \int_{-\infty}^t f(\tau)h(t-\tau)d\tau \quad (27)$$

Where, $h(t-\tau)$, is the impulse response function defined as:

$$h(t) = \frac{x(t)}{\hat{F}} = \frac{e^{-\zeta\omega_n t}}{\omega_n \sqrt{1-\zeta^2}} \sin \omega_n \sqrt{1-\zeta^2} t \quad (28)$$

Where ω_n represents the natural frequency, and ζ the damping coefficient. In order to sum each discretized time band to yield the entire displacement time history the system must be physically realizable:

$$x(t) = \sum_0^{\infty} f(\tau)h(t-\tau)\Delta\tau = \int_0^t f(\tau)h(t-\tau)d\tau \quad (29)$$

Substituting the particular solution into Equation (23), the complete solution to the general equation of motion reduces to:

$$\begin{Bmatrix} x_1 \\ x_2 \\ \vdots \\ x_m \end{Bmatrix} = \begin{Bmatrix} x_1 \\ x_2 \\ \vdots \\ x_m \end{Bmatrix}_h + \int_0^t \begin{bmatrix} h_{11}(t-\tau) & h_{12}(t-\tau) & \cdots & h_{1n}(t-\tau) \\ h_{12}(t-\tau) & h_{22}(t-\tau) & \cdots & h_{2n}(t-\tau) \\ \vdots & \vdots & \ddots & \vdots \\ \vdots & \vdots & \cdots & \vdots \\ h_{1n}(t-\tau) & h_{2n}(t-\tau) & \cdots & h_{nn}(t-\tau) \end{bmatrix} \begin{Bmatrix} F_1^{iso}(\tau) \\ F_2^{iso}(\tau) \\ \vdots \\ 0 \end{Bmatrix} d\tau \quad (30)$$

The resultant equation is the non-homogenous Volterra integral equation as the forcing vector $F_1^{iso}(\tau)$ is a (nonlinear) function of the response and its derivative. The forcing vector $F_1^{iso}(\tau)$ represents the isolator force due to ground excitation on the DOF denoted in the subscript. In order to reduce the computational effort for Equation (30), Equation (22) is transformed into modal space. The transformation equation is defined as:

$$x_i = \sum_{j=1}^n \Phi_i^j q_j^i \quad (31)$$

Where, n is the number of modes, i is the i^{th} DOF, and j is the j^{th} mode.

Pre-multiply Equation (24) with the transpose of the mass normalized mode shape matrix, $[\Phi]^T$, the modal space equivalent is:

$$\begin{Bmatrix} \ddot{q}_1 \\ \ddot{q}_2 \\ \vdots \\ \ddot{q}_n \end{Bmatrix} + \begin{bmatrix} 2\zeta_1\omega_1 & 0 & \cdots & 0 \\ 0 & 2\zeta_2\omega_2 & \cdots & 0 \\ \vdots & \vdots & \ddots & \vdots \\ 0 & 0 & \cdots & 2\zeta_n\omega_n \end{bmatrix} \begin{Bmatrix} \dot{q}_1 \\ \dot{q}_2 \\ \vdots \\ \dot{q}_n \end{Bmatrix} + \begin{bmatrix} \omega_1^2 & 0 & \cdots & 0 \\ 0 & \omega_2^2 & \cdots & 0 \\ \vdots & \vdots & \ddots & \vdots \\ 0 & 0 & \cdots & \omega_n^2 \end{bmatrix} \begin{Bmatrix} q_1 \\ q_2 \\ \vdots \\ q_n \end{Bmatrix} = \begin{bmatrix} \Phi_1^1 & \Phi_1^2 & \cdots & \Phi_1^n \\ \Phi_2^1 & \Phi_2^2 & \cdots & \Phi_2^n \\ \vdots & \vdots & \ddots & \vdots \\ \Phi_n^1 & \Phi_n^2 & \cdots & \Phi_n^n \end{bmatrix} \begin{Bmatrix} F_1 \\ F_2 \\ \vdots \\ F_n \end{Bmatrix} \quad (32)$$

The modal solution of Equation (32) yields the equivalent Volterra integral form of Equation (33):

$$\begin{Bmatrix} q_1 \\ q_2 \\ \vdots \\ q_m \end{Bmatrix} = \begin{Bmatrix} q_1 \\ q_2 \\ \vdots \\ q_m \end{Bmatrix}_h + \int_0^t \begin{bmatrix} h_{11}(t-\tau) & 0 & \cdots & 0 \\ 0 & h_{22}(t-\tau) & \cdots & 0 \\ \vdots & \vdots & \ddots & \vdots \\ 0 & 0 & \cdots & h_{nn}(t-\tau) \end{bmatrix} \begin{bmatrix} \Phi_1^1 & \Phi_1^2 & \cdots & \Phi_1^n \\ \Phi_2^1 & \Phi_2^2 & \cdots & \Phi_2^n \\ \vdots & \vdots & \ddots & \vdots \\ \Phi_n^1 & \Phi_n^2 & \cdots & \Phi_n^n \end{bmatrix} \begin{Bmatrix} F_1^{iso}(\tau) \\ F_2^{iso}(\tau) \\ \vdots \\ 0 \end{Bmatrix} d\tau \quad (33)$$

Since, the system of equations was transformed into modal space the impulse response matrix is uncoupled and is denoted by the (\sim) symbol. Transforming Equation (33) back into normal space by substituting in Equation (31) yields:

$$\begin{Bmatrix} x_1 \\ x_2 \\ \vdots \\ x_m \end{Bmatrix} = \begin{Bmatrix} x_1 \\ x_2 \\ \vdots \\ x_m \end{Bmatrix}_h + \left[\begin{Bmatrix} \Phi_1^1 \\ \Phi_1^2 \\ \vdots \\ \Phi_1^n \end{Bmatrix} \begin{Bmatrix} \Phi_2^1 \\ \Phi_2^2 \\ \vdots \\ \Phi_2^n \end{Bmatrix} \dots \begin{Bmatrix} \Phi_m^1 \\ \Phi_m^2 \\ \vdots \\ \Phi_m^n \end{Bmatrix} \right] \int_0^t \begin{bmatrix} \tilde{h}_{11}(t-\tau) & 0 & \dots & 0 \\ 0 & \tilde{h}_{22}(t-\tau) & \dots & 0 \\ \vdots & \vdots & \ddots & \vdots \\ 0 & 0 & \dots & \tilde{h}_{nn}(t-\tau) \end{bmatrix} \begin{bmatrix} \Phi_1^1 & \Phi_1^2 & \dots & \Phi_1^n \\ \Phi_2^1 & \Phi_2^2 & \dots & \Phi_2^n \\ \vdots & \vdots & \ddots & \vdots \\ \Phi_m^1 & \Phi_m^2 & \dots & \Phi_m^n \end{bmatrix} \begin{Bmatrix} F_1^{iso}(\tau) \\ F_2^{iso}(\tau) \\ \vdots \\ 0 \end{Bmatrix} d\tau \quad (34)$$

Equation (34) contains ($n + m$) unknowns and (n) coupled equations, where (n) represents the total number of nodes and (m) the number of nodal values contained in (Cset). Clearly, we have more unknowns than equations to easily substitute values in and achieve a simple solution. However, since there are only (m) linear or nonlinear forces, a recursive iterative solution process can be conducted solely on a reduced (m) sized system of coupled equations. The set of reduced nodes, (Cset), contains the associated connected base nodes denoted on the subscript of $F_1^{iso}(\tau)$. Therefore, the number of equations reduces to (m) and the number of unknowns reduces to ($2m$). This reduction can dramatically reduce the solution time in comparison to methods that solve the entire (n) governing ordinary differential equations.

Therefore, Equation (34) reduces to:

$$\begin{Bmatrix} x_1 \\ x_2 \\ \vdots \\ x_m \end{Bmatrix} = \begin{Bmatrix} x_1 \\ x_2 \\ \vdots \\ x_m \end{Bmatrix}_h + \left[\begin{Bmatrix} \Phi_1^1 \\ \Phi_1^2 \\ \vdots \\ \Phi_1^n \end{Bmatrix} \begin{Bmatrix} \Phi_2^1 \\ \Phi_2^2 \\ \vdots \\ \Phi_2^n \end{Bmatrix} \dots \begin{Bmatrix} \Phi_m^1 \\ \Phi_m^2 \\ \vdots \\ \Phi_m^n \end{Bmatrix} \right] \int_0^t \begin{bmatrix} \tilde{h}_{11}(t-\tau) & 0 & \dots & 0 \\ 0 & \tilde{h}_{22}(t-\tau) & \dots & 0 \\ \vdots & \vdots & \ddots & \vdots \\ 0 & 0 & \dots & \tilde{h}_{nn}(t-\tau) \end{bmatrix} \begin{bmatrix} \Phi_1^1 & \Phi_1^2 & \dots & \Phi_1^n \\ \Phi_2^1 & \Phi_2^2 & \dots & \Phi_2^n \\ \vdots & \vdots & \ddots & \vdots \\ \Phi_m^1 & \Phi_m^2 & \dots & \Phi_m^n \end{bmatrix} \begin{Bmatrix} F_1^{iso}(\tau) \\ F_2^{iso}(\tau) \\ \vdots \\ F_m^{iso}(\tau) \end{Bmatrix} d\tau \quad (35)$$

By employing modal participation methods, the computational effort in solving Equation (57) can further be reduced. It is shown, [Ref. 4:ch. 6], that for a system

transformed into the frequency domain that for a specified nodal maximum displacement to a particular (p) mode is as follows:

$$|x_i|_{\max} = |\Phi_i^i q_i| + \sqrt{|\Phi_i^1 q_1|^2 + |\Phi_i^2 q_2|^2 + \dots + |\Phi_i^{i-1} q_{i-1}|^2 + |\Phi_i^{i+1} q_{i+1}|^2 \dots + |\Phi_i^n q_n|^2} \quad (36)$$

Where, the superscript identifies the mode, the subscript identifies the node, and (n) the total number of modes. From the resultant frequency response spectrum, the contributions of the modes closest to the mode in question will have the most significant impact. Therefore, the transformation matrix $[\Phi]$, is further reduced from a (n x m) matrix into one that is (m x r). Where, (r) represents the number of modes retained.

The time domain normal mode truncation method approaches the number of modes retained in a similar manner. For example, using the i^{th} DOF's modal displacement time history solution, defined by Equation (39), it is obvious that the more modes retained the accuracy of the solution increases.

$$x_i(t) = \Phi_i^1 q_1(t) + \Phi_i^2 q_2(t) + \Phi_i^3 q_{31}(t) + \dots + \Phi_i^n q_n(t) \quad (37)$$

However, truncating to a sufficient number of modes with an acceptable error, can reduce the computational effort dramatically.

Equation (35) now reduces to the reduced Volterra integral form:

$$\begin{Bmatrix} x_1 \\ x_2 \\ \vdots \\ x_m \end{Bmatrix} = \begin{Bmatrix} x_1 \\ x_2 \\ \vdots \\ x_m \end{Bmatrix}_h + \begin{Bmatrix} \Phi_1^1 \\ \Phi_1^2 \\ \vdots \\ \Phi_m^1 \\ \Phi_m^2 \\ \vdots \\ \Phi_m^r \end{Bmatrix} \begin{Bmatrix} \Phi_1^2 \\ \Phi_2^2 \\ \vdots \\ \Phi_m^2 \end{Bmatrix} \dots \begin{Bmatrix} \Phi_1^r \\ \Phi_2^r \\ \vdots \\ \Phi_m^r \end{Bmatrix} \int_0^t \begin{bmatrix} h_{11}(t-\tau) & 0 & \dots & 0 \\ 0 & h_{22}(t-\tau) & \dots & 0 \\ \vdots & \vdots & \dots & \vdots \\ 0 & 0 & \dots & h_{rr}(t-\tau) \end{bmatrix} \begin{bmatrix} \Phi_1^1 & \Phi_1^2 & \dots & \Phi_m^1 \\ \Phi_1^2 & \Phi_2^2 & \dots & \Phi_m^2 \\ \vdots & \vdots & \dots & \vdots \\ \Phi_1^r & \Phi_2^r & \dots & \Phi_m^r \end{bmatrix} \begin{Bmatrix} F_1^{iso}(\tau) \\ F_2^{iso}(\tau) \\ \vdots \\ F_m^{iso}(\tau) \end{Bmatrix} d\tau \quad (38)$$

In order to reduce Equation (38) to represent a single i^{th} DOF time history, the equation is simplified by multiplying the matrices $[\Phi][h][\Phi]^T$. Multiplying out $[\Phi][h]$ yields:

$$\begin{Bmatrix} x_1 \\ x_2 \\ \vdots \\ x_m \end{Bmatrix} = \begin{Bmatrix} x_1 \\ x_2 \\ \vdots \\ x_m \end{Bmatrix}_h + \int_0^t \begin{bmatrix} \Phi_1^1 \tilde{h}_{11}(t-\tau) & \Phi_1^2 \tilde{h}_{22}(t-\tau) & \dots & \Phi_1^r \tilde{h}_{rr}(t-\tau) \\ \Phi_2^1 \tilde{h}_{11}(t-\tau) & \Phi_2^2 \tilde{h}_{22}(t-\tau) & \dots & \Phi_2^r \tilde{h}_{rr}(t-\tau) \\ \vdots & \vdots & \ddots & \vdots \\ \Phi_r^1 \tilde{h}_{11}(t-\tau) & \Phi_r^2 \tilde{h}_{22}(t-\tau) & \dots & \Phi_r^r \tilde{h}_{rr}(t-\tau) \end{bmatrix} \begin{bmatrix} \Phi_1^1 & \Phi_1^2 & \dots & \Phi_1^r \\ \Phi_2^1 & \Phi_2^2 & \dots & \Phi_2^r \\ \vdots & \vdots & \ddots & \vdots \\ \Phi_r^1 & \Phi_r^2 & \dots & \Phi_r^r \end{bmatrix} \begin{Bmatrix} F_1^{iso}(\tau) \\ F_2^{iso}(\tau) \\ \vdots \\ F_m^{iso}(\tau) \end{Bmatrix} d\tau \quad (39)$$

Continuing, the time history nodal response for the i^{th} DOF yields:

$$x_i(t) = x_{ih}(t) + \int_0^t \sum_{j=1}^r \Phi_i^j \Phi_1^j \tilde{h}_{jj}(t-\tau) F_1^{iso}(\tau) d\tau + \int_0^t \sum_{j=1}^r \Phi_i^j \Phi_2^j \tilde{h}_{jj}(t-\tau) F_2^{iso}(\tau) d\tau + \dots \\ \int_0^t \sum_{j=1}^r \Phi_i^j \Phi_m^j \tilde{h}_{jj}(t-\tau) F_m^{iso}(\tau) d\tau \quad (40)$$

Where, the notational superscript indicates the respective retained modes and the subscript identifies with the DOF values, (i), in (Cset). Therefore, the summation notation for (j) signifies that the associated DOFs, contained in (Cset), is summed over the total number of modes retained from truncation.

C. RECURSIVE ITERATION FORMULATION

By employing modal truncation and retaining the (Cset) sized set of equations, the overall computational effort has been dramatically reduced. The solution of the (m)-coupled equations is conducted in a recursive iterative manner. From Equation (40), the transient response for a particular nodal degree of freedom is dominated by the convolution integrals. The isolator forces, $F_m^{iso}(\tau)$, within the respective integrals are unknown. Therefore, in order to solve for the $x_i(t)$ nodal degree of freedom time history an initial guess is conducted. For a simple linear isolator the linear approximation can be represented as:

$$F_i^{iso} = -K_{iso}(x_i - x_g) \quad (41)$$

Where, K_{iso} represents the linear stiffness, the subscript (i) the nodal DOF, and x_g the ground motion. Substituting all the isolator forces into Equation (40) yields:

$$x_i(t) = \int_0^t \sum_{j=1}^r \Phi_i^j \Phi_1^j \tilde{h}_{jj}(t-\tau) (-K_{iso}(x_1(\tau) - x_g(\tau))) d\tau + \dots$$

$$\int_0^t \sum_{j=1}^r \Phi_i^j \Phi_m^j \tilde{h}_{jj}(t-\tau) (-K_{iso}(x_m(\tau) - x_g(\tau))) d\tau \quad (42)$$

The solution for any one nodal DOF then becomes a function of all the (Cset) unknown DOF displacements. To achieve a solution a recursive iterative process is employed for each nodal DOF. Therefore, Equation (42) is rewritten as:

$$x_i^{new}(t) = \int_0^t \sum_{j=1}^r \Phi_i^j \Phi_1^j \tilde{h}_{jj}(t-\tau) (-K_{iso}(x_1^{last}(\tau) - x_g(\tau))) d\tau + \dots$$

$$\int_0^t \sum_{j=1}^r \Phi_i^j \Phi_m^j \tilde{h}_{jj}(t-\tau) (-K_{iso}(x_m^{last}(\tau) - x_g(\tau))) d\tau \quad (43)$$

The recursive iteration process uses the $x_m^{last}(\tau)$ values to solve for the $x_m^{new}(\tau)$ values. The iterative process begins by assigning initial arbitrary values to $x_1^{last}(\tau)$ through $x_m^{last}(\tau)$. These values are then substituted into Equation (43) and the resultant $x_m^{new}(\tau)$ values are computed. A tolerance check is conducted between $x_m^{last}(\tau)$ and $x_m^{new}(\tau)$, if the criteria is not met the $x_m^{last}(\tau)$ values are updated to the $x_m^{new}(\tau)$ values. The process continues until tolerance is met. An algorithm of the iterative recursive method is presented in Figure 13.

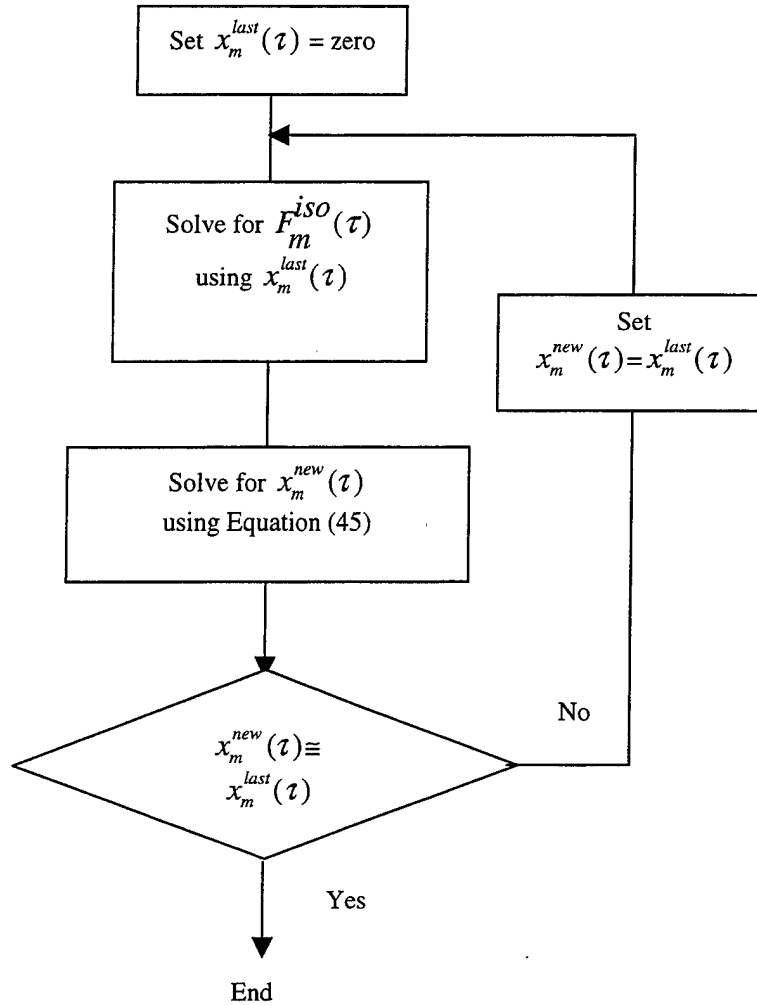


Figure 13. Basic Recursive Iteration Algorithm

D. LINEAR AND NONLINEAR RECURSIVE BLOCK BY BLOCK SYNTHESIS

The algorithm used to solve the governing Volterra integral can still be computationally exhaustive for large, finely discretized time spans and or large (Cset) DOF systems. For physically realizable systems the computational effort can be further decreased by recursive block-by-block iteration. The convolution integral can be divided

into blocks and summed up to arrive at the total solution. The blocks take advantage of the linear properties of the convolution integral.

By the formulation of the convolution integral, Equation (27), the transient response spanned over some period of time t , is the summation of the time histories of the arbitrary impulse forces acting at specified times, τ .

$$\int_0^t f(\tau)h(t-\tau)d\tau = \int_0^t f(0)h(t-\tau)d\tau + \int_1^t f(t_1)h(t-\tau)d\tau + \dots \int_n^t f(t_n)h(t-\tau)d\tau \quad (44)$$

Therefore, the incorporation of this linearity of the convolution integral into the recursive block-by-block method is presented. In general, each block will synthesize both a specified transient time history and an associated forcing function. The recursive process requires the use of all previous block's solutions to achieve the total solution. To represent the process Equation (44) can be rewritten to represent discrete block times as:

$$\begin{aligned} \int_0^t f(\tau)h(t-\tau)d\tau &= \int_0^{t_1} f(0\dots t_1)h(t-\tau)d\tau + \int_1^{t_2} f(t_1\dots t_2)h(t-\tau)d\tau + \dots \\ &\quad \int_n^t f(t_n\dots t)h(t-\tau)d\tau \end{aligned} \quad (45)$$

Where, the forcing functions $f(0\dots t_1)$ represent the block's synthesized force over the specified block time span. The recursive properties are not outwardly evident in the formulation of Equation (45) but is accounted for computationally for each successive block. To illustrate the process a system is synthesized using two blocks. Equation (45) reduces to:

$$\int_0^t f(\tau)h(t-\tau)d\tau = \int_0^{t_1} f(0\dots t_1)h(t-\tau)d\tau + \int_1^t f(t_1\dots t)h(t-\tau)d\tau \quad (46)$$

Computationally, Equation (44) is iterated and converged for the first block. The next block then proceeds to solve Equation (44) for the second time block. However, the first block's isolator forcing time history solution has to be extended over the second block:

$$\int_0^t f(\tau)h(t-\tau)d\tau = \int_0^{t_1} f(0...t_1)h(t-\tau)d\tau + \int_{t_1}^t f(0...t_1)h(t_1...t-\tau)d\tau \quad (47)$$

Here, $h(t_1...t-\tau)$ represents the impulse response function that begins at time t_1 vice zero. The time history, $x(t)$, for the extended time block $\int_{t_1}^t f(0...t_1)h(t_1...t-\tau)d\tau$ is the $x_m^{last}(\tau)$ of the next block. Although it can be generally said that any arbitrary $x_m^{last}(\tau)$ can be chosen for each successive blocks, a closer approximation to the solution can reduce the iterative process. More importantly, the computed extension is added to the final recursive iterated solution of the second block. The recursive block-by-block method algorithm is presented in Figure 14.

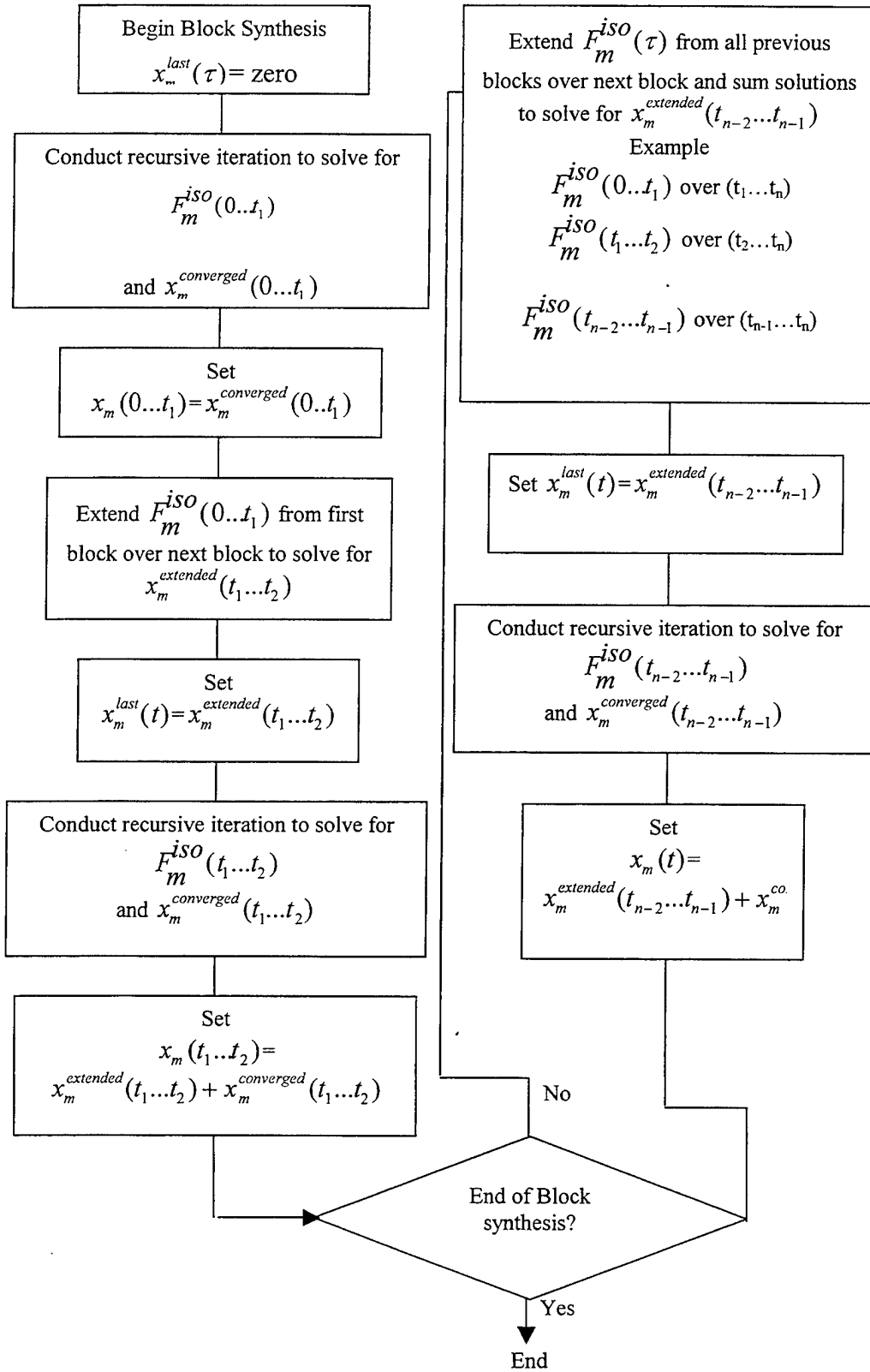


Figure 14. Recursive Block-by-Block Algorithm

For linear isolators such as the one presented in Equation (41) block-by-block iterations and block summations are straightforward. Each block follows the algorithm presented in Figure 16 and Figure 17. However, for nonlinear forces the recursive block-by-block synthesis relies more heavily upon the force solutions of the previous blocks.

A possible model of a nonlinear isolator is presented as:

$$F_i^{iso} = f((x_g - x_i^*), (\dot{x}_g - \dot{x}_i^*), (\ddot{x}_g - \ddot{x}_i^*), K_i(t), \dots) \quad (48)$$

Where the superscript * symbol indicates the iterated value achieved from the algorithm presented in Figure 16. For the nonlinear isolators presented a Runge-Kutta 4, (RK4), ODE solver is used.

Each successive block requires that the solution to the nonlinear equations have the correct initial conditions. Therefore, in order to achieve continuity of the isolator's hysteretic response between blocks, the initial condition is interpolated through a direct quadratic approximation through the last three force data points of the previous block, as shown in Figure 15.

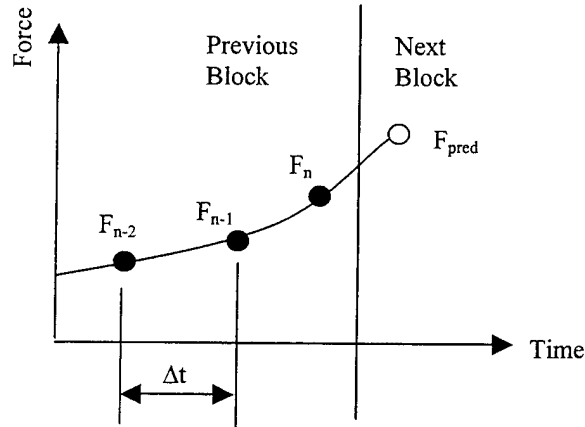


Figure 15. Recursive Interpolation

E. UPLIFT IN RECURSIVE BLOCK-BY-BLOCK SYNTHESIS

Beginning with Equation (42) the calculation of uplift requires the retention in the analysis of the vertical degrees of freedom. Therefore, if the original retained set of nodal degrees of freedom were limited to lateral displacements in (Cset), the new (Cset) would include the vertical DOFs associated with the Cset nodes. This would increase (Cset) by a factor of two. Including bi-directional excitation with uplift would then result in tripling the size of (Cset) [Ref. 20].

For different isolators the uplift properties and their effects on lateral stiffness is well documented in [Ref. 21], [Ref. 16], and [Ref. 17]. For simplicity the uplift portion of the synthesis was modeled as a linear spring:

$$F_i^{iso} = -K_{iso}(x_i^{vertical}) \quad (49)$$

Programming interpolating tables can easily be introduced in the developed program if known. Therefore, Equation (40) expands to include uplift synthesis:

$$x_i(t) = \text{Equation}(42) + \int_0^t \sum_{j=1}^r \Phi_i^j \Phi_{m+1}^j \tilde{h}_{jj}(t-\tau) F_{m+1}^{uplift}(\tau) d\tau + \dots$$

$$\int_0^r \sum_{j=1}^r \Phi_i^j \Phi_{2m}^j \tilde{h}_{jj}(t-\tau) F_{2m}^{iso}(\tau) d\tau \quad (50)$$

Additionally, since many of the parameters are uplift dependant the following isolator models are presented:

$$F_i^{iso} = -K_{iso}^* (x_i - x_g) \quad (51)$$

$$F_i^{iso} = f((x_g - x_i^*), (\dot{x}_g - \dot{x}_i^*), (\ddot{x}_g - \ddot{x}_i^*), K_i^*(t), \eta_i^*(t), \gamma_i^*(t)....) \quad (52)$$

Where, the superscript symbol, *, represents a now synthesized value as depicted in the linear approximation of slope (M) below:

$$Parameter_i^*(t) = Parameter_i^{original} + M(x_i^{vertical}(0) - x_i^{vertical}(t)) \quad (53)$$

F. SINGLE ISOLATION TRAPEZIODAL EXTRACTION

Given an arbitrary excitation displacement time history the resulting forcing function can be extracted using a trapezoidal integration scheme. The general formula taken from any numerous numerical texts [Ref. 22] is presented as:

$$x(t) = \frac{1}{2} \Delta t (f_1 + 2f_2 + 2f_3 + 2f_4 \dots + f_n) \quad (54)$$

Applying the formulation to the convolution integral yields:

$$x(0) = \frac{1}{2} \Delta t (\dot{h}(0)f(0)) \quad (55)$$

$$x(\Delta t) = \frac{1}{2} \Delta t (h(0)f(0) + h(\Delta t)f(\Delta t)) \quad (56)$$

$$x(n\Delta t) = \frac{1}{2} \Delta t (h(0)f(0) + 2h(\Delta t)f(\Delta t) + \dots h(n\Delta t)f(n\Delta t)) \quad (57)$$

Rearranging Equations (55) through (57) into matrix form yields:

$$\begin{Bmatrix} x(0) \\ x(\Delta t) \\ x(2\Delta t) \\ \vdots \\ x(n\Delta t) \end{Bmatrix} = \frac{1}{2} \Delta t \begin{bmatrix} 0 & 0 & \cdots & 0 & 0 \\ h(\Delta t) & 0 & \cdots & 0 & 0 \\ h(2\Delta t) & h(\Delta t) & \cdots & 0 & 0 \\ \vdots & \vdots & \cdots & \cdots & 0 \\ h(n\Delta t) & h((n-1)\Delta t) & \cdots & h(\Delta t) & 0 \end{bmatrix} \begin{Bmatrix} f(0) \\ f(\Delta t) \\ f(2\Delta t) \\ \vdots \\ f(n\Delta t) \end{Bmatrix} \quad (58)$$

The impulse response function matrix is a lower triangular matrix that has zeros dominating the main diagonal. This in effect negates the weighting factor of the 1/2. The integration scheme then turns into a rectangular integration method with an $O(h)$ global error. To achieve the same $O(h^2)$ approximation of the trapezoidal scheme the weight is placed on $f(0)$. Rearranging the matrices in order to solve for $f(t)$ yields:

$$\begin{Bmatrix} x(\Delta t) \\ x(2\Delta t) \\ x(3\Delta t) \\ \vdots \\ x(n\Delta t) \end{Bmatrix} = \Delta t \begin{bmatrix} h(\Delta t) & 0 & \cdots & 0 \\ h(\Delta t) & h(\Delta t) & \cdots & 0 \\ h(\Delta t) & h(\Delta t) & \cdots & 0 \\ \vdots & \vdots & \cdots & \vdots \\ h(n\Delta t) & h((n-1)\Delta t) & \cdots & h(\Delta t) \end{bmatrix} \begin{Bmatrix} 2f(0) \\ f(\Delta t) \\ f(2\Delta t) \\ \vdots \\ f((n-1)\Delta t) \end{Bmatrix} \quad (59)$$

The solution for the extracted forcing function can be accomplished through various numerical methods. The trapezoidal integration scheme is a simple way of acquiring the synthesized forces given a non-isolated simple structure. Increasing the time step would increase accuracy, but can be computationally exhaustive for large time histories.

THIS PAGE INTENTIONALLY LEFT BLANK

V. RESULTS

To develop MATLAB code for the RBBIEF method workable and especially comparative models were used. A sinusoidal wave and the El Centro North South Earthquake of 1940 were used for the base excitation.

Appendix A presents the validation of the trapezoidal method versus NASTRAN and using MATLAB's *ode45* function. Using the same model the recursive block-by-block method is validated against *ode45* using a simple spring. The model is then run for an ideal bilinear element and compared to the results of the recursive block-by-block method

In order to demonstrate the advantages and disadvantages of the recursive block-by-block method 3 models were synthesized using the 1940 El Centro earthquake data. The first finite element model is a 4-story, single square bay, that is 25 feet wide and having an inter-story height of 17.5 feet. The structure is modeled using a total of 20 nodes, 120 DOF, four DOF in excitation, and four DOF in uplift. The second finite element model is a 4-story, nine square bays that is have a total width of 75 and having an inter-story height of 17.5 feet. The building is modeled using a total of 80 nodes, 480 DOF, with 16 DOF in excitation, and 16 DOF in uplift. The last model is the 30-story structure that is 225 feet by 225 feet at the base and an inter-story height of 17.5 feet for a total of 525 feet in height. The 30-story structure is modeled using 2,511 nodes, 15,066 degrees of freedom, 81 DOFs in excitation, and 81 DOFs in uplift. A summary is presented in Table 1.

	1-Bay 4-Story	9-Bay 4-Story	30-Story
Nodes	20	80	2511
Degrees of Freedom	120	480	15066
DOF in exictation	4	16	81
DOF in Uplift	4	16	81
Base Dimension	25' x 25'	75' x 75'	225' x 225'
Total Height	70'	70'	525'

Table 1. Parameters of Modeled Buildings

D. PROGRAM VALIDATION

1. De-coupled Versus Coupled System

A similar recursive process is validated in [Ref. 24] and is presented in Appendix B to validate the trapezoidal method. Using the trapezoidal method, a 9-DOF spring mass system, as shown in Figure 16, is used to present the validity of uncoupling a system. The equivalent de-coupled system is illustrated in Figure 17. Using a single block in the recursive block-by-block method with a linear spring of 10 lbf/in as the isolator the comparison is conducted. Both programs were run using a time step of .01 seconds for a ten second duration with a sinusoidal ground excitation of unit amplitude, oscillating at a frequency of .5 Hz.

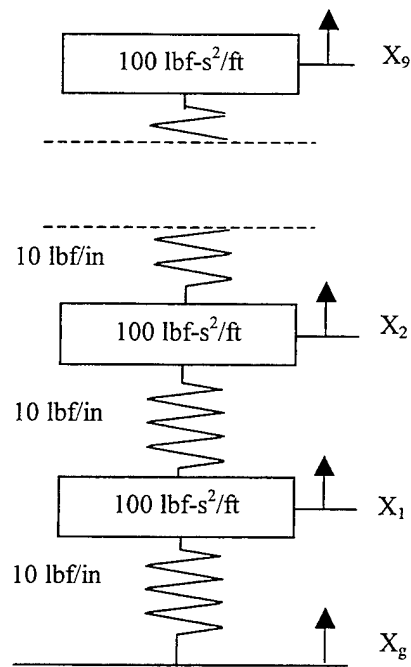


Figure 16. 9-DOF Spring Mass System

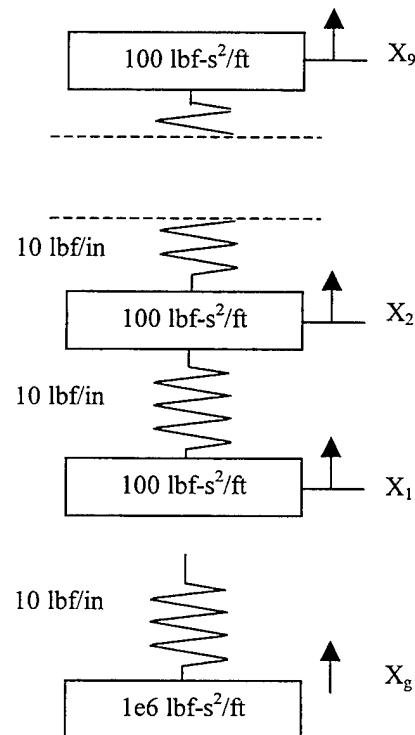


Figure 17. Uncoupled Large Mass 9-DOF Spring Mass System

Synthesizing a solution using single block in the recursive block-by-block program, Figure 18, represents the base displacement time history.

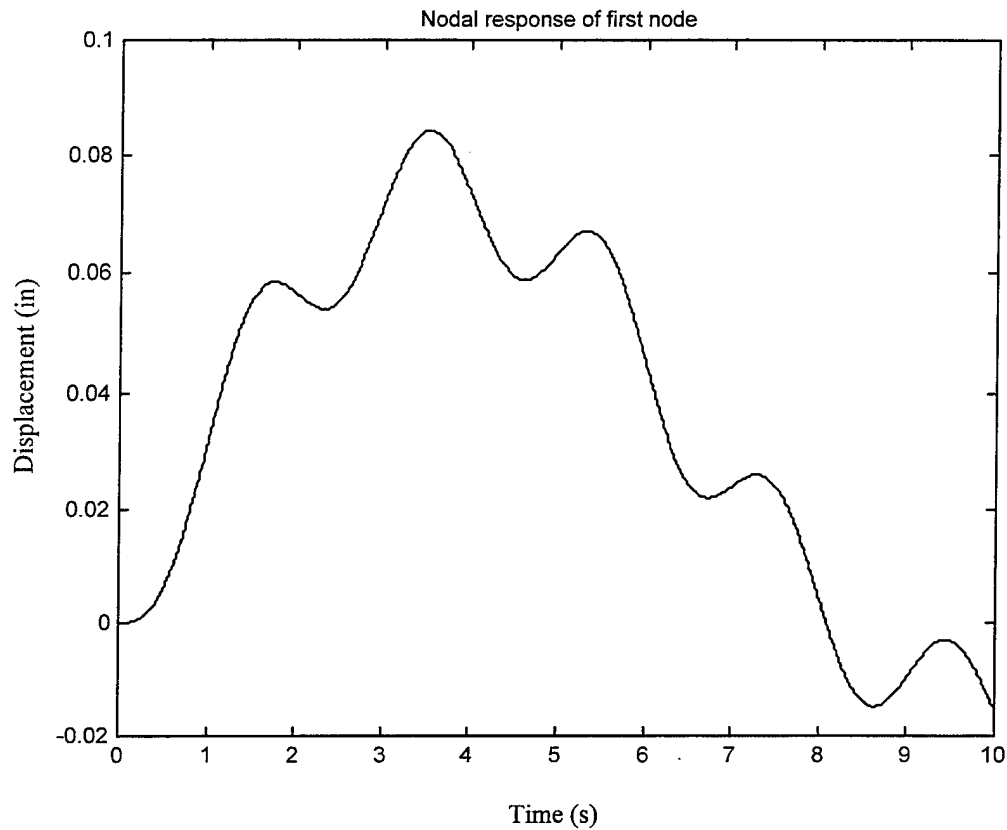


Figure 18. Base Displacement Time History of 9-DOF System Using Recursive Block-by-Block Synthesis

The trapezoidal results plotted along the curve presented in Figure 18, so absolute differences were calculated between the two data sets and revealed that the maximum difference is on the order of 10^{-8} .

2. Block-by-Block Synthesis Versus MATLAB's *ODE45*

The recursive block-by-block validation process will use the simple 9-DOF system is modeled in Figure 16. The process will begin with comparing the two methods using a simple linear spring. MATLAB's *ode45* function will use the state space representation of the second order differential equation presented by Equation (14). A comparison with an ideal bilinear isolator is then made. Because *ode45* is an adaptive algorithm, memory-type isolators with distinct discontinuities at transition points along the loop can make the adaptive solver computationally exhaustive. For example, the bilinear element has sharp transition points around which the *ode45* function will tend to oscillate. To avoid these oscillations, additional code was required to force the solution to stay within the hysteretic loop.

Using the same model in Figure 16, an arbitrary (nt) number of blocks were chosen producing the same plot as Figure 19. For clarification the number of block (nt) was set to three, the linear spring's value was 10 lbf/in, and the tolerance in the recursive block-by-block synthesis was set at 10^{-6} of displacement and 10^{-4} for velocity. Conducting the *ode45* equivalent and plotting the two graphs together depicted no appreciable difference. Therefore an absolute difference plot is again conducted in Figure 19.

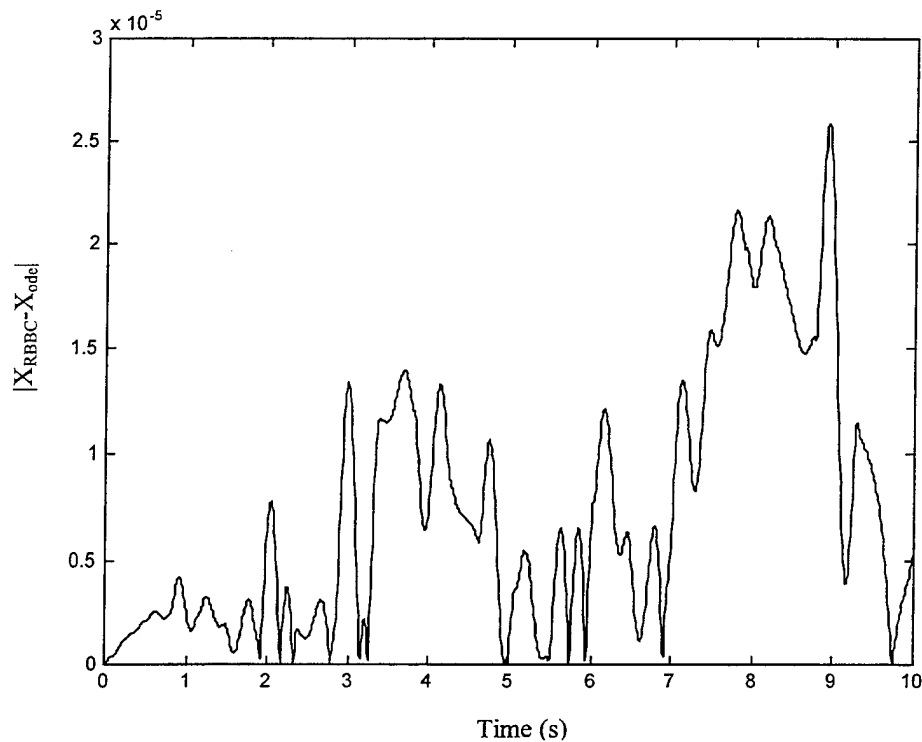


Figure 19. 9-DOF Spring Mass System, Absolute Base Displacement Differences
Between a Three Block Recursive Block-by-Block Synthesis and ODE45

Continuing the comparisons an ideal bilinear element was chosen next. The maximum tensile and compressive forces were set to 5 lbf and -5 lbf respectively. The initial spring constant, K_1 , was set to 10lbf with a yield to post ratio of .04. Again, the ground excitation was a unit sinusoidal waveform with a frequency of .5 Hz. Both programs were conducted with a time step of .01 seconds and a duration of 10 seconds. Figure 20, presents the two time displacement histories of the bottom node. The dashed line represents the ode45 solution. Figure 21, represents the two hysteretic loops. The circles represent the recursive *ode45* solution.

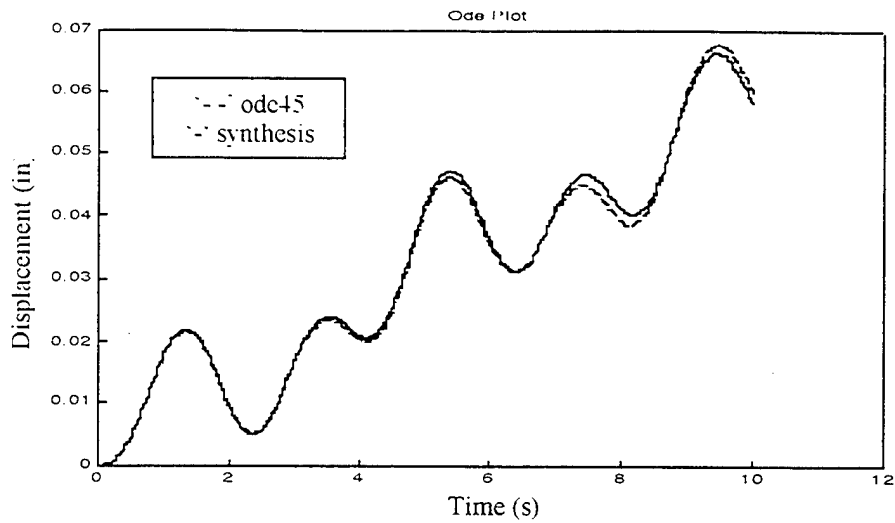


Figure 20. Three Block Synthesis Versus *ODE45* Base Displacements

Comparisons of a Linear Spring Isolated 9-DOF Spring Mass System, from a Unit Sinusoidal Ground Excitation at .5 Hz

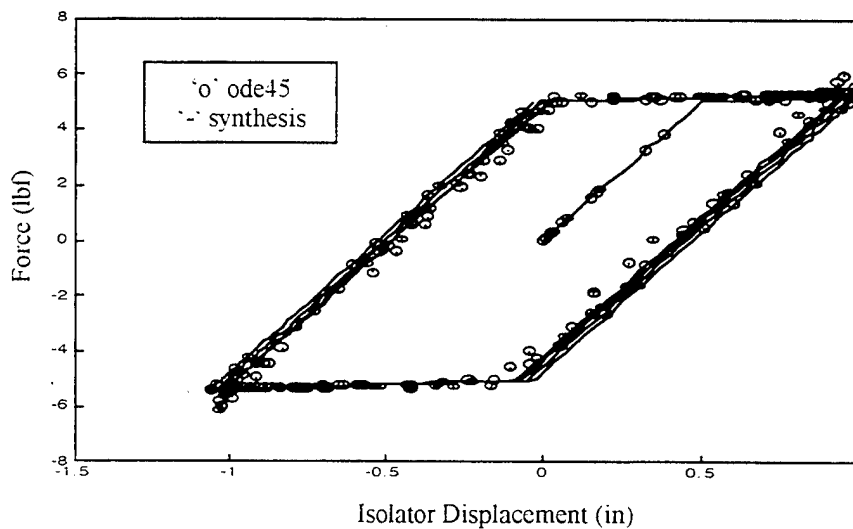


Figure 21. Three Block Synthesis Versus *ODE45* Hysteresis Comparisons of a Linear Spring Isolated 9-DOF Spring Mass System, From A Unit Sinusoidal Ground Excitation At .5 Hz

From Figure 21 it is shown how the ode45 function can oscillate about the discontinuous transition corners. Ultimately, Figure 20 indicates a very good approximation of the synthesis in comparison to the ode45 solution.

3. Model Isolator Plots

A sinusoidal wave of unit amplitude and a frequency of .5 Hz was used on the following modeled isolators below in Table 2.

	Properties
Real Bilinear Element	K = 500 lbf/in Yield to post ratio = .04 Max Tensile Force = 50 lbf Max Compressive Force = -50 lbf
Ideal Bilinear Element	K = 500 lbf/in Yield to post ratio = .04 Max Tensile Force = 50 lbf Max Compressive Force = -50 lbf
Wen Element	Fy = 100 lbf/in Max Elastic Displacement = 1 in A=8 n = 2 g = .0001 v=.0001 alpha=.04
Maxwell Element	K = 500 lbf/in C = 51 lbf-s/in

Table 2. Model Isolator Paramters of Sinusoidal Input

Figures 22 through 25 plot the respective hysteretic response loops. The duration of excitation was ten seconds and at a time step of .01 seconds. The values in Table 2 are arbitrary and were chosen to proved illustration in the figures.

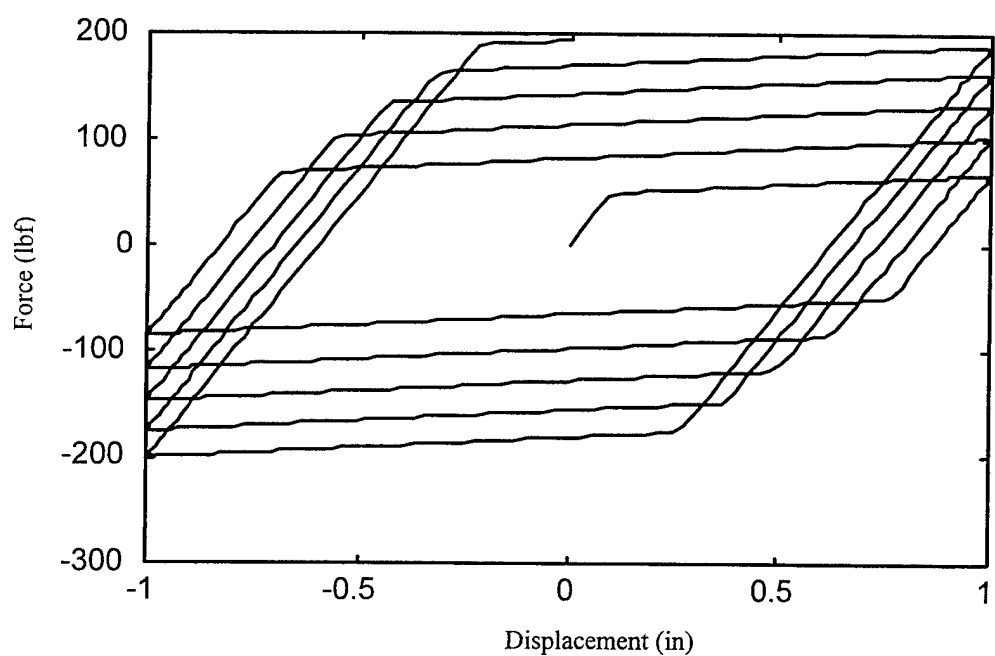


Figure 22. Unit Sinusoidal Ground Excitation at .5 Hz on a Real Bilinear Isolator

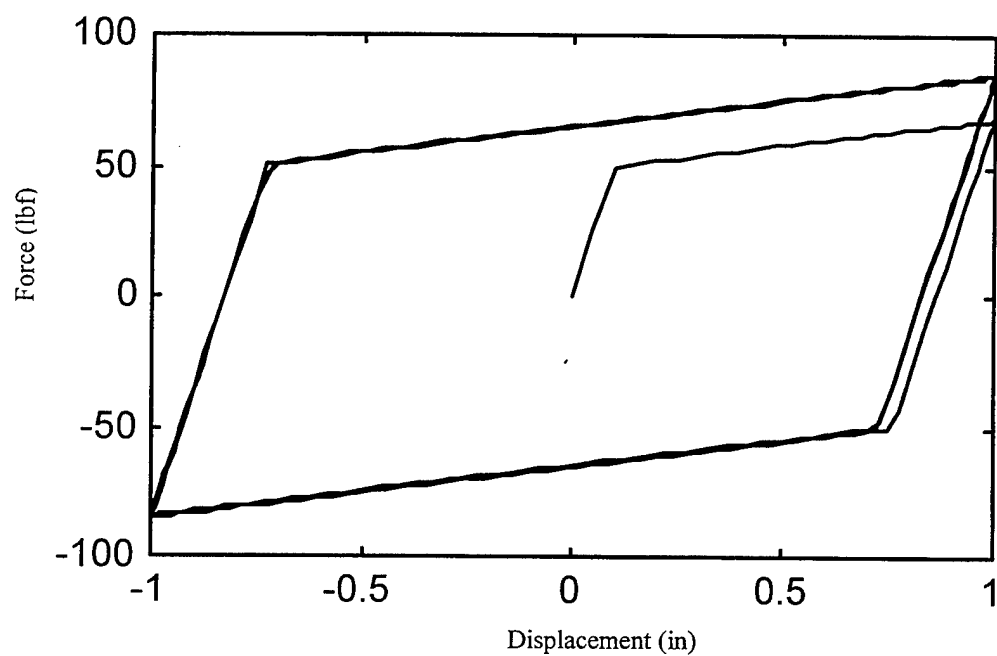


Figure 23. Unit Sinusoidal Ground Excitation at .5 Hz on an Ideal Bilinear Isolator

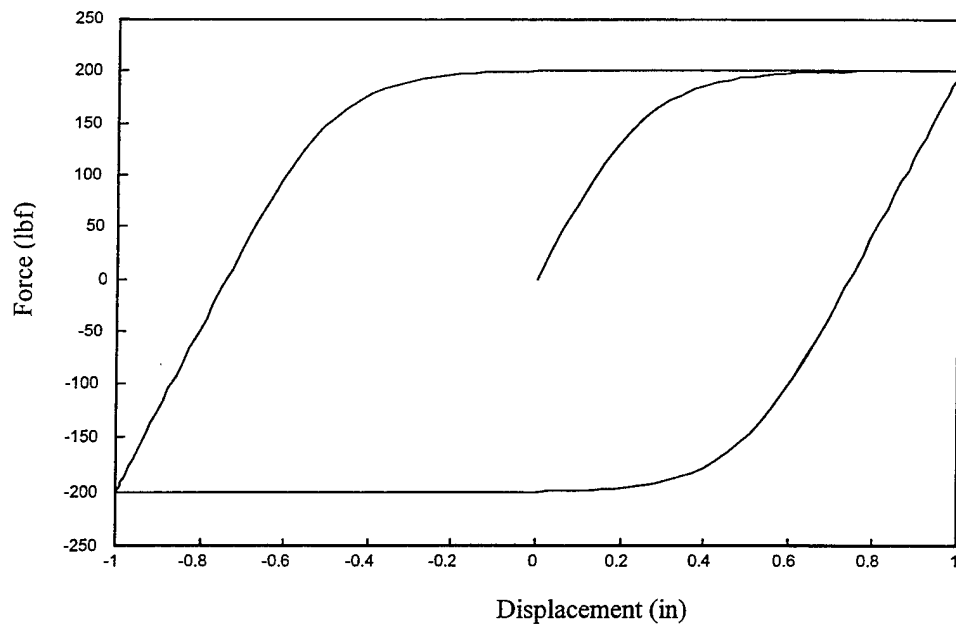


Figure 24. Unit Sinusoidal Ground Excitation at .5 Hz on a Wen Isolator

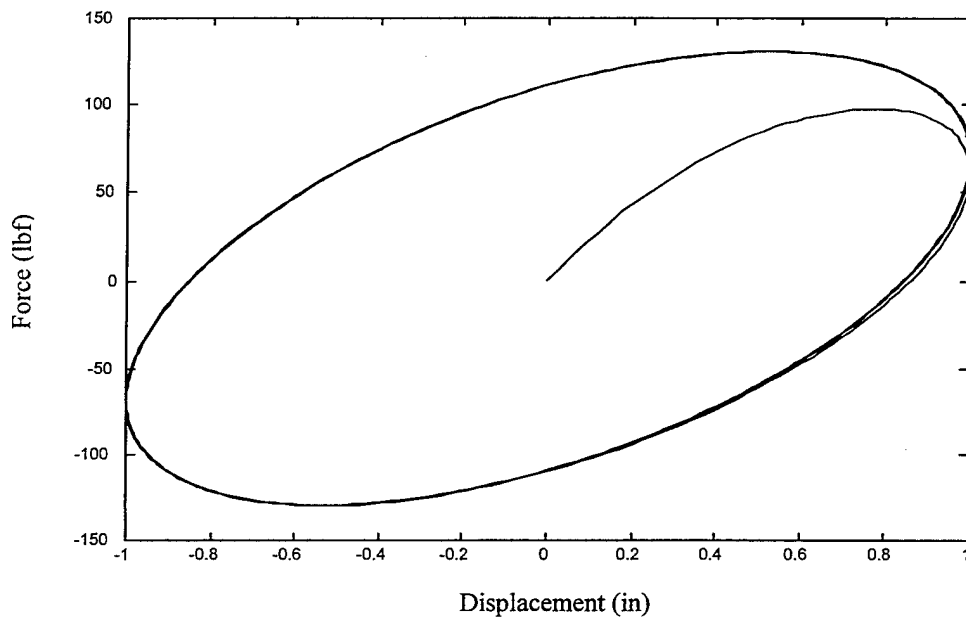


Figure 25. Unit Sinusoidal Ground Excitation at .5 Hz on a Maxwell Isolator

B. SINGLE BAY 4-STORY BUILDING

The 1940 El Centro Earthquake Data, Figure 26, displacement time history is used for the ground motion for synthesis. The earthquake data was sampled at .1 seconds for a duration of 50 seconds.

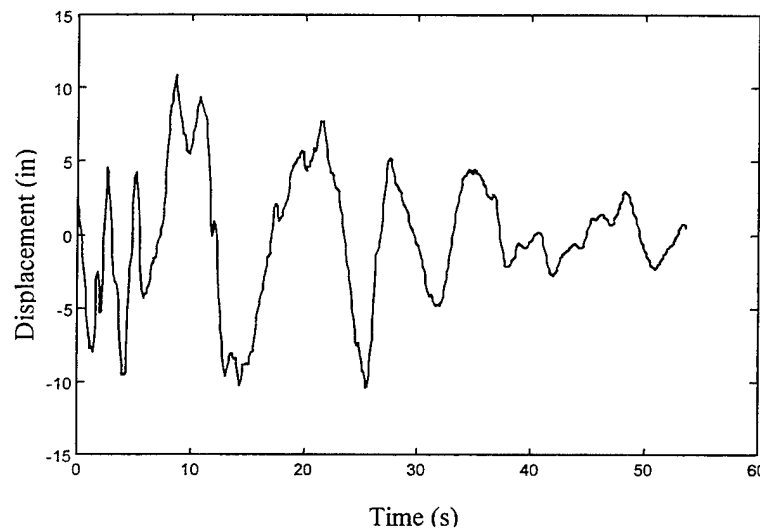


Figure 26. 1940 El Centro North South Ground Motion Time History

The uplift isolators were modeled as linear springs. The columns and beams are 50 ksi steel structural members with the following specifications: columns, W36x486; first and second floor beams, W36x170; third floor beams are W36x160; fourth floor beams, W36x150; roof beams, W36x135. A simple frame illustration of the building is shown in

Figure 27. The isolator's properties are listed in Table 3. Figure's 28-39 illustrates the hysteresis, horizontal and vertical displacement time responses to the earthquake input. The direction of excitation is along the weak axis of bending. Additionally, a cutoff frequency of 10 Hz was chosen leading to ten retained modes.

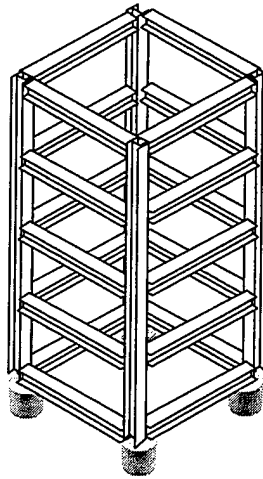


Figure 27. Single Bay, 4-Story Building Frame

	Properties
Real And Ideal Bilinear Elements	$K = 300 \text{ lbf/in}$ Yield to post ratio = .04 Max Tensile Force = 50 lbf Max Compressive Force = -50 lbf $K \text{ vertical} = 30 \text{ lbf/in}$ Stiffness Slope = 30 lbf/in-in
Wen Element	$F_y = 20 \text{ lbf/in}$ Max Elastic Displacement = 3 in $A = 3$ $n = 4$ $g = .0001$ $v = .000001$ $K \text{ vertical} = 30 \text{ lbf/in}$ $\alpha = .04$ $A, g, n, v, xy, F_y \text{ slope} = .08/\text{in} * (A, g, n, v, xy, F_y)$ $\alpha \text{ slope} = .008/\text{in} * \alpha$
Maxwell Element	$K = 300 \text{ lbf/in}$ $C = 51 \text{ lbf-s/in}$ $K \text{ vertical} = 30 \text{ lbf/in}$ Stiffness Slope = 30 lbf/in-in

Table 3. Single Bay, 4-Story Isolator Properties

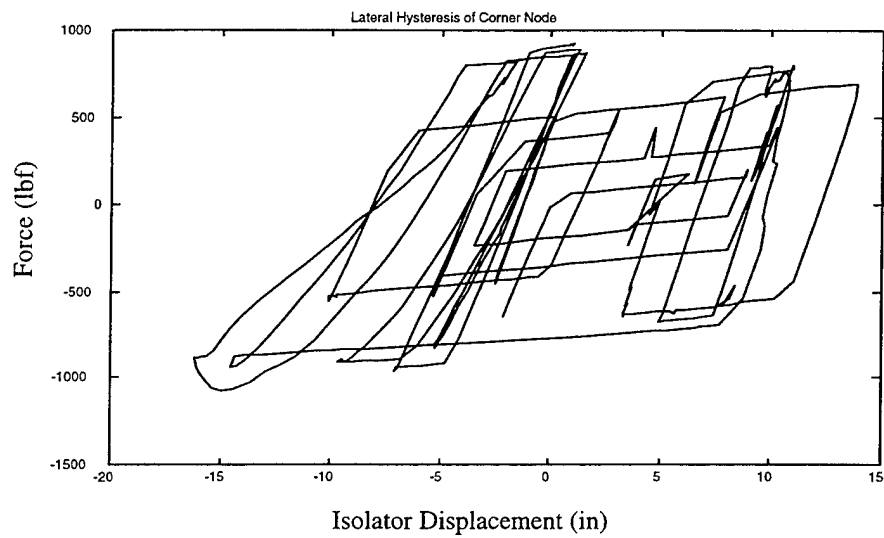


Figure 28. Single Bay, 4-Story, Real Bilinear Isolator, Corner Node Hysteresis for the 1940 El Centro North South Earthquake Ground Motion

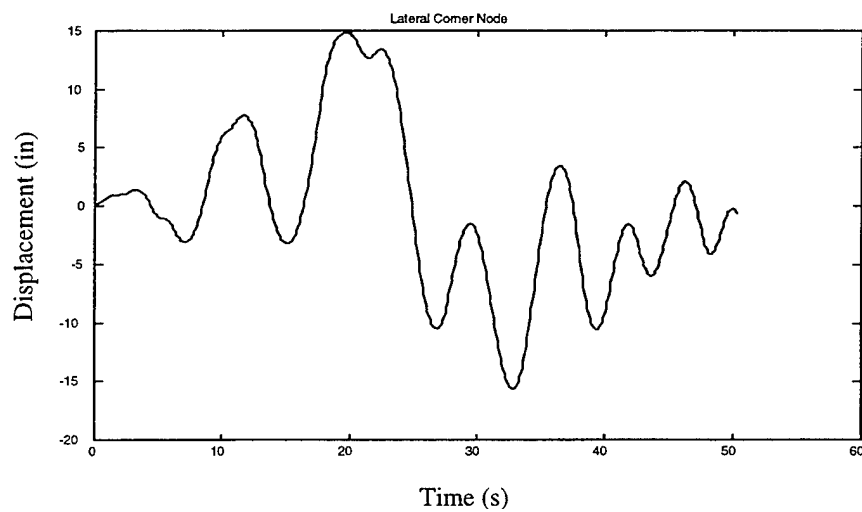


Figure 29. Single Bay, 4-Story, Real Bilinear Isolator, Corner Node Lateral Displacement History for the 1940 El Centro North South Earthquake Ground Motion

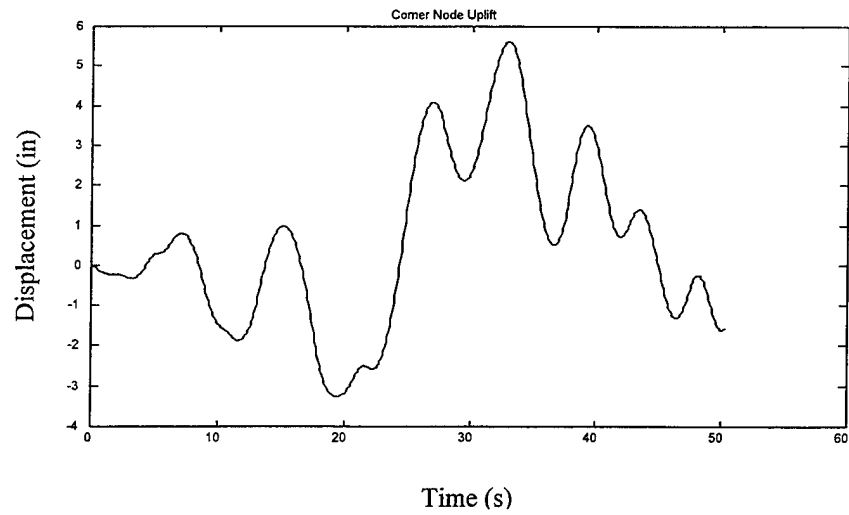


Figure 30. Single Bay, 4-Story, Real Bilinear Isolator, Corner Node Uplift Displacement History for the 1940 El Centro North South Earthquake Ground Motion

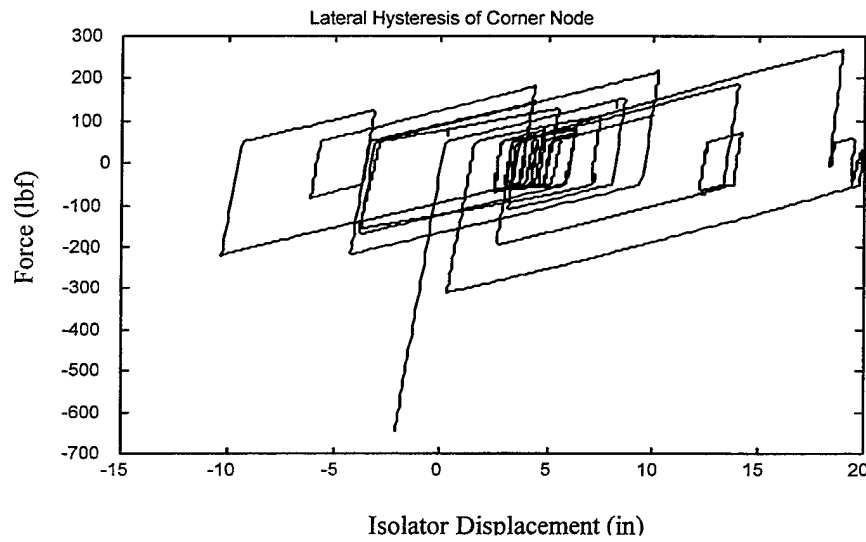


Figure 31. Single Bay, 4-Story, Ideal Bilinear Isolator, Corner Node Hysteresis for the 1940 El Centro North South Earthquake Ground Motion

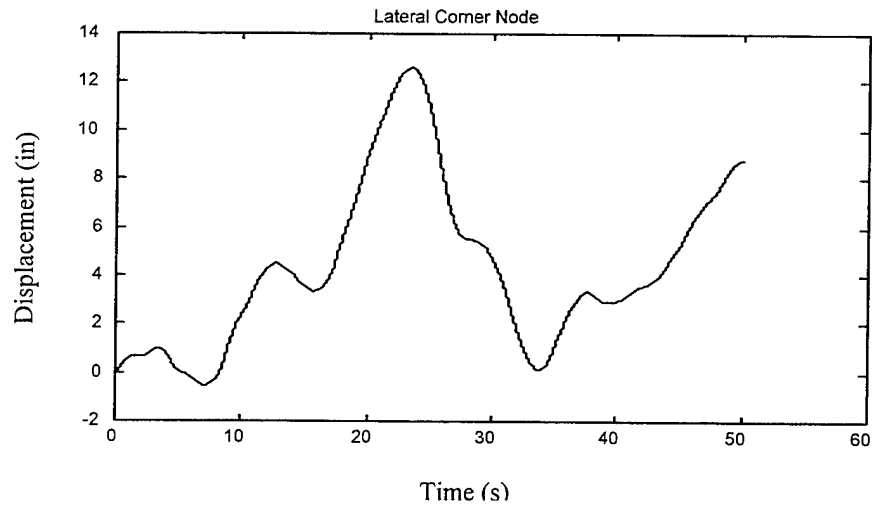


Figure 32. Single Bay, 4-Story, Ideal Bilinear Isolator, Corner Node Lateral Displacement History for the 1940 El Centro North South Earthquake Ground Motion

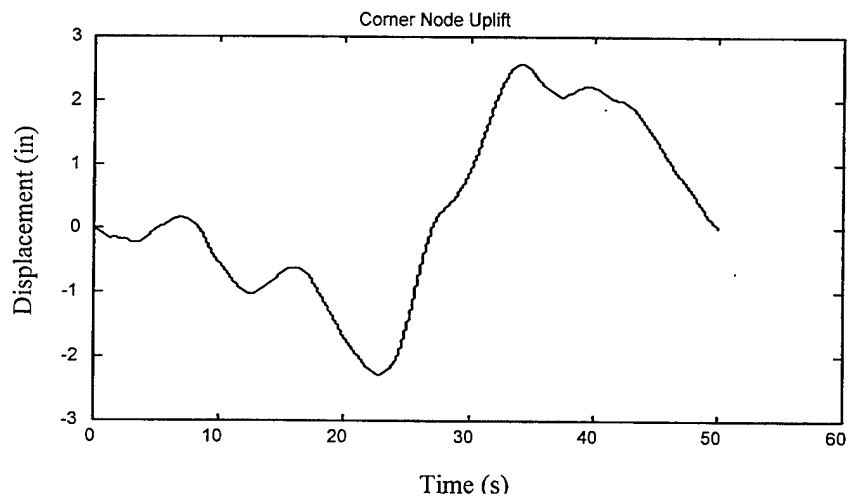


Figure 33. Single Bay, 4-Story, Ideal Bilinear Isolator, Corner Node Uplift Displacement History for the 1940 El Centro North South Earthquake Ground Motion

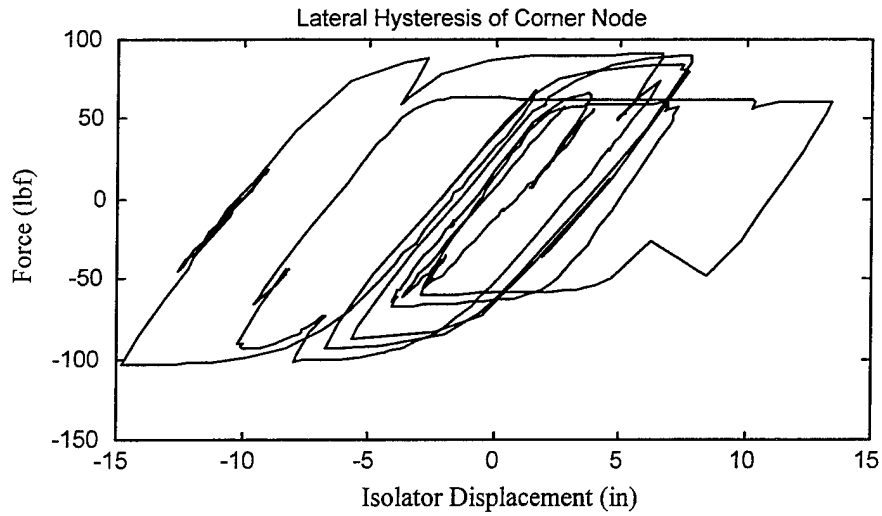


Figure 34. Single Bay, 4-Story, Wen Isolator, Corner Node Hysteresis for the 1940 El
Centro North South Earthquake Ground Motion

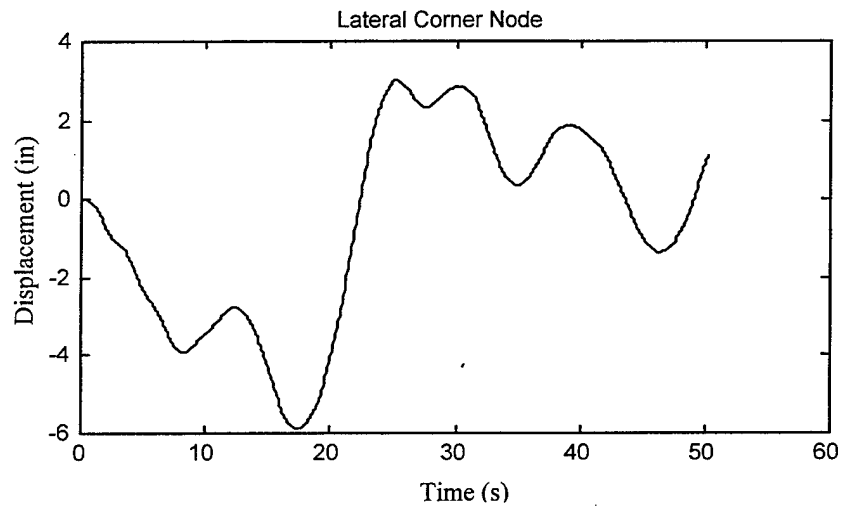


Figure 35. Single Bay, 4-Story, Wen Isolator, Corner Node Lateral Displacement History
for the 1940 El Centro North South Earthquake Ground Motion

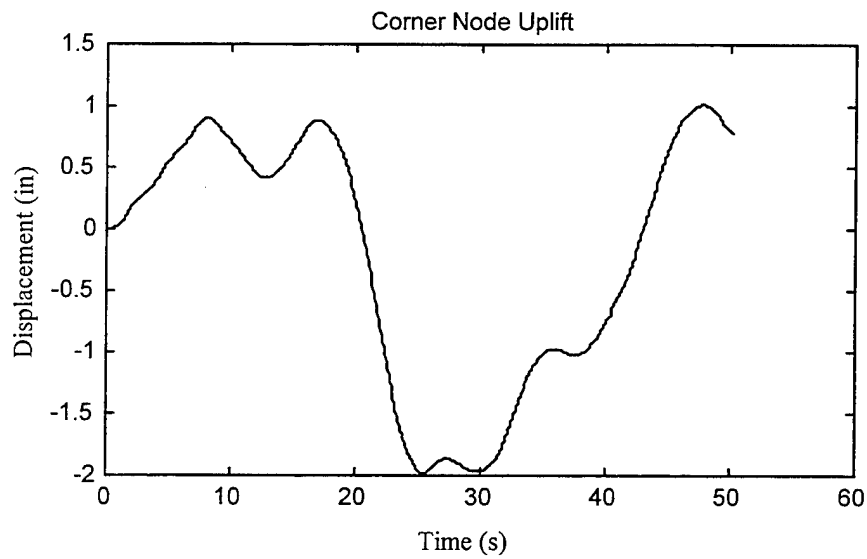


Figure 36. Single Bay, 4-Story, Wen Isolator, Corner Node Uplift Displacement History
for the 1940 El Centro North South Earthquake Ground Motion

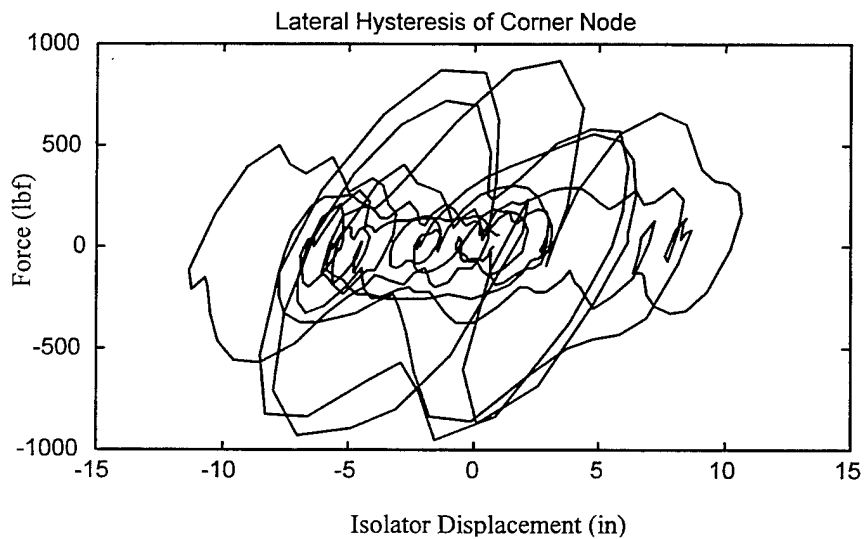


Figure 37. Single Bay, 4-Story, Maxwell Isolator, Corner Node Hysteresis for the 1940
El Centro North South Earthquake Ground Motion

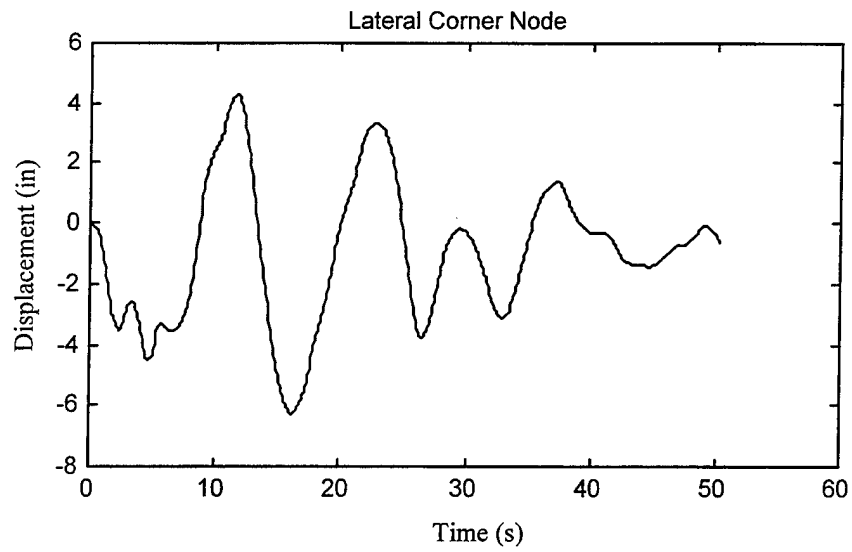


Figure 38. Single Bay, 4-Story, Maxwell Isolator, Corner Node Lateral Displacement History for the 1940 El Centro North South Earthquake Ground Motion

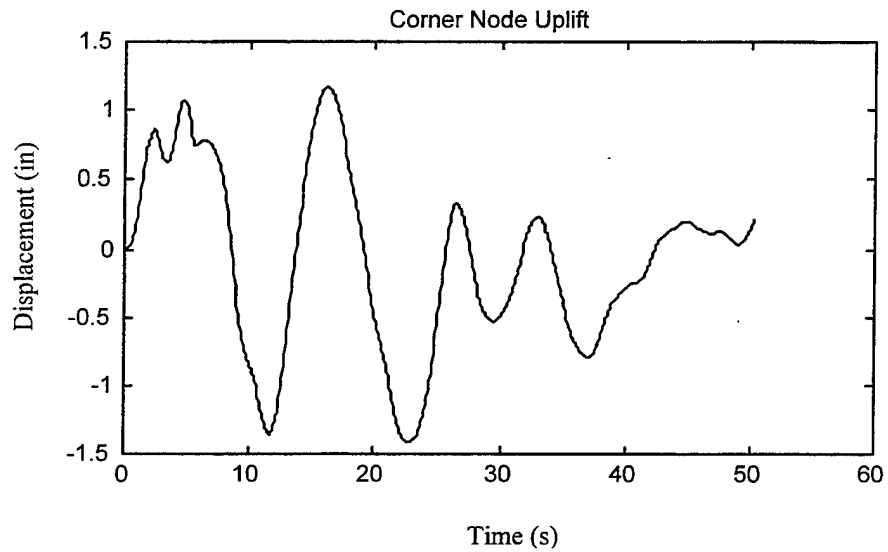


Figure 39. Single Bay, 4-Story, Maxwell Isolator, Corner Node Uplift Displacement History for the 1940 El Centro North South Earthquake Ground Motion

Table 4 and Table 5, present the computational results of the synthesis process using MATLAB 5.2.1 on a 733 Mhz Pentium III, Dell Computer.

Element	Blocks			
	4	8	16	24
Spring	8.3	6	6.4	8.8
Real Bilinear Element	7.6	5.4	6.6	8.6
Ideal Bilinear Element	5.5	4.3	6	8.5
Wen Element	5.1	4.6	6.1	9
Maxwell Element	8.2	6.4	7.25	10

Table 4. Single Bay, 4-Story, 1940 El Centro Earthquake Recursive Block-By-Block
Synthesis Time Results in Seconds

Element	Blocks			
	4	8	16	24
Spring	5.50E+08	9.30E+07	5.17E+07	4.22E+07
Real Bilinear Element	1.64E+08	7.11E+07	4.78E+07	3.90E+07
Ideal Bilinear Element	1.23E+08	6.00E+07	4.38E+07	3.90E+07
Wen Element	2.10E+08	8.89E+07	4.40E+07	3.77E+07
Maxwell Element	1.50E+08	7.04E+07	4.93E+07	4.14E+07

Table 5. Single Bay, 4-Story, 1940 El Centro Earthquake Block-By-Block Synthesis
FLOP Count Results

From the preceeding tables there is an indication that although the number of FLOPS decrease per block there is an optimum number of blocks. This is due to the number of optimum iterations per block. Upon converging to a number of iterations per block this number remains relatively the same for each block. Therefore, increasing the number of blocks with the same number of iterations increases the computation time.

C. 9-BAY, 4-STORY BUILDING

Increasing the model's complexity, a 9-bay 4-story building, Figure 40, is now investigated using the 16 hysteretic isolators that include uplift. Uplift is again calculated as in the single bay, 4-story structure.

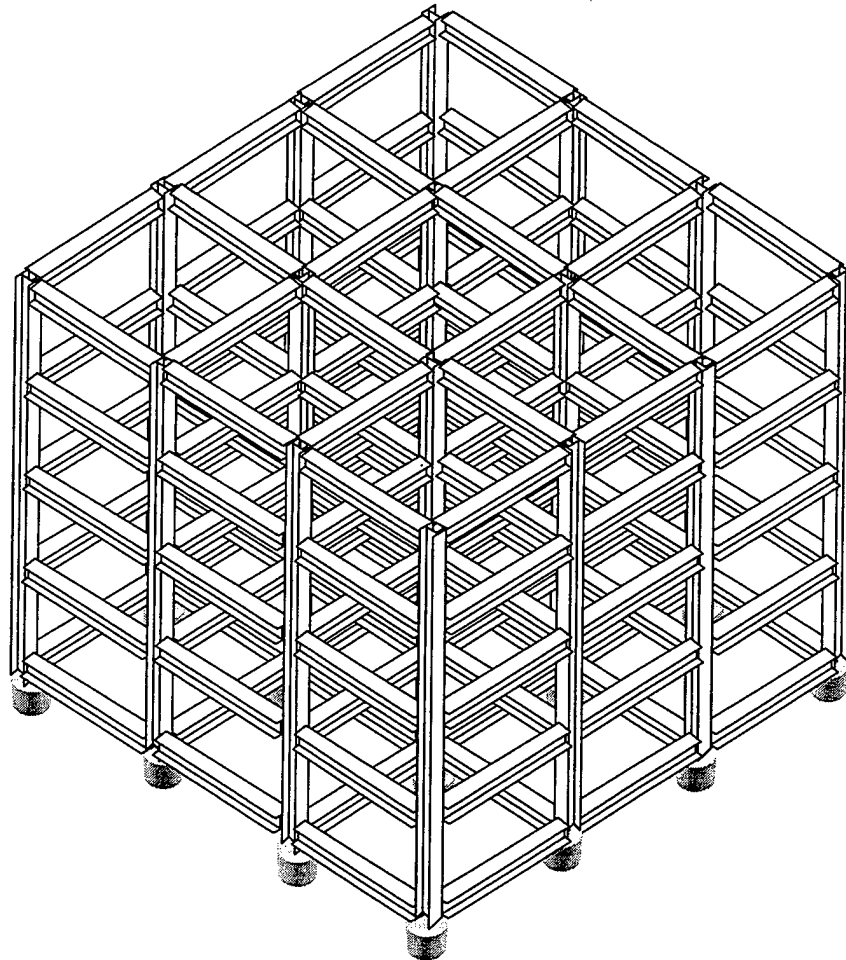


Figure 40. 9-Bay, 4-Story Building Frame

The building is design with 50 ksi steel members. The columns are W36x486, first and second floor beams are W36x170, third floor beams are W36x160, the fourth floor beams are W36x150, and the roof beams are W36x135.

The structure is synthesized for various isolators listed in Table 6, with a base excitation of the 1940 El Centro earthquake. The transient time history is developed from a time step of .1 seconds for a duration of 50 seconds.

	Properties
Real And Ideal Bilinear Elements	$K = 300 \text{ lbf/in}$ Yield to post ratio = .04 Max Tensile Force = 50 lbf Max Compressive Force = -50 lbf $K \text{ vertical} = 30 \text{ lbf/in}$ Stiffness Slope = 30 lbf/in-in
Wen Element	$F_y = 20 \text{ lbf/in}$ Max Elastic Displacement = 3 in $A = 3$ $n = 4$ $g = .00001$ $v = .000001$ $K \text{ vertical} = 30 \text{ lbf/in}$ $\alpha = .04$ $A, g, n, v, xy, F_y \text{ slope} = .08/\text{in} * (A, g, n, v, xy, F_y)$ $\alpha \text{ slope} = .008/\text{in} * \alpha$
Maxwell Element	$K = 300 \text{ lbf/in}$ $C = 51 \text{ lbf-s/in}$ $K \text{ vertical} = 30 \text{ lbf/in}$ Stiffness Slope = 30 lbf/in-in

Table 6. 9-Bay, 4-Story Isolator Properties

Figures 41-52, illustrate the results of displacement time histories and hysteretic loops of the respective isolators. Again, the cutoff frequency was set to 10 Hz retaining 20 modes. The direction of excitation is along the weak axis of bending.

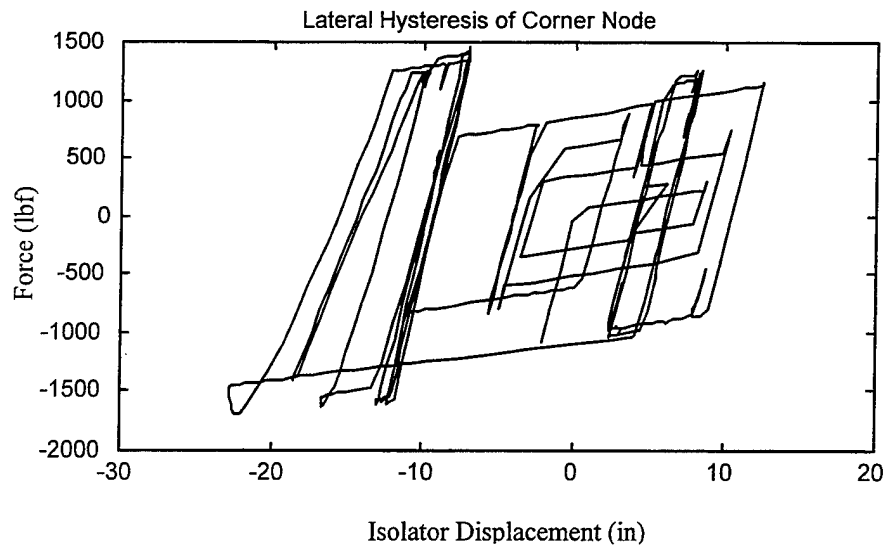


Figure 41. 9-Bay, 4-Story, Real Bilinear Isolator, Corner Node Hysteresis for the 1940 El

Centro North South Earthquake Ground Motion

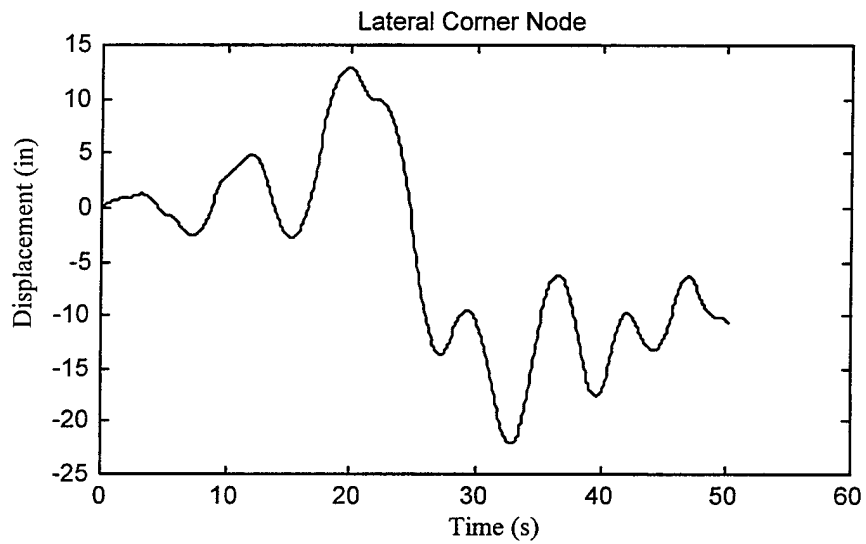


Figure 42. 9-Bay, 4-Story, Real Bilinear Isolator, Corner Node Lateral Displacement

History for the 1940 El Centro North South Earthquake Ground Motion

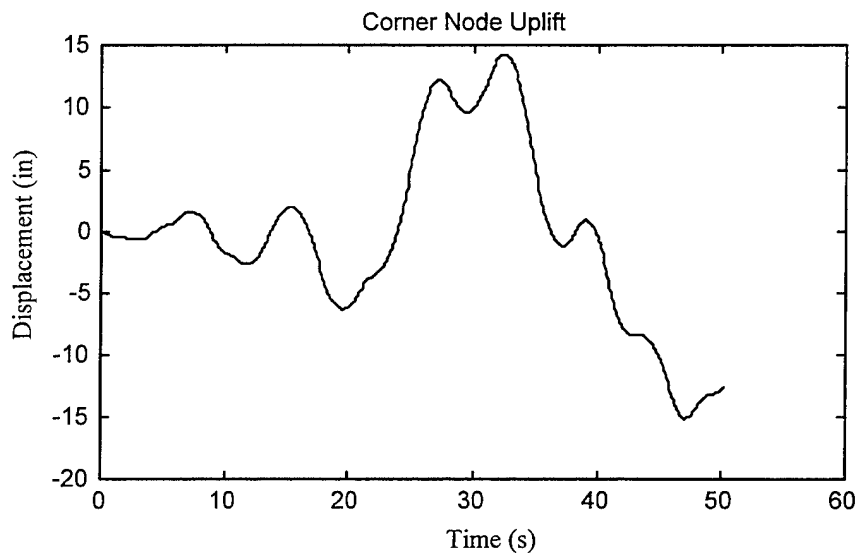


Figure 43. 9-Bay, 4-Story, Real Bilinear Isolator, Corner Node Uplift Displacement

History for the 1940 El Centro North South Earthquake Ground Motion

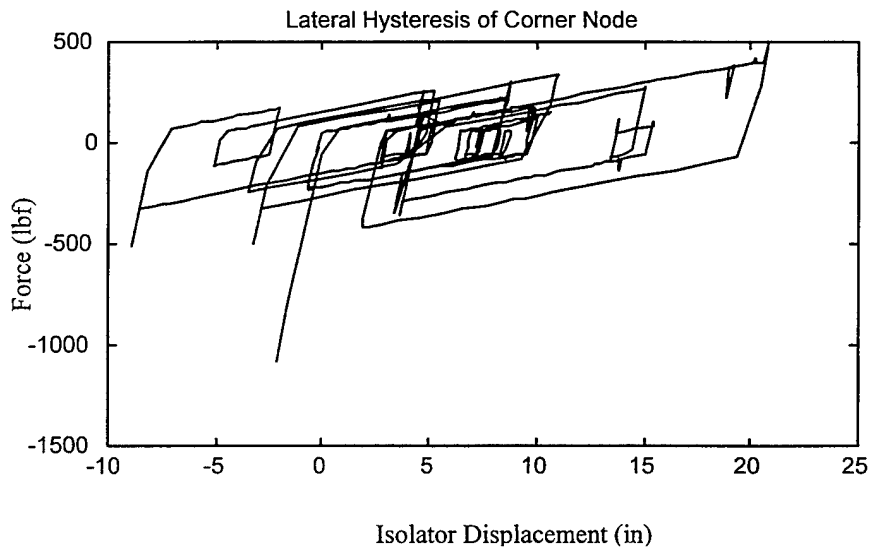


Figure 44. 9-Bay, 4-Story, Ideal Bilinear Isolator, Corner Node Hysteresis for the 1940

El Centro North South Earthquake Ground Motion

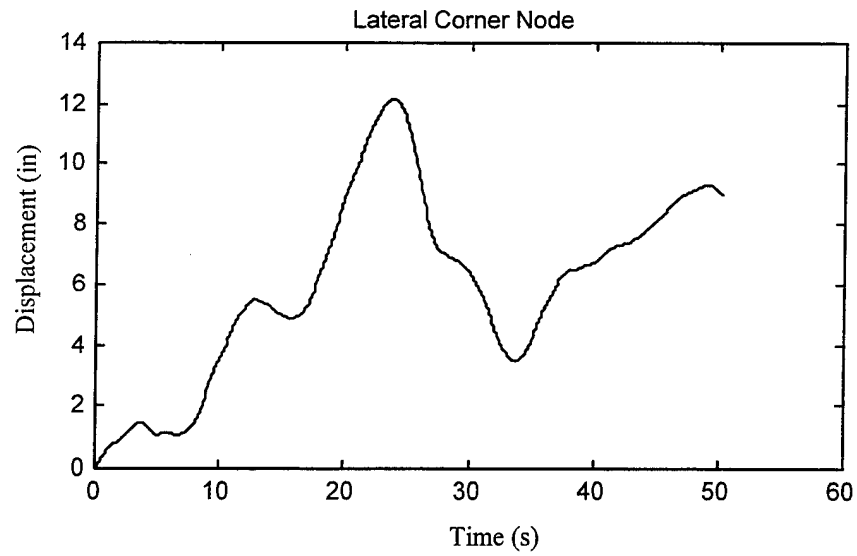


Figure 45. 9-Bay, 4-Story, Ideal Bilinear Isolator, Corner Node Lateral Displacement

History for the 1940 El Centro North South Earthquake Ground Motion

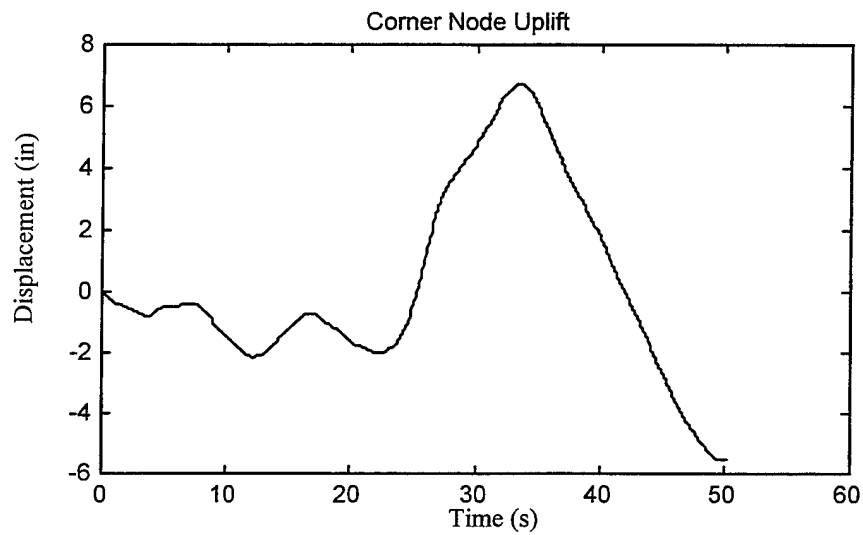


Figure 46. 9-Bay, 4-Story, Ideal Bilinear Isolator, Corner Node Uplift Displacement

History for the 1940 El Centro North South Earthquake Ground Motion

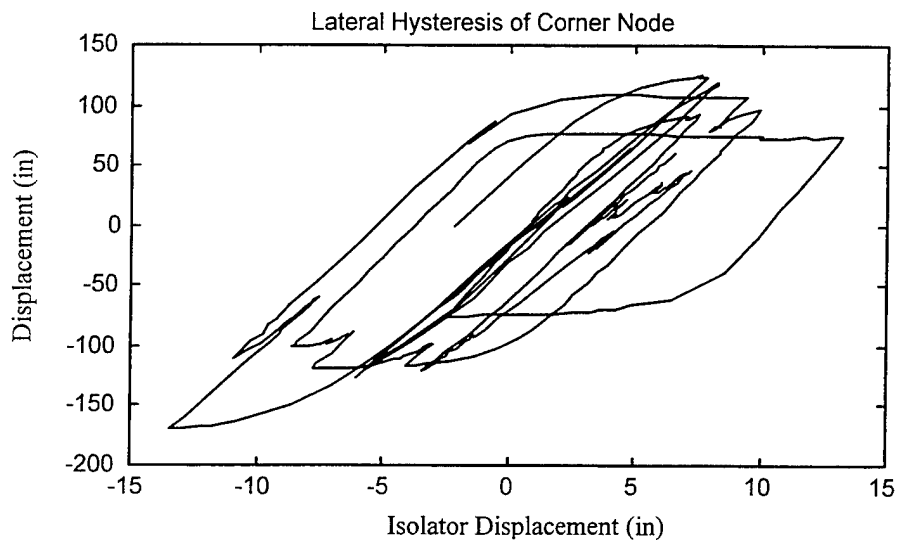


Figure 47. 9-Bay, 4-Story, Wen Isolator, Corner Node Hysteresis for the 1940 El Centro

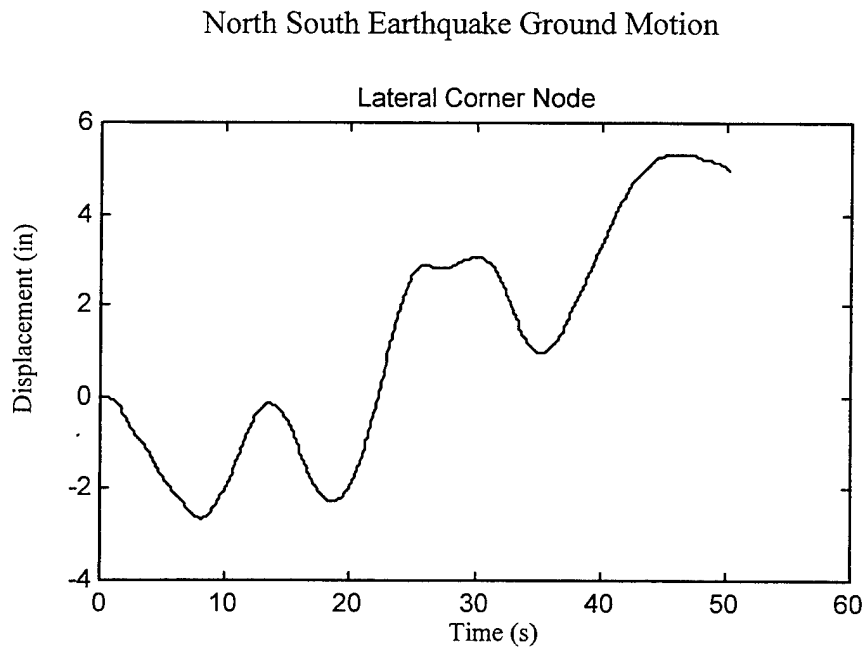


Figure 48. 9-Bay, 4-Story, Wen Isolator, Corner Node Lateral Displacement History for the 1940 El Centro North South Earthquake Ground Motion

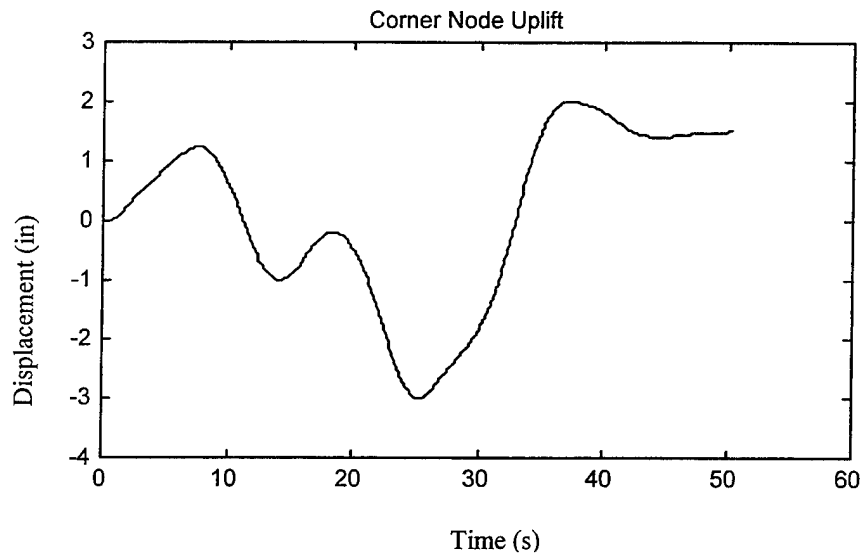


Figure 49. 9-Bay, 4-Story, Wen Isolator, Corner Node Uplift Displacement History for the 1940 El Centro North South Earthquake Ground Motion

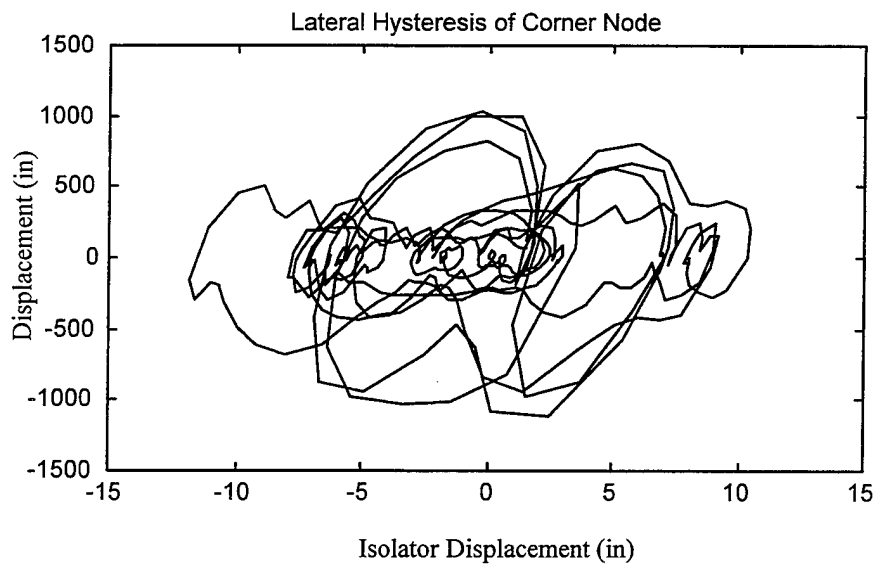


Figure 50. 9-Bay, 4-Story, Maxwell Isolator, Corner Node Hysteresis for the 1940 El Centro North South Earthquake Ground Motion

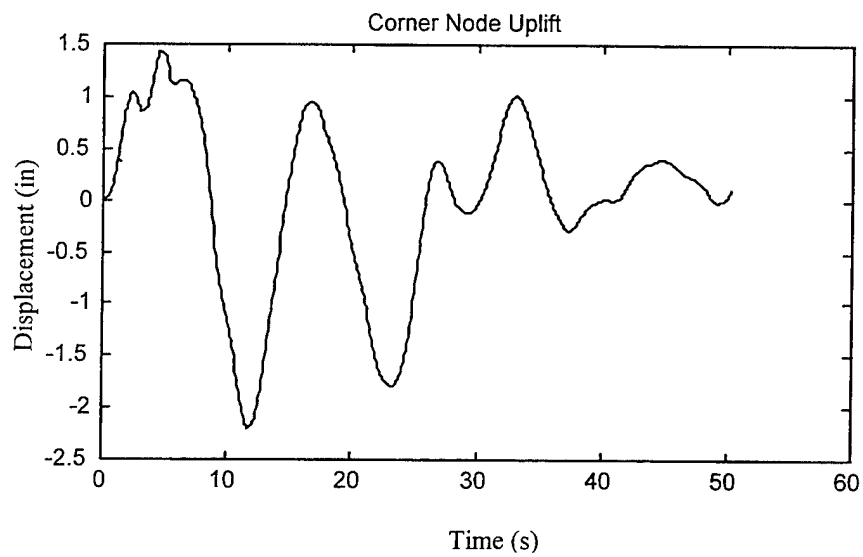


Figure 51. 9-Bay, 4-Story, Maxwell Isolator, Corner Node Lateral Displacement History
for the 1940 El Centro North South Earthquake Ground Motion

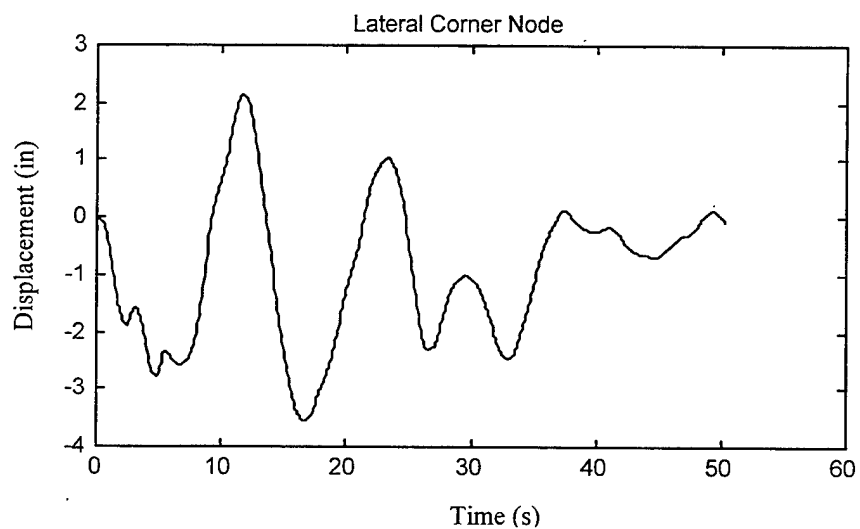


Figure 52. 9-Bay, 4-Story, Maxwell Isolator, Corner Node Uplift Displacement History
for the 1940 El Centro North South Earthquake Ground Motion

Again, Table 7 and Table 8, present the computational results of the synthesis process using MATLAB 5.2 on a 733 Mhz Pentium III, Dell Computer.

Element	Blocks			
	2	4	8	16
Spring	124	59	50	71
Real Bilinear Element	50	49	44	47
Ideal Bilinear Element	61	38	39	65
Wen Element	57	38	40	66
Maxwell Element	73	44	45	72

Table 7. 9-Bay, 4-Story, 1940 El Centro Earthquake Recursive Block-By-Block

Synthesis Time Results in seconds

Element	Blocks			
	2	4	8	16
Spring	9.27E+09	2.89E+09	7.37E+09	1.54E+09
Real Bilinear Element	3.17E+09	2.05E+09	7.01E+08	1.45E+09
Ideal Bilinear Element	4.06E+09	1.62E+09	6.74E+08	1.45E+09
Wen Element	2.70E+09	1.24E+09	6.39E+08	1.22E+09
Maxwell Element	5.10E+09	1.69E+09	6.93E+08	1.54E+09

Table 8. 9-Bay, 4-Story, 1940 El Centro Earthquake Block-By-Block Synthesis FLOP

Count Results

As before, there indicates an optimum number of blocks. In comparison to the single bay 4-story structure the optimum number of blocks were relatively the same although the number of FLOPS increased.

D. 30 STORY BUILDING

The 30-story building, Figure 53, is now investigated using 81 various hysteretic isolators that include uplift. Uplift calculations are carried from the previous examples. The structure is synthesized for various isolators listed in Table 9, with a base excitation of the 1940 El Centro earthquake.

	Properties
Real And Ideal Bilinear Elements	$K = 300 \text{ lbf/in}$ Yield to post ratio = .04 Max Tensile Force = 50 lbf Max Compressive Force = -50 lbf $K \text{ vertical} = 30 \text{ lbf/in}$ Stiffness Slope = 30 lbf/in-in
Wen Element	$F_y = 20 \text{ lbf/in}$ Max Elastic Displacement = 3 in $A = 3$ $n = 4$ $g = .00001$ $v = .000001$ $K \text{ vertical} = 30 \text{ lbf/in}$ $\alpha = .04$ $A, g, n, v, xy, F_y \text{ slope} =$ $.08/\text{in} * (A, g, n, v, xy, F_y)$ $\alpha \text{ slope} = .008/\text{in} * \alpha$
Maxwell Element	$K = 300 \text{ lbf/in}$ $C = 51 \text{ lbf-s/in}$ $K \text{ vertical} = 30 \text{ lbf/in}$ Stiffness Slope = 30 lbf/in-in

Table 9. 30-Story Isolator Properties

The transient time history is developed from a time step of .1 seconds for a duration of 50 seconds. Again, excitation is in weak axis of bending and Figures 54-65 represents the results of the displacement time histories and hysteresis.

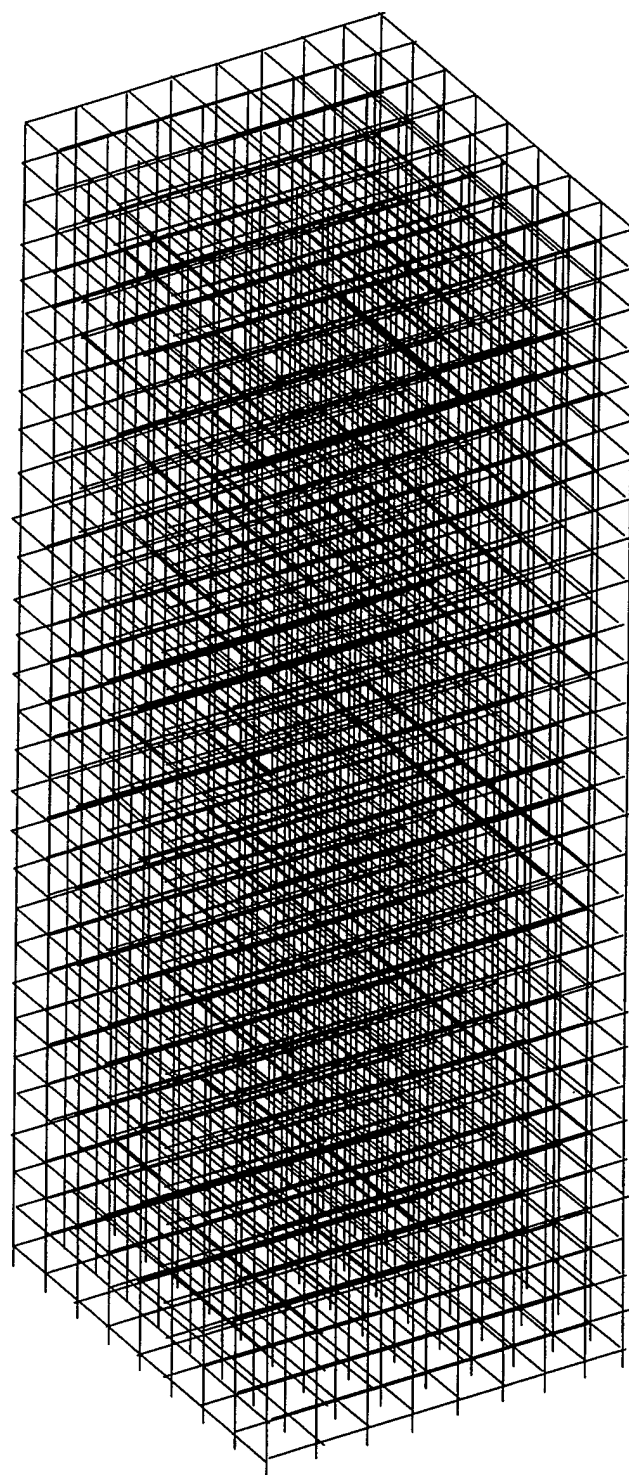


Figure 53. 30-Story Building Wire Frame

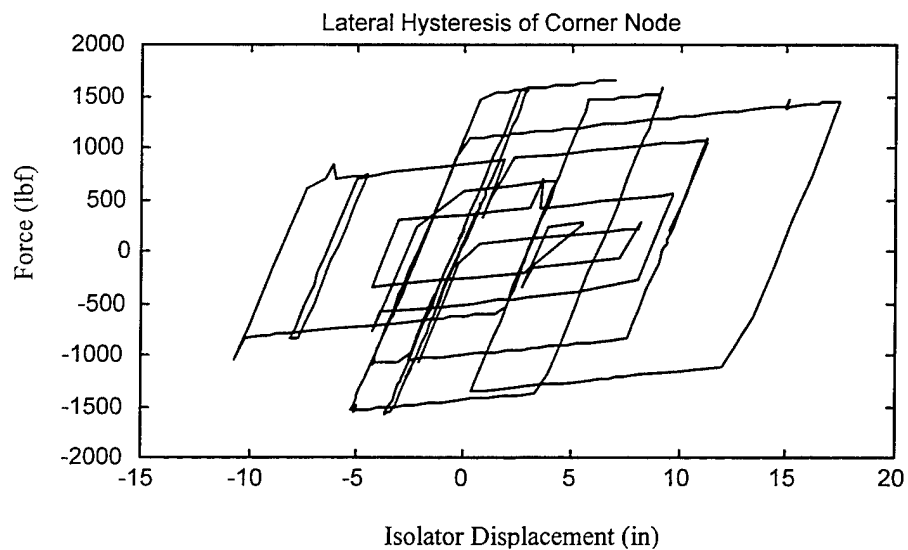


Figure 54. 30-Story, Real Bilinear Isolator, Corner Node Hysteresis for the 1940 El

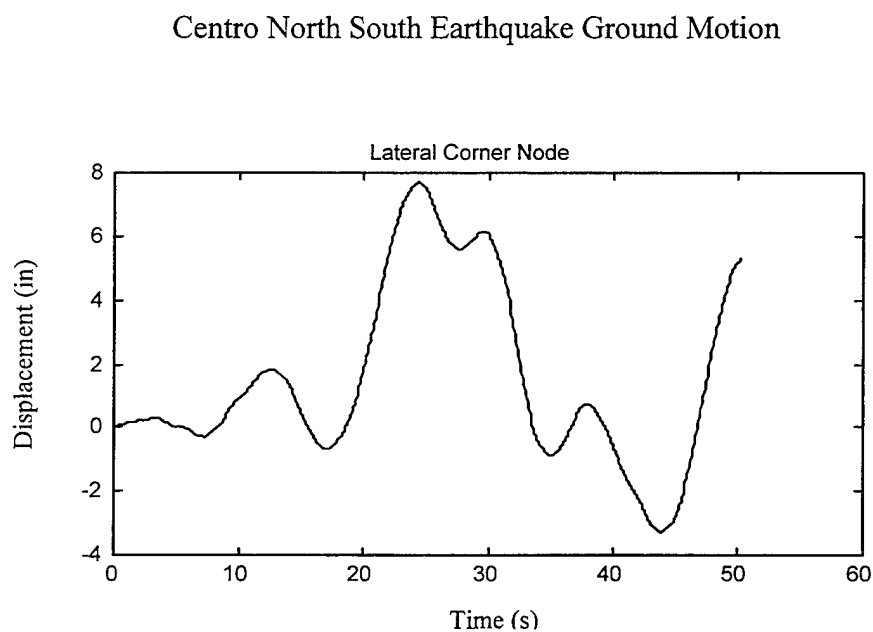


Figure 55. 30-Story, Real Bilinear Isolator, Corner Node Lateral Displacement History
for the 1940 El Centro North South Earthquake Ground Motion

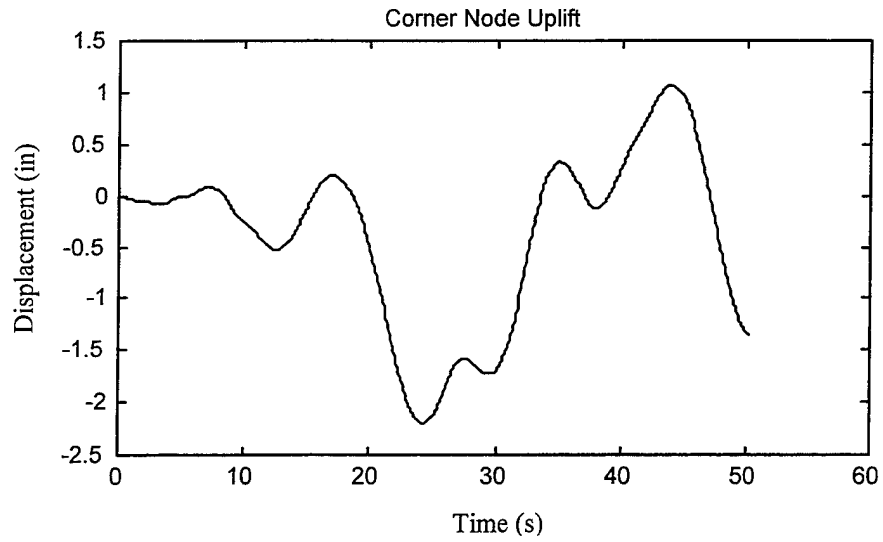


Figure 56. 30-Story, Real Bilinear Isolator, Corner Node Uplift Displacement History for the 1940 El Centro North South Earthquake Ground Motion

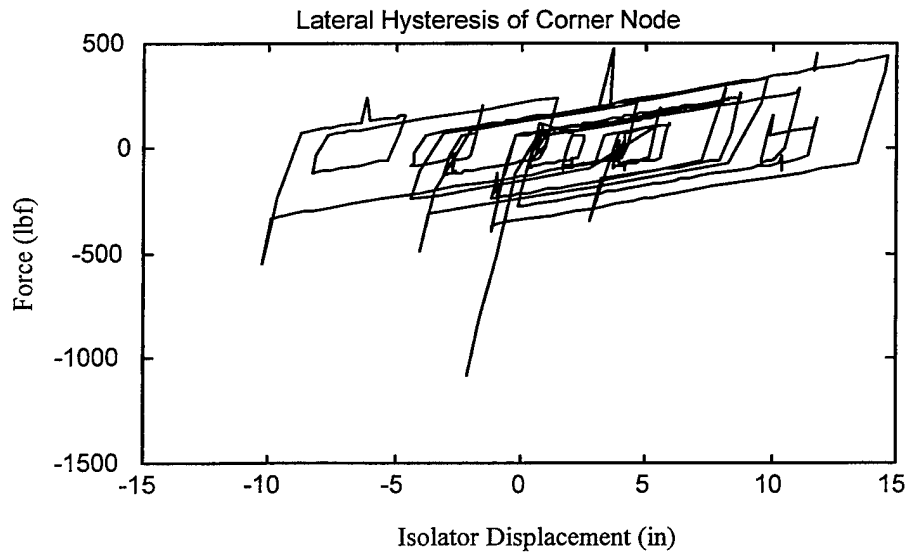


Figure 57. 30-Story, Ideal Bilinear Isolator, Corner Node Hysteresis for the 1940 El Centro North South Earthquake Ground Motion

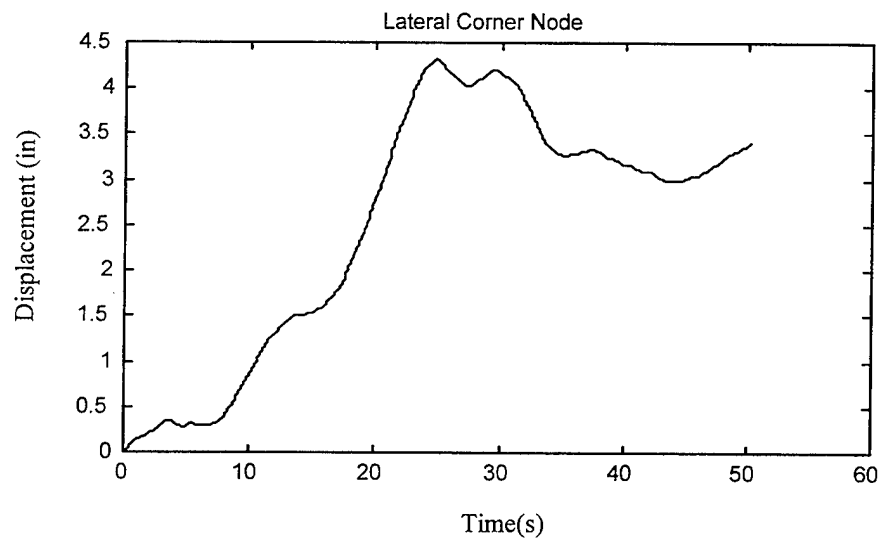


Figure 58. 30-Story, Ideal Bilinear Isolator, Corner Node Lateral Displacement History
for the 1940 El Centro North South Earthquake Ground Motion

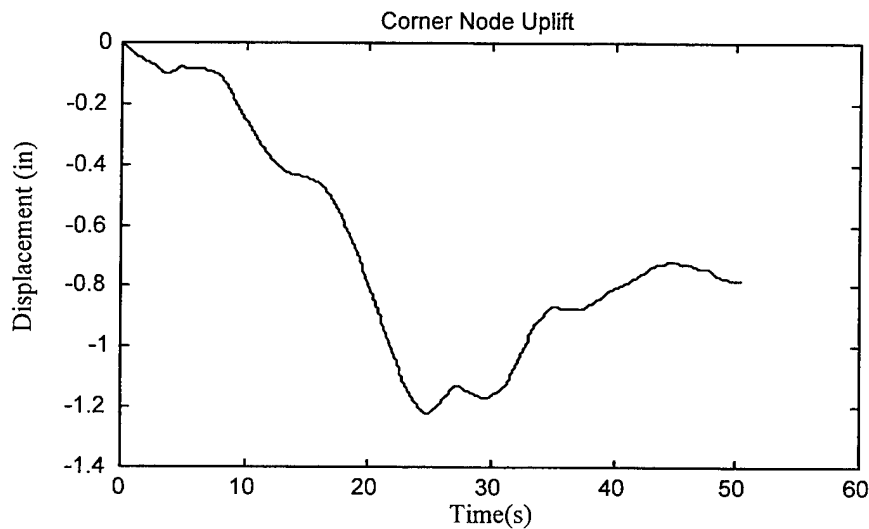


Figure 59. 30-Story, Ideal Bilinear Isolator, Corner Node Uplift Displacement History
for the 1940 El Centro North South Earthquake Ground Motion

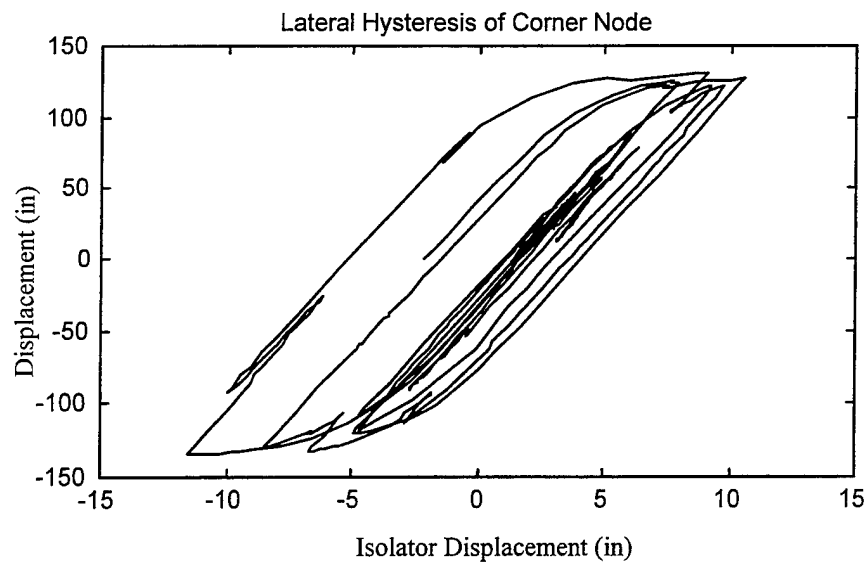


Figure 60, 30-Story, Wen Isolator, Corner Node Hysteresis for the 1940 El Centro North

South Earthquake Ground Motion

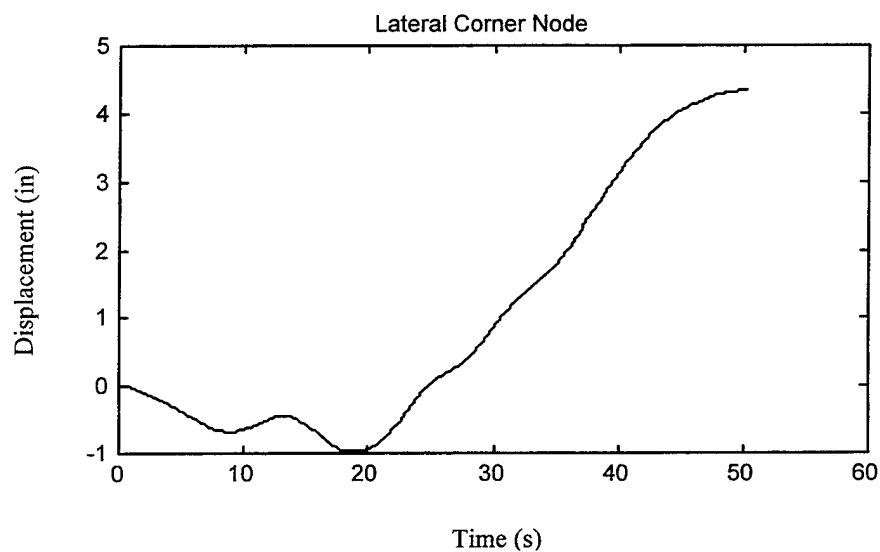


Figure 61. 30-Story, Wen Isolator, Corner Node Lateral Displacement History for the
1940 El Centro North South Earthquake Ground Motion

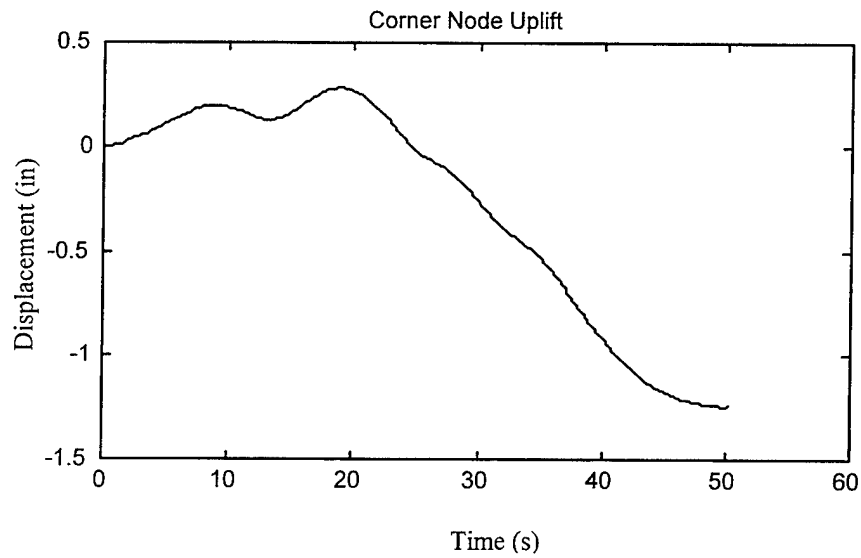


Figure 62. 30-Story, Wen Isolator, Corner Node Uplift Displacement History for the 1940 El Centro North South Ground Motion

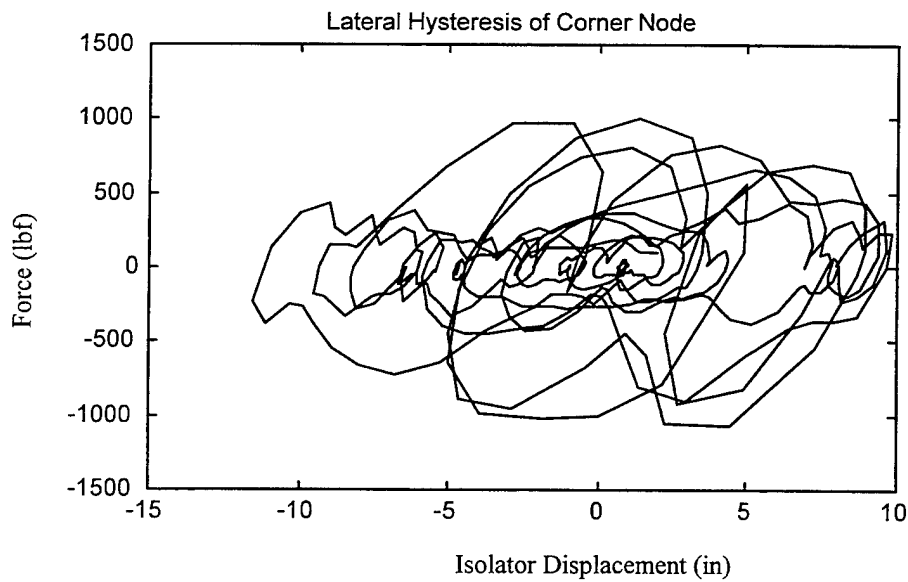


Figure 63, 30-Story, Maxwell Isolator, Corner Node Hysteresis for the 1940 El Centro North South Earthquake Ground Motion

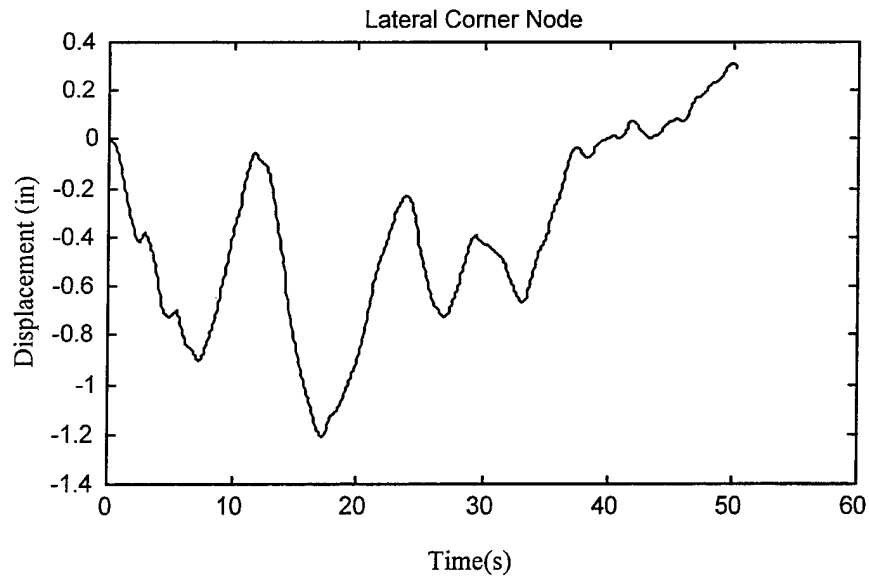


Figure 64. 30-Story, Maxwell Isolator, Corner Node Lateral Displacement History for the 1940 El Centro North South Earthquake Ground Motion

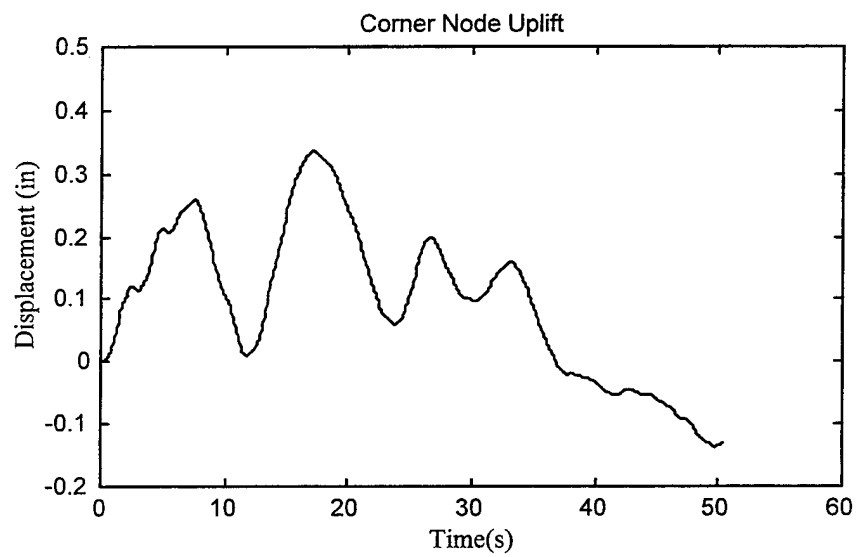


Figure 65. 30-Story, Maxwell Isolator, Corner Node Uplift Displacement History for the 1940 El Centro North South Earthquake Ground Motion

Again, Table 10 and Table 11, present the computational results of the synthesis process using MATLAB 5.2 on a 733 Pentium III, Dell Computer.

Element	Blocks			
	2	4	6	8
Spring	1388	823	783	870
Real Bilinear Element	840	611	615	782.7
Ideal Bilinear Element	847	402	489	625
Wen Element	819	576	785	989
Maxwell Element	603	485	576	680

Table 10. 30-Story, 1940 El Centro Earthquake Recursive Block-By-Block Synthesis

Time Results in seconds

Element	Blocks			
	2	4	6	8
Spring	1.21E+11	4.50E+10	2.91E+10	2.34E+10
Real Bilinear Element	6.80E+10	3.23E+10	2.27E+10	2.06E+10
Ideal Bilinear Element	3.15E+10	1.97E+10	1.74E+10	1.60E+10
Wen Element	9.13E+10	4.50E+10	2.90E+10	2.33E+10
Maxwell Element	3.82E+10	2.56E+10	2.11E+10	1.82E+10

Table 11. 30-Story, 1940 El Centro Earthquake Block-By-Block Synthesis Flop Count

Results

For the above calculations, the cutoff frequency was set to 1.0 Hz, which retained a total of 26 modes.

Looking at the optimum number of blocks versus time, Table 12, tabulates the fastest times for the varying numbers of isolators and DOFs. The table also compares time synthesis for various computers and processor speeds. The synthesized values are

taken from a 50 second time duration of the 1940 El Centro earthquake displacement data for the nonlinear Wen element.

	1-Bay 4-Story	9-Bay 4-Story	15-Bay 30-Story
NDOF synthesized	8	32	162
Modes retained	20	20	26
NDOF	120	480	15066
Optimum Number of Blocks	8	5	4
Avg Iterations	10	8	8
PowerMac G4 350 Mhz Time (s)	15	60	1145
Dell Pentium III 750 MHz Time (s)	4.6	38	576

Table 12. Optimum Times for Nonlinear Wen Element Synthesis

As Table 12 indicates that for fairly large base isolated structures the optimum number of blocks doesn't deviate much from smaller models. Although relatively constant the timesavings can be significant from the original integral method.

VI. CONCLUSIONS

The recursive block-by-block method is considerably efficient in computing the seismic transient dynamic response of multiple degrees of freedom structures using hysteretic type isolators. As Table 12 outlines, there are limits to the number of blocks used to save computation time. Though the number of iterations is generally reduced per block, the recursive iterative process still requires a minimum amount of iterations to converge. Therefore, by increasing the number of blocks will incur added synthesis time even though the number of floating point operations, FLOPS, is decreased.

Although the initial reductions in time computation are attributed to the retention of significant modes and computing the synthesis over the retained (Cset) degrees of freedom, it is the recursive block-by-block method that can further reduce it up to an additional 60%. For large (Cset) models the major computational elements are the impulse response matrix assembly and the recursive iterative synthesis. As stated above the iterative synthesis will reach a minimum, however, the impulse response function program can contain a significant amount of loops which can have a moderate effect on time. However, if the time duration and the number of modes retained remain constant a flag variable can be entered as to skip this computation if the only thing that changes is isolator properties. This can significantly reduce the computation time for large number of isolator based structures.

Since the program only iterates on the retained (Cset) nodal degree of freedoms, it will produce the transient dynamic response history and the respective synthesized force time history. Because of this, if two structures had an equal number of base

isolators and the same number of modes retained, the program's run time will be similar even though structure two had 10 times as many nodes as structure one did. To compute non-isolator coupled degrees of freedom time history responses the integral equation formulation of the synthesized forces and the associate impulse response function is employed. This integral calculation can be computed directly or by the block-by-block method. Either method produces the responses quickly and in a matter of seconds.

The force extraction of an isolated structure using the trapezoidal integration scheme proved very accurate. However, the limitations lay in MATLAB's memory intensive backslash command, '\', and the process only works on system that has only one node in vibration.

VII. RECOMMENDATIONS FOR FUTURE WORK

The work contained herein was conducted to develop and validate a recursive block-by-block program that uses nonlinear hysteretic type isolators for base isolation. There have been studies conducted on the exact nature of uplift effects on isolators. The shared data from these studies or additional laboratory data can be incorporated into the program as data files, which MATLAB can easily interpolate from. Using this data, a model can be designed and isolated using a known or fabricated isolator. This model can then be used for further validation of the program. Additionally, optimizing the program code can greatly reduce the computation time by re-writing the loops into a more efficient manner, specifically, in assembling the impulse response function. Finally, an optimization method can be employed to give the designer an optimal isolator for a given excitation and set of structural limitations.

THIS PAGE INTENTIONALLY LEFT BLANK

APPENDIX: TRAPEZOIDAL FORCE EXTRACTION VERSUS NASTRAN AND ODE45

A W36x848 50 ksi steel column was modeled using 16 nodes spaced equally over the total length of the column of 375 feet. The column was chosen from the designed 30 story building. The MATLAB code, developed for the trapezoidal force extraction's data was compared to the large mass method used in NASTRAN, [Ref. 23]. NASTRAN generated the modal data as well. The excitation was conducted in the weak axis of bending of the column. A 9-DOF system was used to validate the extraction process against MATLAB's *ode45* function.

The validation is conducted with a sinusoidal input with an amplitude of 1 centimeter converted to inches with a frequency of .5 Hz. In NASTRAN, the time step was conducted at .1 seconds for a duration of 20 seconds. Figure. 66, depicts the transient time history of the tip of the beam. Conducting the Trapezoidal force extraction program at a time step of .01 seconds and a duration of 20 seconds and a large mass representing the ground, yields a solution that is very similar to the one generated by NASTRAN. A better representation of the two plots would be to present the relative difference, as shown in Figure 67. Because the time response crosses the time axis, calculating the relative errors vice differences would generate gross errors. As the plot indicates the comparisons are acceptable.

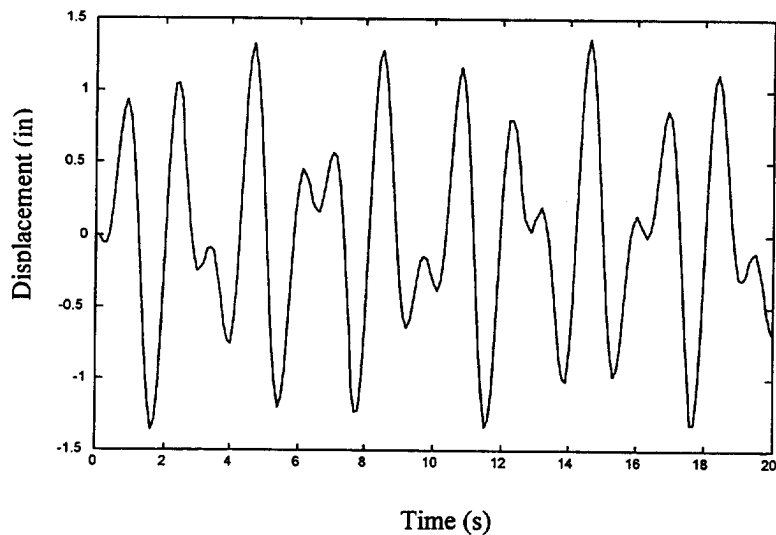


Figure 66. NASTRAN Sinusoidal Base Excitation Tip Displacement Results of a 375 Feet Steel W36x487 Column

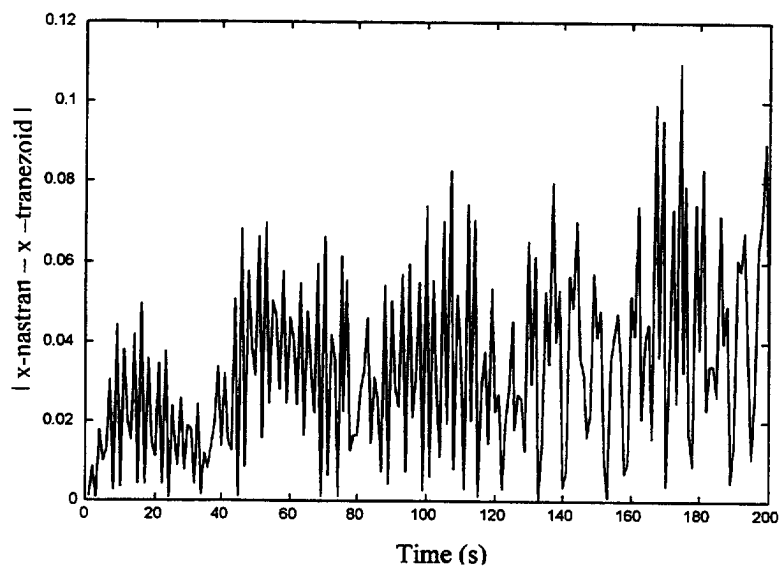


Figure 67. 375 Feet Steel W36x487 Column, NASTRAN Versus Trapezoidal Time History Difference Plot of Tip DOF

Using a 9-DOF spring mass system as presented in Figure 16, MATLAB's *ode45* function was used in accordance with the following state space representation of the governing second ordinary differential equation:

$$\begin{aligned}\begin{Bmatrix} \dot{x} \\ \dot{s} \end{Bmatrix} &= \begin{Bmatrix} s \\ \end{Bmatrix} \\ \begin{Bmatrix} \dot{s} \end{Bmatrix} &= -[M]^{-1}[C]\begin{Bmatrix} \dot{x} \\ \end{Bmatrix} - [M]^{-1}[K]\begin{Bmatrix} x \\ s \end{Bmatrix} + [M]^{-1}\{F_1^{iso}\}\end{aligned}\tag{62}$$

Where:

$$F_1^{iso} = -(10 \frac{lbf}{in})[x(1) - X_{ofT}]\tag{63}$$

Using Figure 17, the trapezoidal extraction method was used using a large mass to represent the ground and conducted at time step of .01 for 10 seconds. Figure 68, illustrates the time history response of the first mass. Again, the *ode45* plot is very similar and a difference plot was graphed in Figure 69. From the figures the extraction method is an acceptable method in developing a transient response.

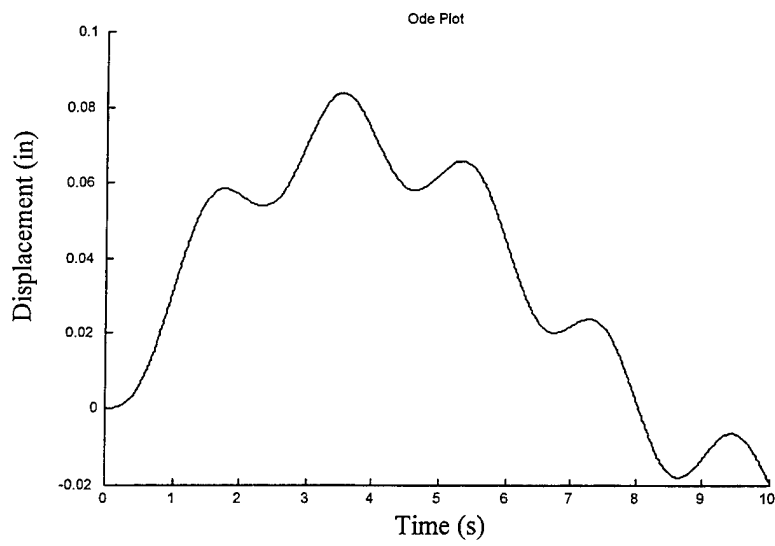


Figure 68. Trapezoidal Extraction Base Node Displacement Time History of a 9-DOF System

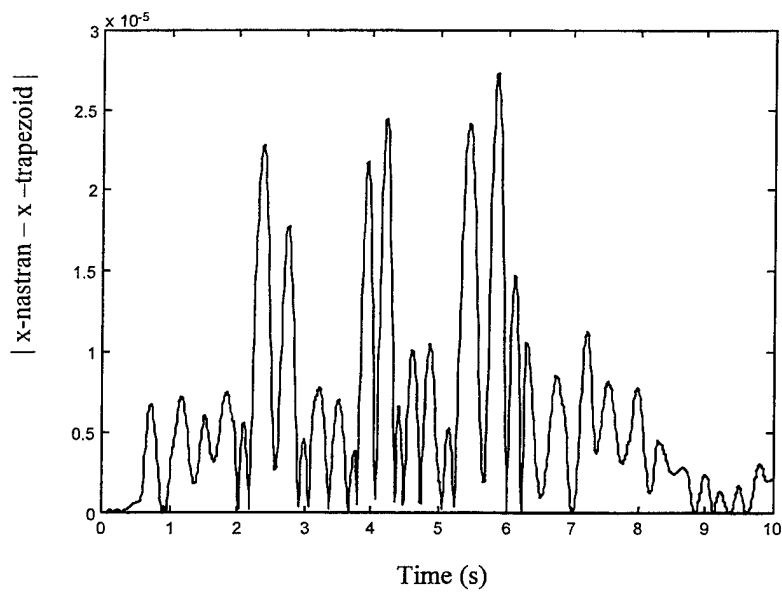


Figure 69. 9-DOF Spring Mass System, ODE Versus Trapezoidal Extraction Absolute Difference Plot of Base DOF

LIST OF REFERENCES

1. American Institute of Steel Construction Inc, *Manual of Steel Construction Load & Resistance Factor Design*, Third Printing, , AISC, 1993
2. *Uniform Building Code*, International Conference of Building Officials, Whittier, California, 1994
3. Nagarajaiah, S., Reinhorn, A., and Constantinou M. "Nonlinear Dynamic Analysis of Base Isolated Structures-Current Techniques", T125-3, 1998
4. Gordis, J.H., Radwick, J. "Efficient Transient Analysis For Large Locally Nonlinear Structures", *Shock and Vibration*, vol 6, 20 January 1999, pp1-9
5. Gordis J.H., "Integral Equation Formulation for Transient Structural Synthesis", *AIAA Journal*, vol 33, no.2, February 1995, pp. 320-324
6. Thomson, W. T., *Theory of Vibration With Applications*, 3rd Ed, Prentice Hall, 1988
7. Salmon, C, Johnson, J., *Steel Structures Design and Behavior*, 3rd Ed, Harper Collins Publishers Inc., 1990
8. "Strong Motion Data Base." [<http://smdb.crustal.uscb.edu>] March 2001.
9. Bendat, J., Piersol, A., *Engineering Applications of Correlation and Spectral Analysis*, 2nd ed, John Wiley & Sons Inc, 1993, pp. 47-77
10. Kelly, J. M., "Base Isolation: Origins and Development", National Information Service for Earthquake Engineering, UC Berkley, Nov. 4, 1999
11. Kelly, J. M., *Earthquake-Resistant Design With Rubber*, 2nd Ed, Springer-Verlag London Limited, 1997
12. Braga, F., "High Damping Elastomeric Bearings (HDEB): Experimental Tests and Preliminary Results", Dip.to di Struttre, Geotecnica, Geologia applicata All'Ingegneria (DiSGG), Italy
13. Wen, Y. K., "Method For Random Vibration of Hysteretic Systems", *Journal of the Engineering Mechanics Division*, EM2, April 1976, pp. 249-262
14. De Luca, A., Faella, G., "Modeling of Elastomeric Devices in the Dynamic Linear and Nonlinear Range", Dip.to di Struttre, Geotecnica, Geologia applicata All'Ingegneria (DiSGG), Italy

15. Inaudi, J. A., De La Llera J. C., "Dynamic Analysis of Nonlinear Structures Using State-Space Formulation and Partitioned Integration Schemes", College of Engineering University of California At Berkley, November 1992
16. Challhoub, M., Kelly, J., "Reduction of the Stiffness of Rubber Bearings Due to Compressibility", Report No. UCB/SESM-86/06, College of Engineering University of California at Berkley, 1986
17. Koh, C., Kelly, J., "Effects of Axial Load on Elastomeric Isolation Bearings", Report No. UCB/EERC-86/12, EERC, University of California at Berkley, 1987
18. Kown, Y. W., *The Finite Element Method*, CRC Press, 1997
19. Craig, R., *Structural Dynamics*, John Wiley & Sons, 1981
20. Wen, Y. K., Park, Y. J., Ang, A. H-S., "Random Vibration of Hysteretic Systems Under Bi-Directional Ground Motions", *Earthquake Engineering and Structural Dynamics*, Vol. 14, pp. 543-557, 1998
21. Gerald, C., Wheatley, P., *Applied Numerical Analysis*, Addison Wesley, 1999
22. Nagarajaiah, S., Rienhorn, A., Constantiou, M., "Nonlinear Dynamic Analysis of 3-D-Base-Isolated Structures", *Journal of Structural Engineering*, Vol. 117, No.7, pp. 2034-2054, July 1991
23. Blakely, B., *MSC/NASTRAN Basic Dynamic Analysis*, Ver. 68, Chapt. 7, pp. 205-225, 1998
24. Pearce, C., "Efficient Computation of Nonlinear Transient Structural Synthesis for Seismic Isolation", Master's Thesis, Naval Postgraduate School, Monterey, California, March 1999

INITIAL DISTRIBUTION LIST

1. Defense Technical Information Center2
 8725 John J. Kingman Road, Suite 0944
 Ft. Belvoir, VA 22060-6218

2. Dudley Knox Library2
 Naval Postgraduate School
 411 Dyer Road
 Monterey, CA 93943-5101

3. Engineering & Technology Curricular Office, Code 341
 Naval Postgraduate School
 700 Dyer Road
 Monterey, CA 93943-5100

4. Chairman, Code ME1
 Department of Mechanical Engineering
 Naval Postgraduate School
 Monterey, CA 93943-5100

5. Professor Joshua H. Gordis Code ME/Go1
 Department of Mechanical Engineering
 Naval Postgraduate School
 Monterey, CA 93943-5100

6. Lieutenant Al V. Jarque1
 1038 Delaware Street
 Imperial Beach, CA 91932